HIGH POWER DENSITY VARIABLE SPEED TRACTION MOTOR

A THESIS SUBMITTED TO
THE GRADUATE SCHOOL OF NATURAL AND APPLIED SCIENCES
OF
MIDDLE EAST TECHNICAL UNIVERSITY

BY

SALAR KOUSHAN

IN PARTIAL FULFILLMENT OF THE REQUIREMENTS
FOR
THE DEGREE OF MASTER OF SCIENCE
IN
ELECTRICAL AND ELECTRONICS ENGINEERING

JANUARY 2020

Approval of the thesis:

HIGH POWER DENSITY VARIABLE SPEED TRACTION MOTOR

submitted by **SALAR KOUSHAN** in partial fulfillment of the requirements for the degree of **Master of Science in Electrical and Electronics Engineering Department, Middle East Technical University** by,

Prof. Dr. Halil Kalıpçılar
Dean, Graduate School of **Natural and Applied Sciences**

Prof. Dr. İlkay Ulusoy
Head of Department, **Electrical and Electronics Eng.**

Assist. Prof. Dr. Ozan Keysan
Supervisor, **Electrical and Electronics Eng., METU**

Prof. Dr. Hulusi Bülent Ertan
Co-Supervisor, **Electrical and Electronics Eng., Atılım Uni.**

Examining Committee Members:

Assist. Prof. Dr. Emine Bostancı
Electrical and Electronics Eng., METU

Assist. Prof. Dr. Ozan Keysan
Electrical and Electronics Eng., METU

Prof. Dr. Hulusi Bülent Ertan
Electrical and Electronics Eng., Atılım Uni.

Assist. Prof. Dr. Özgür Bayer
Mechanical Eng., METU

Prof. Dr. Mehmet Timur Aydemir
Electrical and Electronics Eng., Gazi University

Date: 19.01.2020

I hereby declare that all information in this document has been obtained and presented in accordance with academic rules and ethical conduct. I also declare that, as required by these rules and conduct, I have fully cited and referenced all material and results that are not original to this work.

Name, Surname: Salar Koushan

Signature:

ABSTRACT

HIGH POWER DENSITY VARIABLE SPEED TRACTION MOTOR

Koushan, Salar
Master of Science, Electrical and Electronics Engineering
Supervisor: Assist. Prof. Dr. Ozan Keysan
Co-Supervisor: Prof. Dr. Hulusi Bülent Ertan

January 2020, 157 pages

The purpose of this thesis is to develop, manufacture, and test a new traction induction motor that is capable of meeting the desired characteristics, limits and expectations set by the traction application in which it will be utilized. For achieving this goal, initially the finite element (FE) calculation techniques and model accuracy is verified by modeling a reference test motor in a FE environment and verifying the loss data and performance of the motor with measurement data. After testing and modelling the reference test motor, several guidelines and criteria are defined to further help the design process and to ensure the accuracy of the results obtained. In the next step, an initial FE design is developed based on the desired motor rating, and by following the established design criteria (motor’s magnetic loading, electrical loading, current density, and cooling capacity of the motor). Through iterative analytical modification, initial FE model, is improved and an optimum design is selected. Finally, based on the developed model, the motor is manufactured and is verified through comparing the FE data with the test results. Additionally, manufactured motor is tested to ensure that the motor is capable of providing the required performance.

Keywords: Traction Motor, Induction Machine, Core Loss Estimation, Finite Element Analysis

ÖZ

DEĞİŞKEN HIZLI YÜKSEK GÜÇ YOĞUNLUKLU CER MOTORU

Koushan, Salar
Yüksek Lisans, Elektrik ve Elektronik Mühendisliği
Tez Danışmanı: Dr. Öğr. Üyesi Ozan Keysan
Ortak Tez Danışmanı: Prof. Dr. Hulusi Bülent Ertan

Ocak 2020, 157 sayfa

Bu tezin amacı, içerisinde kullanılacağı uygulaması tarafından belirlenen karakteristikleri, sınırları ve beklentileri karşılayabilecek yeni bir cer motoru geliştirmek, üretmek ve test etmektir. Bu amaca ulaşmak için, ilk olarak sonlu eleman hesaplama tekniklerinin ve modelin doğruluğu, bir referans test motorunun sonlu eleman ortamında modellenmesi ile ve motorun kayıp verilerinin ve performansının ölçüm verileriyle karşılaştırılmasıyla doğrulanır. Referans test motorun modellenmesinin ve test edilmesinin ardından, tasarım sürecine yardımcı olmak ve elde edilen sonuçların doğruluğundan emin olabilmek için birkaç kriter tanımlanmıştır. Bir sonraki adımda, istenen motor gücüne ve belirlenen tasarım kriterlerine göre (motorun manyetik yüklemesi, elektriksel yüklemesi, akım yoğunluğu ve motorun soğutma kapasitesi) uygun olarak bir sonlu eleman tasarımı geliştirilmiştir. Geliştirdiğimiz bu yeni sonlu eleman tasarımını, analitik yöntemlereler iyileştirdik ve optimum bir model elde ettik. Son olarak, geliştirilen modele göre motoru ürettik ve sonlu eleman verileri test sonuçlarıyla karşılaştırılarak doğruladık. Ek olarak, üretilen motor, gerekli performansı sağlayabildiğinden emin olmak için test edilir.

Anahtar Kelimeler: Cer motoru, Asenkron motor, Çekirdek kayıpları hesaplama yöntemi, Sonlu elemanlar yöntemi

To my family

ACKNOWLEDGEMENTS

I would like to give my thanks to Prof. Dr. H. Bülent Ertan, for his dedicated attention towards my academic endeavor. His constant support in my dissertation work has helped me to always look to the future with enthusiasm.

I would also like to thank Assistant Prof. Dr. Ozan Keysan for his support and valuable suggestions during my studies.

I want to dedicate my sincere gratitude to my family, for always being there for me, and supporting me, in my academic studies. I would like to thank my father, Sina, for being a role model as an electric engineer, my mother Farah, for always pushing me forward, with her everlasting emotional support, and my one and only sister, Sara, for making this endeavor a happy and fun journey.

I also wish to thank my friends and colleagues at METU power lab research group, staff and faculty members at METU department of Electrical and Electronics Engineering, staff at ELSAN Electric and their team designated for testing.

This work is partially funded by Scientific and Technological Research Council of Turkey under grant number TUBİTAK 5150086.

TABLE OF CONTENTS

CHAPTERS

APPENDICES

LIST OF TABLES

TABLES

LIST OF FIGURES

FIGURES

LIST OF ABBREVIATIONS

ABBREVIATIONS	
FEA	Finite Element Analysis
PMSM	Permanent Magnet Synchronous Machine
PWM	Pulse Width Modulation
DPWM	Discrete Pulse Width Modulation
DTC	Direct Torque Control
EMU	Electric Multiple Units
HST	High Speed Train
CFD	Computational Fluid Dynamics
RTM	Reference Test Motor
IM	Induction Motor
SVM	Space Vector Modulation

CHAPTER 1

INTRODUCTION

1.1. Purpose of This Study

In this thesis it is intended to develop a reference design criterion based on an available traction motor which has been used in the same application. This is achieved by modeling the reference test motor in ANSYS Maxwell through Finite Element analysis and verifying the model by comparing the test results with the data computed through FEA. The design criteria help us to develop an accurate model, making sure that the to be manufactured motors' performance will be in par with the FE model, and also gains us in computational time.

In the next step an initial model is designed, considering a set of designing constrains developed earlier, and by modifying the FE design we intend to satisfy the target performance , and to design an efficient high power, high torque density motor; while not violating the limits set by the reference model, both on the aspect of electromagnetics and thermal and fluid flow dynamics.

As Final stage, the selected FE design will be manufactured and tested to verify the design and to ensure that the manufactured motor is capable of providing the characteristics needed by the traction application.

1.2. Electric Vehicles and Traction Applications

Electric vehicles have been on the rise for the past couple of years and they are going to gain much more popularity and attention in the coming years [1] , [2] give a brief review of the available topologies used in traction applications , amongst those Induction motors are good candidates for the electrical vehicles, and IMs have been the backbone of the industry for many years, and although many new motor types have emerged and replaced induction motor in some applications, they are being preferred mainly due to their cost efficiency over to the other types, and there is still a trend towards more efficient induction motors so that it becomes more competitive in the market. [3] gives a review of challenges and a macroscopic look towards induction machines and their usage for industrial applications.

1.3. Modelling, Simulation, and Verification

The purpose of this thesis is to design, verify and manufacture a traction induction motor. Considering this, an initial FE model should be developed; several design criteria are determined based on a reference test motor to ensure the accuracy of the FE models. To achieve an accurate FE model there are methods in the literature to investigate the loss calculations and improve the FEA for efficiency evaluation of an electrical machine. It will be of importance if the results of a FEA is verified through controlled test results.

1.4. Core Loss Estimation

One of the challenges in calculating the efficiency and truly predicting the motor performance lies within the core loss component and how to effectively calculate the value. A more popular approach would be using the Finite Element method whether in 2D or 3D environment, although FE 3D method may yield a more accurate result it will not be time friendly and on the other hand FE 2D will use approximations and will disregard the higher frequency order components. A more responsive method can be used [4] by combining the analytical approach with FEA. In the literature on the topic of induction machines researches are geared towards higher order loss component [5] and ways to improve the design [6] by investigating the reason behind this phenomena. For this reason space harmonics [7], [8], [9] are widely discussed in the literature.

1.5. Chapter Description

Chapter 1 contains a brief introduction to the thesis with main focus on the topic of induction machines, and literature review of materials related with loss determination and efficiency evaluation, and design strategies to improve the IMs efficiency.

Chapter 2 is dedicated on building a reference test motor in a FE environment by comparing the performance and characteristics of the model with the measurement data, so to verify the methods being used in modelling and loss calculation of the model.

In chapter 3 an initial design is selected and based on the limiting factors and design constraints; a final design has been achieved.

Chapter 4 includes test results on the final manufactured prototype at various conditions and it moves on to show the capabilities of the machine on satisfying the target performance as well as comparing the measurement data with the Finite Element results.

1.6. Literature Review

With electrifications of transportation, traction motors are becoming more popular than ever, and induction motor is not an exception. The traction induction motors are known for their robustness and reliability. However it lacks in efficiency compared to Permanent Magnet Synchronous Machines (PMSM), it is more important to determine the loss components and their distribution trend in more details, so that the motor design can be modified to address those loss components and to decrease the overall heat generation in the machine.

In designing a traction motor or any kind of electrical machines, one of the indispensable tools that is used is the Finite Element (FE) analysis, which is used to analyze the model, and to make sure that the manufactured motor will be performing as intended.

A Literature survey is done to brief the papers available in two main areas of a) efficiency and loss evaluation, and b) design, development, and optimization.

1.6.1. FE Model Analysis, Loss Determination and Efficiency Evaluation

In [10] paper aims to design an induction for traction applications with higher efficiency ratings close to the PM machines so that it can be considered a first priority for the railway applications. It states that the efficiency of the induction motors used in traction applications is usually around 92 %, however PMSM used in the same application has an efficiency of 97 %.

The aim of this paper is to do research on possible fronts to increase the efficiency of the induction traction motor to approximately 96 % by use of low-loss materials, optimization of the number of series turns per phase in stator windings, modifications of the rotor slot shape, and reduction of mechanical loss.

The specifications of a conventional induction for traction application (IM-C) and its optimized prototype (IM-P) variant is included in the Table 1.1. In order to reach IM-P several FEA analysis have been investigated which are included in .

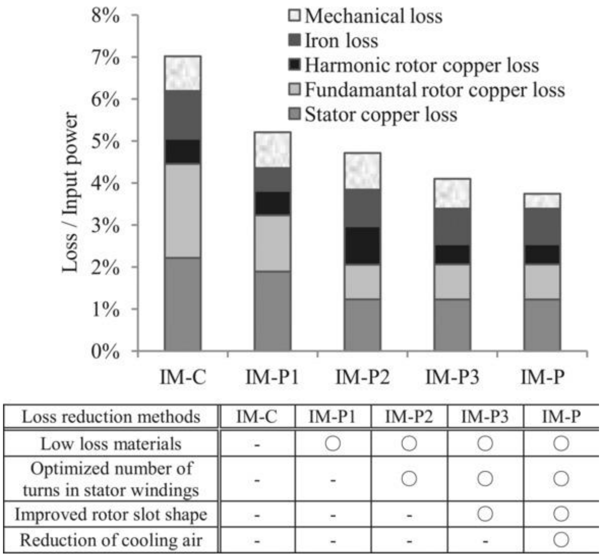

Loss reduction methods	IM-C	IM-P1	IM-P2	IM-P3	IM-P
Low loss materials	-	○	○	○	○
Optimized number of turns in stator windings	-	-	○	○	○
Improved rotor slot shape	-	-	-	○	○
Reduction of cooling air	-	-	-	-	○

Figure 1.1. FEA Results for Losses in Traction Motors

Table 1.1. *Comparison of Developed Prototype Machine (IM-P) with a Conventional Induction Motor(IM-C)*

Traction Motor	IM-C	IM-P
Motor type	Squirrel cage induction motor	
Cooling type	Open self-ventilated cooling	
Phases/ Poles	Three phases/ Four poles	
Core length	190 mm	
Core outer diameter	518 mm	
Number of stator slots	36	
Number of rotor slots	46	
Rated voltage	1100	
Rated frequency	100 Hz	
Rated output (1 h)	220 kW	
Rated output (cont.)	195 kW	
Maximum working speed	5821/min	
Core material	50A800	35A300
Rotor conductor	Red brass	Silver bearing copper
Conductivity (115 C)	4.72 μΩcm	2.37 μΩcm
Number of turns in series per phase	72	54

By comparing the plots in it is seen that the efficiency of the IM-P is approximately improved by 3% compared to the IM-C. And how this improvement is achieved is explained in four parts.

Part A. Utilizing Low loss materials used in stator winding, rotor conductors, and iron core:

In rotor conductors silver containing copper is used which has a reduced resistance compared to the red brass. Also, by selecting 35A300 as the rotor and stator core laminations, the iron loss is expected to reduce. In stator windings, by using a Kapton wire, the insulator thickness is reduced, and this allow for higher fill factor, and as the result reducing the resistance per phase of the stator winding. Based on the analytical results the efficiency of the prototype IM-P1 is improved by 1.8% simply by selecting more efficient materials.

Part B. Optimizing the stator winding’s turns per phase:

The series turns per phase is reduced from 72 to 54 comparing, IM-P with IM-C. The idea behind this change is to balance the iron core loss and the copper loss happening in the stator and the rotor. The author states that the torque produced is approximately proportional to the product of the current density and the magnetic flux density, so in order to minimize the sum of iron loss and the copper loss while keeping torque constant the two loss type values should be the same.

By examining the IM-P1 and IM-C at rated point, the copper loss is greater than the core loss. So, by reducing the turns per phase number in IM-P2. Although the flux density increases and thus the core loss, the decrease in the copper loss will overcome the heat generated in the iron parts, and as the final result the efficiency of the IM-P2 to improve by 0.5 % compared to the IM-P1.

Part C. Rotor slot shape modification:

It is known that in induction motors a portion of the copper loss known as harmonic secondary copper loss exists due to the harmonic components present in the flux density distribution because of the slotting of the rotor and the stator. Due to nature of the harmonic secondary copper loss, it is found that they consist a majority of the copper loss, and due to the skin effect phenomena, they exist at layers of the rotor bar close to the surface. So, four different cases are investigated for this purpose.

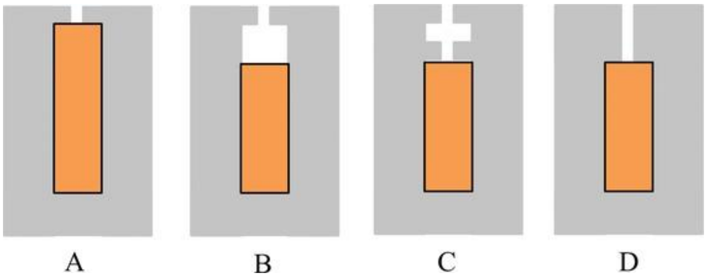

Figure 1.2. Candidate Rotor Slots

An initial slot shape is selected as in Figure 1.2 (A). Although Figure 1.2 (B) was able to reduce the aforementioned loss, it was not suggested due to the centrifugal forces. The Figure 1.2 (D) was not preferred due to the deep bar effect and increased leakage inductance affecting the torque. Finally, the rotor slot shape of Figure 1.2 (C) is selected which reduces the harmonic secondary copper loss. And the overall efficiency of the Im-P3 is 0.4 % improved compared to the IM-P2.

Part D. Improve self-ventilated cooling system of the IM-P, and reduced mechanical loss:

The cooling is improved by the increased space in the air gap due to change of shape on the rotor slot shape. And by only this change the mechanical loss is slightly improved compared to the IM-C in IM-P3. In total by changing the shape of the rotor slot, the cooling is more efficient, and so the cooling air flow rate can be decreased which means decreased mechanical loss.

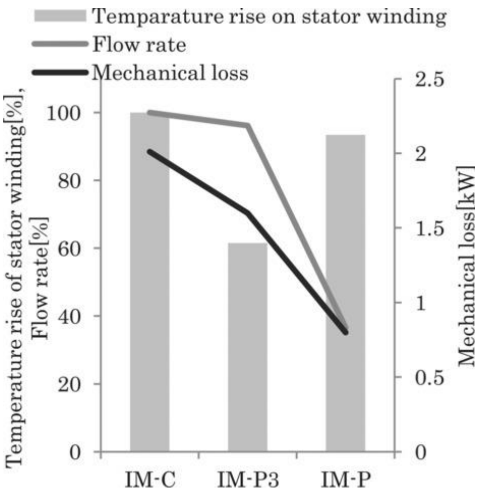

Figure 1.3. Reduction of Mechanical Loss

Indirect efficiency evaluation is suggested because of its improved accuracy over direct method. In this method, stator copper loss, rotor copper loss, iron loss, stray load loss, and mechanical loss is individually calculated and summed.

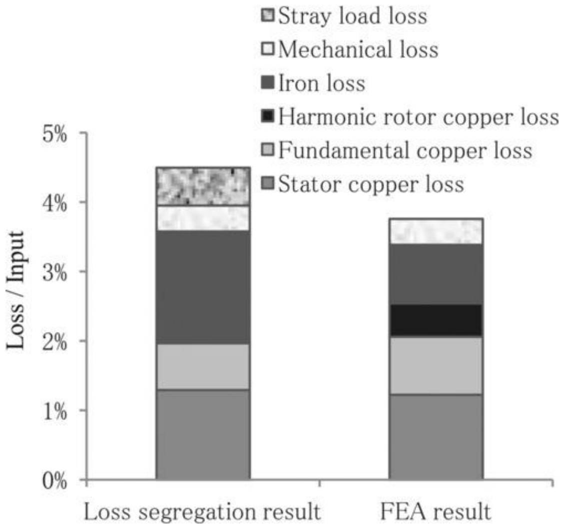

Figure 1.4. Determination of Losses

As the Figure 1.4 suggests the objective of reaching an efficiency value of 95 to 96% is achieved compared to the 97 % efficiency of the PMSM.

In the case of calculating the stray load loss, the paper lacks to bring a viable solution in FEA for calculating the stray load loss, and how it can separate the copper loss and iron loss in the rotor bars, stator windings or the iron core into fundamental components and the higher frequency component devised as stray load loss. Further analysis and measurements can be done to separate the stray load loss components included in the stator copper loss and iron losses.

In [11] energy efficiency of a 5-kW induction motor is analyzed. For the evaluation, FEA and measurement data is investigated. The rated values of the motor are included in Table 1.2:

Table 1.2. *Rated Values of the 5-kW IM*

Motor Parameter	*Value*
Stator stack length	160 mm
Stator core outer diameter	220 mm
Stator core inner diameter	125 mm
Air gap	0.5 mm
Number of winding turns in one phase	257
Winding configuration	Y
Rated Voltage	400
Rated frequency	50 Hz
Rated power	5 Kw
Rated speed	1467 min^{-1}
Rated current	10.4 A

The motor in this paper represent a typical modern industrial motor with IE3 efficiency rating. However a special focus is given to the eddy current loss by selecting a worse material for the loss, to be recognizable. The paper uses a 2D FEM to analyze the motor at 4 different frequencies. To properly model the motor , it determines the end region parameters analytically and uses external circuit to include parameters in the analysis. Stator phase resistance, end winding leakage inductance, end ring resistance [12] ,end ring leakage inductance, squirrel-cage leakage resistance, and squirrel-cage leakage inductance are determined and added as external elements.

After the FE model is finalized, model’s behavior is studied, by varying parameters like stator end leakage inductance, slip; investigating the torque behavior as a function of time by changing end winding inductance; Analyzing iron loss as a function of frequency. Figure 1.5 shows the effect of stator end winding inductance on the transient torque waveform .

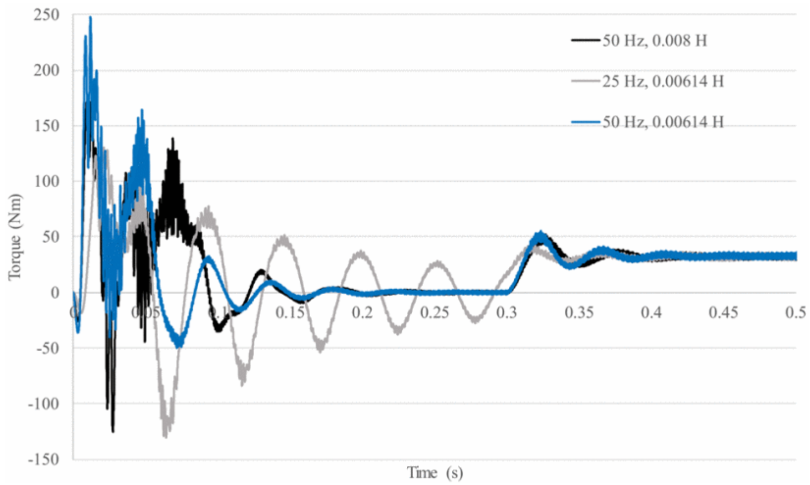

Figure 1.5. Motor Torque as a Function of Time with Different End Winding Values

The paper tries to tune the externally included parameters to study their effects in the FEA model and to measure how sensitive these parameters are and how they will change the performance result.

Motor is tested at four different frequencies, and voltage levels. The U/f is kept constant to keep the magnetization in the machine constant. In this study IEC loss segregation method is used.

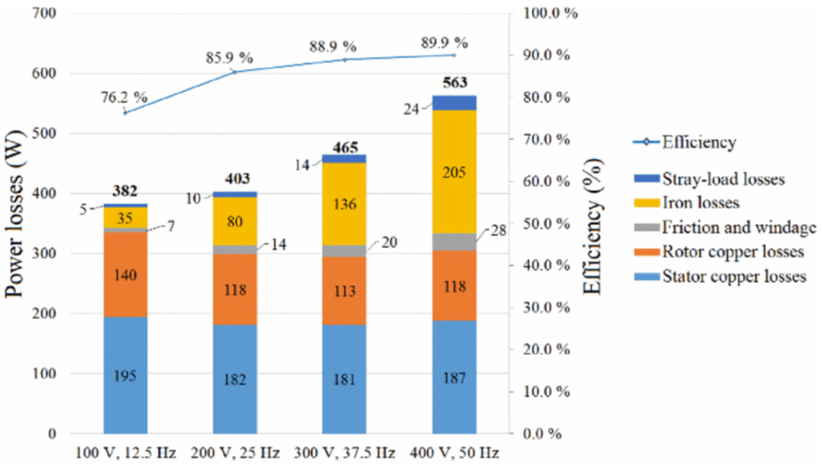

Figure 1.6. Measurement Result for the Loss Components, Total Losses, and Efficiency of the 5 kW Induction Motor at Four Different Supply Frequencies

As paper suggests in order to model the losses accurately, and verify the results, it is possible to compare the current wave forms, from which it gives us an indication of which if the motor is characterized good enough in the FE environment, and by studying the FFT of the current waveforms we can see the accuracy level of the FE and what can be done to improve the simulation model.

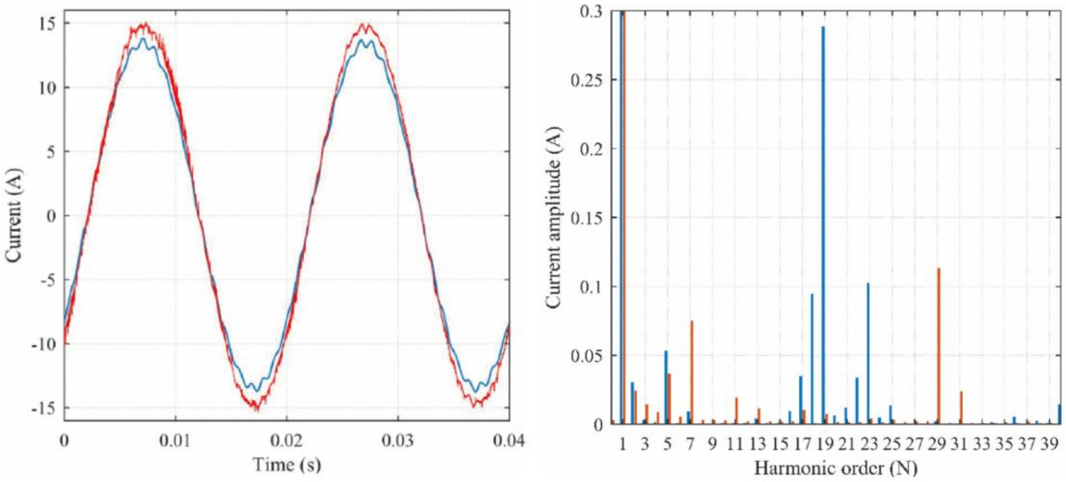

Figure 1.7. Comparison of the Measured and FEA Computed Currents at 50 Hz(Left Image), and Their FFT Analysis(Right Image)

By analyzing the current waveform in Figure 1.7 and its FFT analysis it can be deduced that :

- Some harmonics are present in the measurement data due to the voltage harmonics from the supply that are absent in the simulation waveform.
- In the FE model the skewing is not taken into considerations, so the harmonics originated from the rotor slot harmonics are higher in the simulation model. (Harmonics from 17 to 21)

And finally to benchmark the FE computed loss components measurement data is provided. The FE computed loss values is included in Figure 1.8 by comparing the FE losses with the measurement it is obvious the relative value of the losses are in agreement.

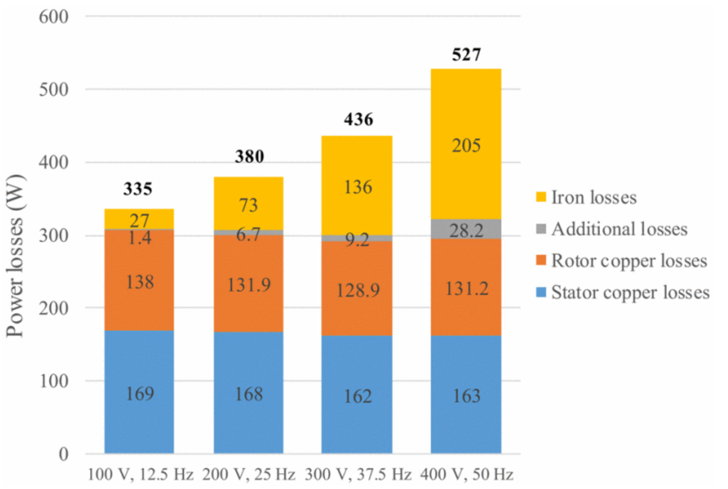

Figure 1.8. Computed Results for the Loss Components, Total Losses of the 5-kw Induction Motor at Four Different Supply Frequencies

In order to improve the accuracy of the model it is possible to utilize the 3D FE, if the mesh element are limited, and it is feasible to do a simulation considering time limit, And it can be of importance to simulate the model with the exact voltage of the measurement data to include the harmonics.

In [13] paper is investigating the loss calculation and efficiency determination with more focus towards the driver and different modulation techniques. The motive behind this study is the absence of a regulated loss calculation and efficiency determination for the convert-fed induction machines. The paper analyzes a single motor by performing measurements and FE simulations with three different modulation techniques and determining the loss components as well as comparing the measurement data with the simulation model.

In this paper loss segregation procedure IEC 60034-2-1 and IEC 60034-2-3 are used. A detailed FE is constructed, and the validity of the test results are checked by comparing both methods. For the numerical method to be in par with the actual motor, voltage waveforms are recorded from the motor terminals and used to supply the model. The motor's parameters are included in Table 1.3.

Table 1.3. *TEFC Motor Parameters for Delta Connection*

Variable	*Value*
Power	37-kW
Current	65.4 A
Voltage	400 V
Torque	239 Nm
Frequency	50 Hz
Speed	1482 min^{-1}
Efficiency	94.9 % (IE3)

In standard loss segregation there are five parts: stator copper loss, rotor copper loss, iron losses, mechanical losses, and additional load losses or stray loss. The methods used for the loss calculations are well known as mentioned in the standard however there are some challenges as mentioned in [14] when segregating the loss components. There are a few methods for estimating the additional load loss through indirect methods, and there are few experimental methods. In IEC standard the additional load losses are determined through residual loss(“P_{LR}”) at each load point of the load curve test, and by using linear regression the loss value is estimated at various load levels.

$$P_{Lr} = P_1 - P_2 - P_s - P_r - P_{Fe} - P_{fw} \tag{1-1}$$

The loss components in Equation (1-1) with order from left are: residual loss, input power, output power, stator copper loss, rotor copper loss, iron loss, and mechanical loss.

As mentioned earlier, the purpose of this study is to evaluate the efficiency considering various modulation techniques and their effect compared with a sinusoidal source. Here three different commercially available converter with different modulation technique are used, and by recording the voltage waveform the simulation is replicated through feeding the model the same signals. The three methods are : direct torque control (DTC), space vector modulation (SVM), and symmetrical two-phase modulation (DPWM).

Several points can be extracted from the paper with respect to using various modulation techniques :

- In calculating the overall measure loss, the DTC method has the higher fundamental voltage which leads to lower losses.
- DTC has the fast torque response, simple design and robustness against parameter variation, however variable switching frequency and high torque ripple might be considered a drawback in some cases.
- The difference between a PWM and DTC method lies in the switching pattern where in PWN switched are controlled by a predefined pattern, the switched are controlled by the output of torque and flux linkage errors.
- By using DPWM in theory provides 33 % reduction in the effective switching frequency and switching losses compared with the standard SVPWM.

In comparing the results obtained from the numerical simulations and the measurement data it becomes noted that :

- The total losses are in agreement and in all three modulation techniques the total loss value is accurately predicted.
- Bothe the DTC, and SVPWM the results are matching, however in DPWM the results are less coherent.

In this study all individual loss components are segregated, using numerical methods and IEC loss segregation technique, there are several points that are worth mentioning:

- The measured stator copper losses are estimated based on the dc resistance corrected to the operating temperature, and ac resistance is ignored.
- It is assumed that the magnitude of the fundamental magnetic flux from sinusoidal source and the PWM source is the same. As the result the simulated iron losses in FE is much higher than the analytically calculated iron loss based on measurement. Since in FE the iron loss included the loss component created by harmonics.
- Additional load losses only are added to the measured loss values, whereas in FE it is already included in the calculated components.

The paper uses recorded voltage waveform from the motor terminal for the FE simulations, however this approach is a time-consuming approach if a small time step is selected so that the model can follow the voltage waveform. It can be beneficial if the system used current excitation.

In calculating the core loss in FE a post processing operation is used, and effect of the core loss on B field in an iterative manner is not analyzed, it will further increase the core loss if it were to calculate the core loss in an online manner.

In [15] it explains various motor types used, and their cooling technology which is selected by the application type and the environment in which the motor is going to be used.

In railway market there is demand towards high performance low cost, and compact motors with high torque and power density. The motor types that can be used in this application are usually limited to Induction motors, PM motors. The electromagnetic design that is going to be selected is dependent on the five main application type: Locomotives, Electric Multiple Units (EMUs), metro, LRV, or High-Speed Trains (HST). Each application has certain requirements and demand a certain type of electromagnetic design, motor size and cooling system. A typical comparison between these five applications types is included in the paper which is shown in Figure 1.9

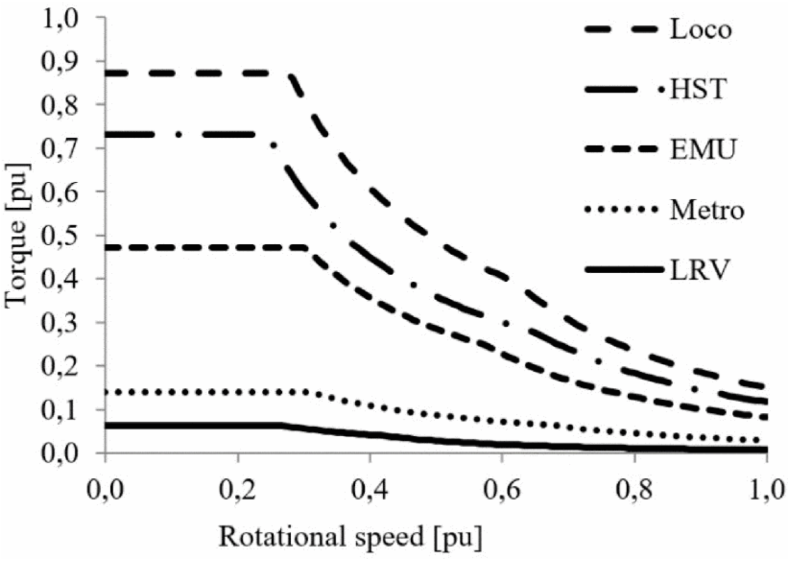

Figure 1.9. A Typical Comparison Between the Traction Motor Performances Required in Different Railway Applications

Induction motors:

- Are Considered due to simple design, low cost, and their robustness.
- Aluminum and copper squirrel cage rotors have been the dominant topologies.
- In some applications in which a group of motor is driven by a single inverter aluminum bars are preferred as expressed in Figure 1.10.
- The trend is toward further reduction of cost, and increase of compactness, topologies with copper rotor bars can be beneficial with this regard.

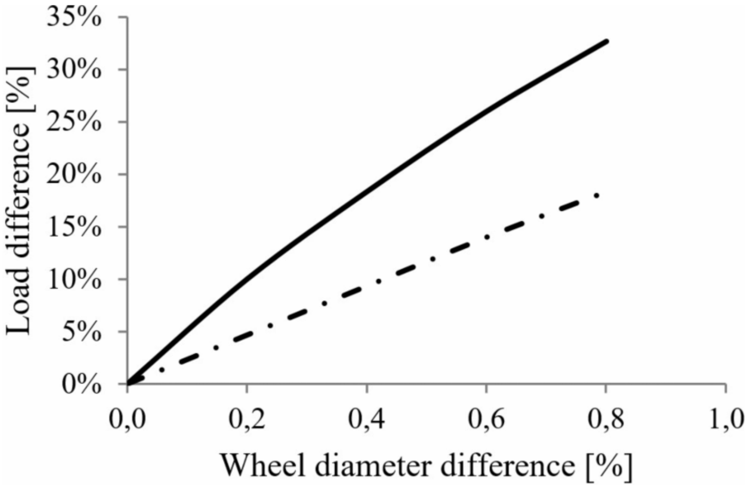

Figure 1.10. The Load Sharing Between Two Parallel Connected Motors Using either an Aluminum Rotor (Dashed Line) or a Copper Rotor (Solid Line)

Permanent Magnet Motors:

- Generally have higher torque density and efficiency compared to induction motors.
- One of the main disadvantages of its usage is its dependency on rare earth magnets and as a result higher cost and uncertainty of the market.
- In high speed trains due to its much-needed higher performance PMs are preferred.

- In PM motor there is a trend towards reducing the usage of rare earth materials by moving towards permanent magnet assisted synchronous reluctance motors.

There are different types of cooling systems and selecting a cooling system and its capacity is linked to the loss distribution and the duty cycle of the machine, also it relies on the environment and level of dirt in the application used. In paper four main cooling types are suggested : open air forced-ventilated cooling, open air self-ventilated cooling, enclosed air self-ventilated cooling.

In open air forced-ventilated cooling:

- The cooling is provided via duct supplied from an external fan.
- This enables higher torque levels, and power levels due to cooling being independent of motor speed.
- Better air quality due to the placement of the external fan in a cleaner area, which ensures the low risk of blockage of cooling ducts.
- Cost and extra space is the main challenge.

In open air self-ventilated cooling:

- The advantages are the relatively simple design, cost efficiency , and no need for extra space, despites its drawback of decreased performance at low speeds(<) and higher noise at high speeds(>4000 rpm).
- The limiting factor is the maximum speed due to acceptable noise levels.

Enclosed air self-ventilated cooling is preferred in dirty environments where low floor is preferred, and cooling air is supplied from underneath the bogie.

Another means of better cooling the motor is the selection of materials which are highly thermal conductive to enhance the heat transfer.

This study briefly discusses motor topologies and their cooling system used in traction applications, investigates their advantages and disadvantages based on application type.

In [16] the paper aims to investigate the core materials and their effect on the motor performance. Selecting a core material as paper suggests depends on the operating point. For a non-oriented electrical steel material generally as magnetic flux density saturation point decreases, specific core loss decreases too; And if a material has high magnetic flux density saturation point it will have a higher specific core loss. It is important to study the materials, while integrated into the system and consider the overall effectiveness of the material at various operating points.

Three materials are considered in this study 35PN230, 50PN470, and 50PN1300. The summary of their characteristics is included in Table 1.4.

Table 1.4. *Summary of Core Materials*

Characteristics	*35PN230*	*50PN470*	*50PN1300*
Thickness [mm]	0.35	0.5	0.5
Specific core loss [W/kg at 1.5 T 50 Hz]	2.12	3.04	5.7

The B-H curves are included in Figure 1.11.

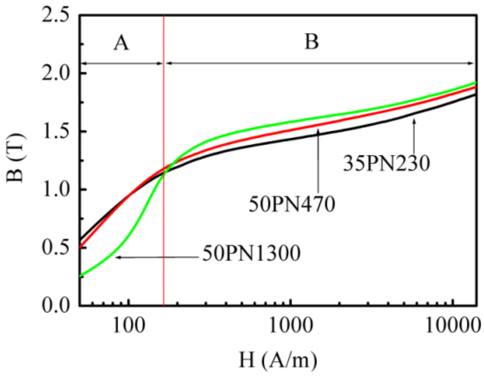

Figure 1.11. B-H Curves of Core Materials

Point of interest here is the operating regions, where for example 35PN230 if operated in region A will have lower flux density compared to others and as such will have smaller current, core loss, and as the result higher efficiency. So it will have higher efficiency in region A, however if it is to be used in region B. Although it may have lower specific core loss compared to the other two materials, but because of the lower saturation flux of the material in region B it may have more copper loss, so the efficiency cannot be compared.

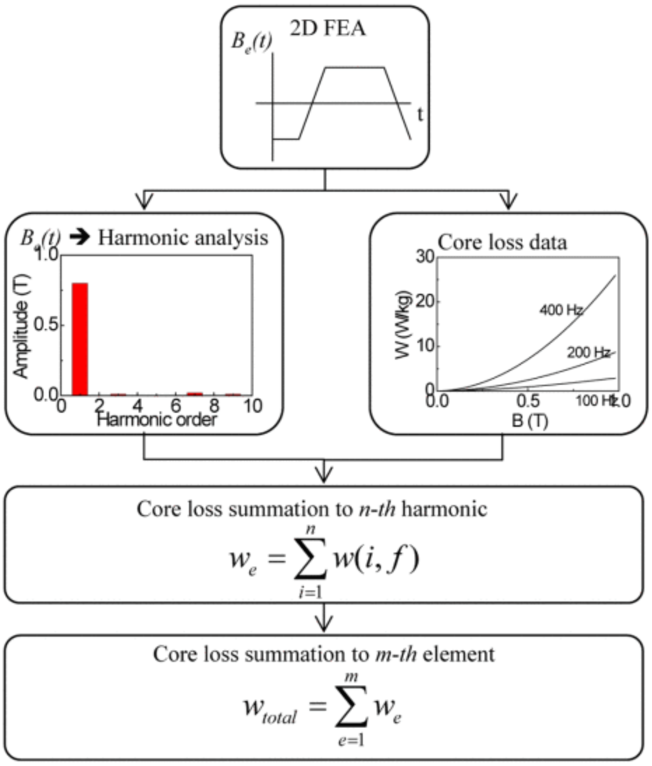

Figure 1.12. Core Loss Calculation Process

Under sinusoidal flux distribution, core loss is computed in the frequency domain as the following :

$$P_{core} = P_h + P_c + P_e = K_h f (B_m)^2 + K_c (f B_m)^2 + K_c (f B_m)^{1.5} \qquad (1\text{-}2)$$

In which, “B_m” is the amplitude of the ac flux component, “f” is the frequency, and “K_h , K_c , K_e” are respectively hysteresis, eddy-current, and excess core loss coefficients.

Here in this paper 2D transient FEA is used and by using the FFT analysis and employing Equation (1-2) core loss is calculated. By using various operating points at different load (Torque) levels and using the FEA as well as the experimental measurement. Several points are deduced from the results :

- Although a material may have lower core loss in an operating point, the system might not have higher efficiency.
- A system with a material although may have higher efficiencies at certain operating ranges, it might have a noticeable lower efficiency at another operating region.

So in conclusion it can be said that a high grade of core material with higher cost does not always guarantee an improved efficiency, and a proper material should be selected with the requirement needed of a certain application.

The purpose of [4] is to estimate the high-frequency loss components of core loss in a much efficient manner which will use much less computational time if only 2D and 3D FE simulation is used.

This high-Frequency loss is based on the eddy current loss, with an assumption of a defined path for eddy current within each lamination shown in Figure 1.13. In this study it is assumed that the supplied power is a purely sinusoidal source . With this assumption the harmonics present in the air gap are mainly due to the slotting, geometric properties of the lamination, and distribution of the conductors in the stator and the rotor slots. The flux density distribution in the air gap can be easily obtained , proving the existing of these harmonics. A flux density distribution in the air gap is shown in Figure 1.14. Each point on the rotor sees this waveform passing by, since it is a varying B waveform it will induce eddy currents on the rotor; the frequency of the induced component is related to the relative speed of the rotor and the traveling waveform. And the penetration depth of the induced current into the rotor is dependent on the frequency of the induced component. Obviously, the traveling waveform of B shown in Figure 1.14 consists of multiple traveling waveforms at different frequencies with respect to rotor. The components of this waveform can be easily obtained by taking the FFT of it. By summing up the core loss component of each harmonic content we can estimate the total high frequency core loss.

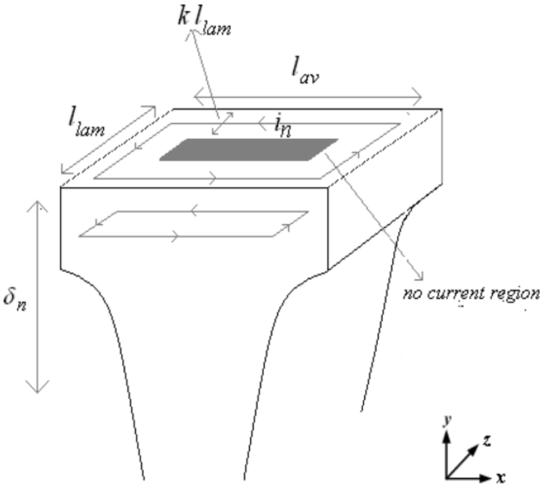

Figure 1.13. Eddy Current Path Within a Lamination of Thickness l_{lam}

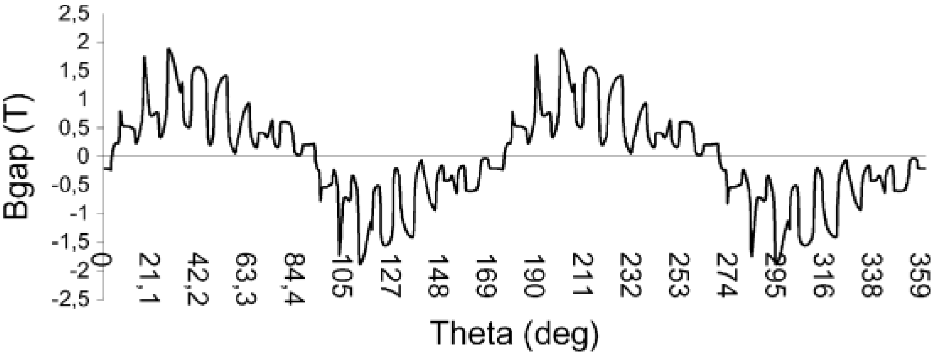

Figure 1.14. Variation of the Magnetic Flux Density in the Air Gap of the C100-Frame Motor

High-Frequency core loss calculation method:

$$P_{n,t,lam} = P_{1,t} \times \frac{{l_{lam}}^2 \times k}{2 \times {l_{lav}}^2} \times \left(\frac{B_n f_n}{B_1 f_1}\right)^2 \qquad (1\text{-}3)$$

This equation is valid for each rotor tooth at each lamination. Therefore to find the total high-frequency loss for the entire rotor core of the nth harmonic we have to multiply Equation (1-3) by the total number of laminations and by the number of rotor teeth. Which is shown in Equation (1-4) :

$$P_n = t \times P_{1,t} \times \frac{{l_{lam}}^2 \times k}{2 \times {l_{lav}}^2} \times \left(\frac{B_n f_n}{B_1 f_1}\right)^2 \quad (1\text{-}4)$$

P_n is The power loss due to the nth harmonic in the entire core, t is the product of the number of laminations and the number of rotor teeth, $P_{1,t}$ is the Power loss calculated by the FE analysis in one tooth of one lamination in the penetration depth of the nth harmonic, l_{lav} is the average current path width (one rotor tooth pitch), l_{lam} is Thickness of a lamination, k is a constant, B_n is the flux density magnitude of the nth harmonic, f_n is frequency of the nth harmonic observed by the rotor [8] B_1 is fundamental frequency flux density, and f_1 is the frequency of the fundamental waveform in the airgap.

The proposed method is verified using a typical induction motor. Bu using this method it is possible to benchmark the results obtained from the ANSYS Maxwell 2D analysis. However the challenge is to be able to calculate the fundamental core loss without the presence of the high frequency components. A further study can be implemented to estimate the core loss of the motor when it is driven from a non-sinusoidal voltage source.

In [17] This paper suggests a method for estimating no-load core loss as well as high frequency core loss components, by utilizing the FEA in combination with analytical methods. The core loss calculation used in FEA is a post processing method which further reduces the time needed for the FEA. A Discrete Fourier Transform (DFT) is uses in combination with the data obtained from the FEA which will be used in the analytical calculations.

The core loss calculation method used in this paper is based on the Bertotti’s method [18] as in Equation (1-2). A crucial technique used in this study is selecting several points on critical elements of the FE solution nodes to be able to study the magnetic flux density harmonic distribution throughout the motor surface. By using DFT it is possible to determine the contribution of higher harmonics at each element.

$$\underline{B}_k = \sum_{n=0}^{N-1} B\,(n) e^{\frac{-i2\pi kn}{N}}, k = 0, 1, \dots, \frac{N}{2} \qquad (1\text{-}5)$$

Where k is the harmonic order and N is the number of sample points. This allows the core loss to be calculated individually for each harmonic and by summing up it is possible to calculate the total core loss. Additionally we can produce the distribution map of the harmonics of the magnetic flux, where in a commercial software like ANSYS MAXWELL it gives the overall superimposed B distribution on the surfaces.

Another outcome of the paper is the slot harmonics and as the paper suggests space harmonics and specifically slot harmonics largely contribute to the total core loss, and it is possible to calculate these components using Equation (1-6).

$$P_{s0v} = p_{scv} \frac{\rho_{Fe} \pi D_{si(re)}^2 l_{s(r)} k_{Fe} k_{cs(r)}}{4|v_{r(s)}|} (\frac{B_{r(s)v}}{1.5})^2 (\frac{f_{s(r)v}}{50})^2 \qquad (1\text{-}6)$$

Where ρ_{Fe} is the mass density of the core material, P_{s0v} is the additional surface loss, D_{si} is the stator inner diameter, D_{re} is the rotor external diameter, $l_{s(r)}$ is the length of the stator or rotor, p_{scv} is the eddy-current loss density in the sheets for a flux density of 1.5 T and a frequency of 50 Hz, $v_{r(s)}$ is the harmonic order with respect to stator or rotor, B and f are the amplitude of the magnetic flux density with respect to a harmonic and its frequency .

Although this paper uses measurement to accurately determine the specific core loss and the magnetic characteristics of the material used in the simulations, it is possible to easily implement it in an study if details of the electrical used in a FE simulation model is known.

1.6.2. Design, Development, and Optimization Methods

In [19] authors address two issues with traction motors which are intertwined and should be solved in combination. It is the cooling and acoustics in an enclosed induction traction motor. The cooling system in this study is radial inner fan mounted on the shaft of the motor. The motor's performance that is being analyzed is included in Table 1.5.

Table 1.5. *Specification of Motor*

Type	*Value*
Pole- Output	6- 160 kW
Voltage- Frequency	1100 V- 70 Hz
Rated current	112 A
Rated rotation	2080 rpm
Insulation class	H class
Operating cycle	S1

Traction motors are different from conventional motors regarding the cooling, and it is the limited space for the motor, dirty environment, and capability to endure higher temperature rise. The purpose of the study is to develop a fan in order to reduce the acoustic noise and to utilize the newly developed fan geometry with optimized cooling system for enclosed motor types.

To reduce the acoustic noise developed by the fan, an uneven pitch radial fan is developed. The main reason for the acoustic noise created by the even pitched fan blades is the rotational blade noise. With even blades sound pressure from a stationary point of view shows a pure sinusoidal waveform which is transformed to sound pressure focused on a single frequency. The frequency of the rotational blade noise is calculated in Equation (1-7). In which f_z is the noise frequency, f_n is the rotational frequency, and Z is the number of blades.

$$f_z = f_n \times Z \tag{1-7}$$

The paper suggests using uneven pitched blades so to disperse the peak sound to a range of frequencies with lowered maximum amplitude.

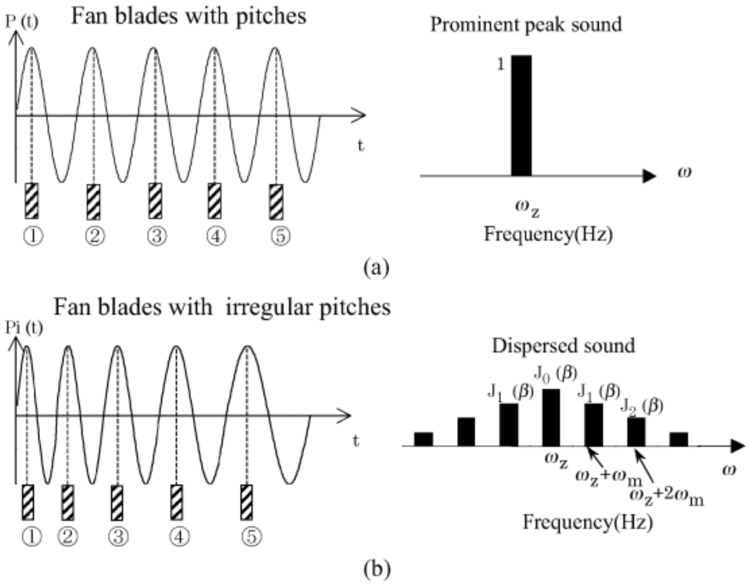

Figure 1.15. Sound Pressure and Frequency of Blade Pitch. (a) Spectrum of Even Pitch Fans. (b) Spectrum of Irregular Pitch Fans

However there is a problem with the uneven distribution of the blades which is the unbalanced rotational load. It is possible to balance the load by arranging adjacent blades to have predetermined tilt but in different directions.

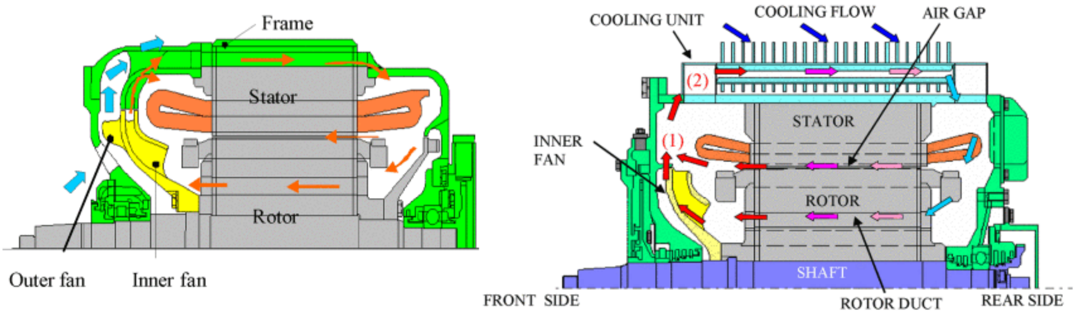

Figure 1.16. (a) Totally Enclosed Motor with External Fan on the Right, and (b) Totally Enclosed Motor without External Fan on the Left

As mentioned earlier the newly developed fan is incorporated in an enclosed motor. Two different enclosed motor types are investigated here. A) totally enclosed motor with external cooling fan shown in Figure 1.16 (a), and B) totally enclosed motor without external fan shown in Figure 1.16(b). Both topologies use the inner fan with uneven pitched blades. The conventional enclosed system (A) is used for comparison purposes. Point of interest is the second topology (B) , in which:

- In order to improve the acoustics and cooling, external fan is removed.
- An inner fan is used , and radiating fin directly coupled to the stator , in a frameless design to better dissipate the generated heat.
- Rotor ducts are utilized

As included in Table 1.6 the paper suggests removing the external fan and using a totally enclosed topology can improve the cooling, additionally it helps to reduce the acoustic noise from 77 decibel to 70 decibel (while in no-load operation at 3000 rpm). However the paper just mentions acoustic noise for a limited speed range, whereas at higher speed the acoustic noise becomes more challenging, and it is better to use external fan system. And considering the cooling, the traction application requires frequent acceleration which will attenuate the effectiveness of a radial fan mounted on the motor shaft at low speeds.

Table 1.6. *Temperature Rise of Each Motor*

Type	*Temperature rise(°C)*		
	External uneven pitch fan	*Without external fan (enclosed)*	*Limit*
Stator	131	111	190
Rotor	156	120	210

1.6.3. Comments

The studies included in Sections 1.6.1 and 1.6.2 have a similar approach to IMs and how it is possible to further improve this type of topology. In most of the papers the authors try to investigate the source of the loss component with higher accuracy so that a design procedure can be developed. And a main concern of some of the papers is the fact that there is not a uniform testing procedure for determining the efficiency specifically when it comes to inverter driven induction motors. This is a problem that will be faced within this study as well. It goes the same as for the measurement techniques used based on different IEC or IEEE standards.

In this thesis a crucial part of the thesis depends on being able to determine the FE loss components accurately as well as finding a measurement technique that is applicable and will yield a better accuracy. So these resources will further help to build a more accurate model and to investigate the loss components with increased accuracy.

CHAPTER 2

ASSESSMENT OF FINITE ELEMENT METHOD FOR PERFORMANCE EVALUATION

2.1. Introduction

The aim of this chapter is to develop an accurate model utilizing a FE analysis software that can predict the performance of an induction motor at a given operating condition. Such a model must be capable of making sure that thermal limits of the motor is not exceeded. Normally this would require repetitive magnetic and thermal analysis with realistic coolant flow. However, it is obvious that this would require tremendous computer time and seeking an optimal solution in this manner would not be practical. Therefore an acceptably accurate method yet requiring reasonable computational time is needed.

Note that accuracy of a FE model depends also on the meshing of the geometry and parameters of the solution. To make sure that the developed model has the desired accuracy, verification of its results via tests is required.

To achieve the purpose stated above a reference motor is acquired and tests and simulations are made on it. The following sections explain how an accurate FE base model is developed and verified using this reference test motor.

2.2. Reference Test Motor

The reference test motor is a traction induction motor . Although this motor has no similarity to our motor(that is going to be designed and manufactured as will be explained in Chapter 4), we shall use only this motor to verify the FE techniques that will be used throughout this thesis. The rated performance of the reference test motor is given in Table 2.1.

Table 2.1. *Reference Test Motor Rated Performance Values*

Parameter	*Value*
Voltage [L-L rms]	360
Connection	Y
Current [A rms]	198
Rated Speed [rpm]	1461
Torque [N.m]	648
f [Hz]	50
Output Power [kW]	100
Power Factor	0.87
Stator Outer Diameter [mm]	516
Core Length [mm]	137

2.2.1. Geometry

Reference Test Motor's 3D solid model is provided in Figure 2.1. And the 2D stator and rotor laminations can be easily modeled in FE environment as shown in Figure 2.2. The Geometric details are obtained through measuring the motor components at ELSAN.

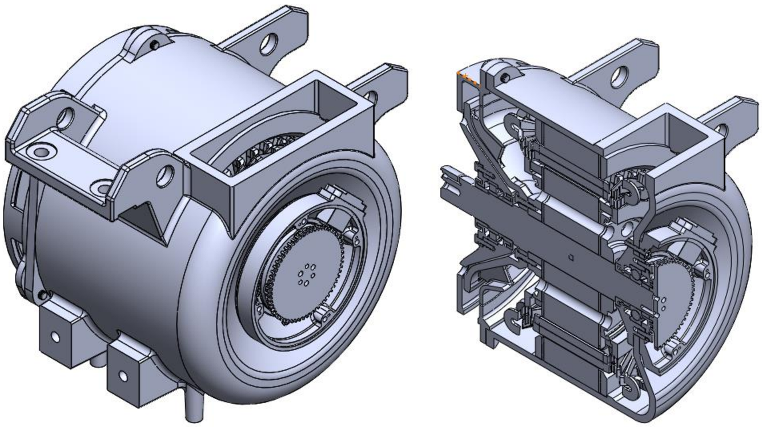

Figure 2.1. Reference Test Motor's 3D Solid Model

2.2.1.1. Main Dimensions

The main dimensions of the reference test motor is included in Table 2.2, and the 2D lamination model is given in Figure 2.2.

Table 2.2. *Reference Test Motor Main Dimension*

Parameter	*Value*
Stator Outer Diameter (D_o) [mm]	516
Stator Inner Diameter (D_i) [mm]	330
Air gap [mm]	1.2
Core length [mm]	137
Stator Slot No	36
Rotor Slot No	46

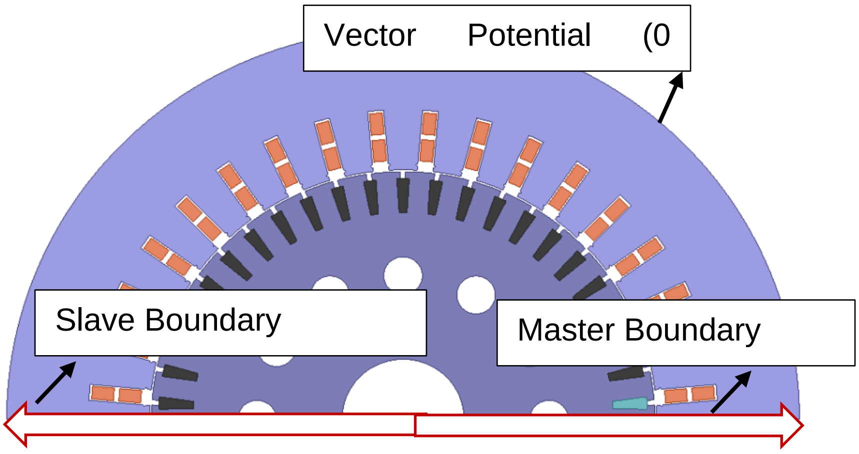

Figure 2.2. Reference Test Motor's Stator and Rotor FE 2D Laminations with Boundary Conditions

2.2.1.2. Stator Slot Information

The slot information is acquired through direct measurement of the stator lamination stack on the motor itself. The slot information is included in Table 2.3, and the parameters are depicted in *Figure 2.3*.

Table 2.3. *Reference Test Motor’s Stator Slot Information*

Parameter	*Value*
Hs0 [mm]	2.2
Hs1 [mm]	2
Hs2 [mm]	37.5
Bs1 [mm]	13
Bs2 [mm]	10.4

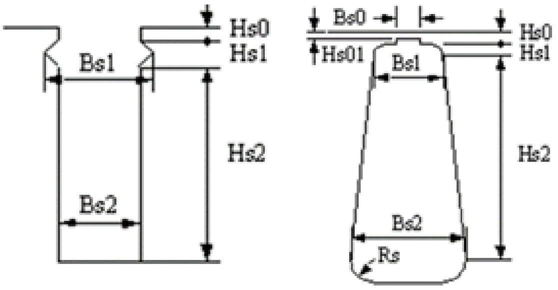

Figure 2.3. *Reference Motor’s: Stator Slot Schematic (on Left), and Rotor Slot Schematics (on Right)*

2.2.1.3. Rotor Slot Information

As explained in previous section, the data regarding slot dimensions is acquired through measuring the laminations. The data with respect to a typical schematic of Figure 2.3 is included in Table 2.4.

Table 2.4. *Reference Motor’s Rotor Slot Information*

Parameter	*Value*
Hs0 [mm]	4.6
Hs01 [mm]	0
Hs1 [mm]	0.4
Hs2 [mm]	21.6
Bs0 [mm]	3.3
Bs1 [mm]	8.1
Bs2 [mm]	5.1
Rs [mm]	0.5

2.2.2. Stator Winding Configuration

The stator winding parameters- including winding layers, parallel branches, conductor per slot, coil pitch, and wire size- are determined as a result of examining the motor, and stator windings structure. However for a FE model to accurately calculate the stator copper loss, the resistance value of the FE model and the motor itself should be approximately the same. For this reason the end length turn is calibrated, and the selected parameters for the FE analysis is included in Table 2.5.

Table 2.5. *Reference Test Motor's Stator Winding Configuration Used in Finite Element Analysis*

Stator Winding Parameters	*Value*
Winding Layers	2
Parallel Branches	2
Conductors per Slot	**7+7**
Coil Pitch	7
Number of Strands	1
Wire Size	Width:8.5mm Thickness:1.5mm
Half Turn Length [mm]	409.0

2.2.3. Rotor Squirrel Cage Configuration

Squirrel cage rotor used in this motor is assumed to be made of a Copper alloy, named Copper Chromium Zirconium abbreviated by CuCrZr. And the data regarding the geometry of the rotor squirrel cage is achieved through inspecting the motor.

As mentioned in [10], and [20] manufacturing cage from copper alloys not only will improve the efficiency by reducing the rotor copper loss, but also improves the mechanical strength and reliability of the motor, which makes it a suitable material for traction applications. If an Aluminum squirrel cage is to be used, assuming the same current density and the same cross section, the conductivity of Aluminum is 38 MS/m whereas the conductivity of CuCrZr used is 47 MS/m , so by using the AL the heat generated is approximately 23 % higher (assuming the temperature remains the same). However by choosing this material the challenge is to create a reliable joint to connect the rotor bar to the end ring. The squirrel cage dimensions are included in Table 2.6, with visual representation in Figure 2.4.

Table 2.6. *Reference Test Motor's Rotor Cage Dimensions*

Rotor Wdg. Parameters	Value	Description
End Length	33 [mm]	single-side end extended bar length
End Ring Width	14 [mm]	width of end rings (in axial direction)
End Ring Height	31.4 [mm]	height of end rings (in radian direction)

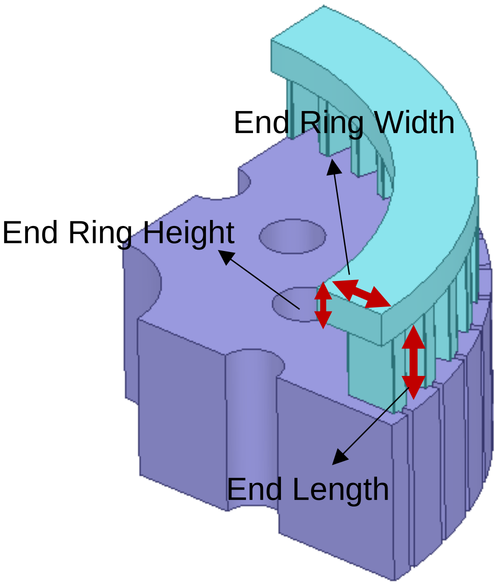

Figure 2.4. 3D Schematic of the Rotor Bar and Rotor End Ring Connection of the Reference Test Motor

Material characteristics of Copper Chromium Zirconium(CuCrZr) related with electromagnetic analysis is included in Table 2.7.

Table 2.7. *Rotor Conductors, Electrical and Mechanical Properties*

Alloy	*Electrical Conductivity MS/m at 25 °C*	*Density kg/dm^3*	*Thermal Coefficient of Resistance 1/°C at 20°C*
CuCrZr	47	8.9	0.00426

In order to determine the resistance of the rotor conductors at various temperatures, thermal coefficient of resistance or "α" is needed. The value selected for the alloy in FE analysis is the same as of copper (0.00426). It is an acceptable assumption considering the fact that the alloy is above 95 % copper. By doing so the calculated rotor copper loss will yield a more optimistic result.

2.2.4. Core Material

Table 2.8. *Core Material used in Reference Test Motor*

Component	*Material*
Stator Lamination	JFE 50JN600
Rotor Lamination	JFE 50JN600

The core material that is used in the actual motor is not known, so a typical core material is selected for this application.

2.2.5. Cooling Method

The motor is using a self-ventilation system via a fan mounted on its shaft. The cooling capacity of the fan while motor is connected to a 50 Hz supply the intake air flow rate is approximately measured at 0.14 m^3/s. The cooling system is shown in Figure 2.19 and Figure 2.20.

2.3. Test Setup

The test setup that has been used in the experiments can be categorized into four main sections. The first part is power supply unit. For this purpose either an external generator or main grid is used. The main grid is fixed on 380-volt, line-line 50 Hz, and to be able to change the voltage level an external generator is being utilized. The generator can be adjusted to act as a sinusoidal source, its output voltage rating and its frequency can be adjusted from. The second test bench component is the electrical measurement device which will be explained in the following paragraph, and the third component is the mechanical load with speed encoder and torque transducer mounted on its platform. Fourth test bench component is the Inverter unit. The VACON inverter that is used is being supplied by 690 Volt rms voltage and is capable of providing a 3 phase voltage up to 690 volt and frequency range of up to 320 Hz, with maximum ampere rating of 261 Amps. The testing platform is shown in Figure 2.5.

Two Different power analyzer devices have been used in measurements. The first device is the HIOKI 3390 Power Analyzer, and the second measuring device is the HIOKI 3194. All of the measurements of the electrical parameters are recorded via the HIOKI 3194 due to its high range band width compared to the other device.

The Mechanical measurements have been logged manually by reading the data output of the loading unit displayed on the panel. The loading unit is fixed throughout the whole testing ranges, which is shown in Figure 2.5 It is a hydraulic dynamometer acting as a loading unit with encoder and torque transducer installed on, so that we are able to read the speed and the torque values at the output shaft of the motor.

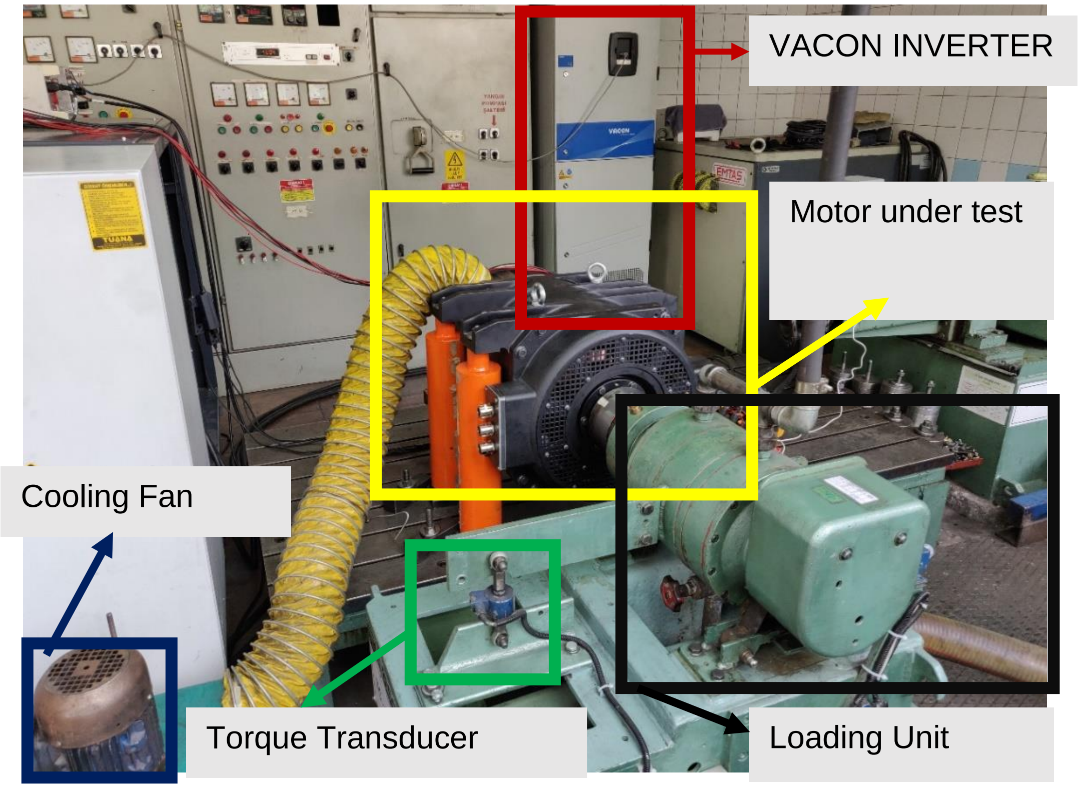

Figure 2.5. Test Setup, Including the Load System, Inverter, and the Motor Under Test

Figure 2.6. Measurement Devices from Left : Hioki 3194, Hioki 3390

2.4. Tests Performed on Reference Motor

Three different type tests have been performed on the motor. Load, no-load, and locked rotor test.

2.4.1. Reference Motor Load Test

For the load test the motor is operated till reaching thermal steady-stated , in which the temperature of the motor (PT100 heat sensors) is approximately constant and does not vary more than 2 °C within an hour. The stator and rotor temperatures are estimated at the end of the test with respect to the IEC standard. The methods used for temperature estimation is explained in Sections 2.4.1.1 and 2.4.1.2.

Table 2.9. *Reference Test Motor 50 Hz-Grid, 648 Nm Load Test Operating Condition*

Parameter	*Value*
Measuring Equipment	HIOKI-3390
Test Type	Under-Load
Main Power Source	Grid
Connection	Y
Rated Voltage [V, L-L]	360
Rated Frequency, [Hz]	50
Rated Torque [Nm]	648
Cooling	Fan (Mounted on the shaft)

2.4.1.1. Stator Winding Temperature Measurement

Temperature estimation is done via resistance method, and it is verified by using PT100 temperature sensor placed at the end winding of the stator. The test detailed procedure is explained in IEC Standard of 60349-2 2010 , Annex A. The test is done by stopping the motor as short a time as possible, and consecutive measurement of the stator resistance is taken. The resistance readings are plotted as a function of time. The resulting curve shall be extrapolated to determine the average resistance of the winding at the commencement of cooling. And the temperature of the winding at the operating instance can be estimated.

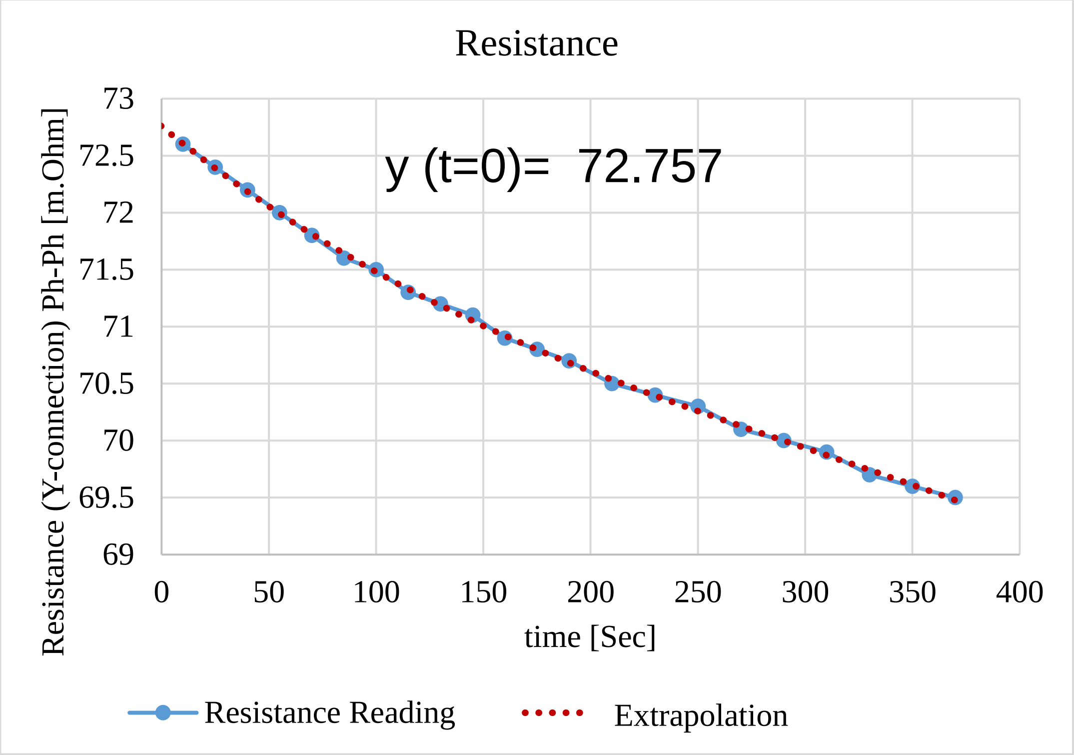

*Figure 2.7.*Temperature measurement based on the resistance method, 50 Hz, 648 Nm, Sinusoidal Source (Solid Blue- Resistance Readings, Dotted Red- Extrapolated Curve)

And based on the extrapolation on the data in Figure 2.7, the stator resistance is estimated for the test motor to be 36.38 m.Ω, which corresponds to 163 °C.

2.4.1.2. Rotor Cage Temperature Measurement

Rotor conductor temperature estimation is based on the warm and cold slip of the motor. And as the name suggests , the slip of the motor is measured at the very beginning of the test, and as the motor reaches steady state, the speed drops and a warm slip is logged. Rotor's temperature is estimated based on Equation (2-1).

Electromagnetic torque in an induction motor can be calculated as in the following equation:

$$T = \frac{3 \times r_2' \times i'^2_2}{s \times \omega_s} \tag{2-1}$$

The rotor resistance is linked to the other parameters via the above equation. If the torque is kept constant during the test , and assuming that i'^2_2 approximately remains the same the relationship given in Equation (2-2) between the hot and cold resistance values.

$$\frac{r'_{2-T1}}{r'_{2-T2}} = \frac{s_{T1}}{s_{T2}} \tag{2-2}$$

The relations for the resistance change with the temperature is known :

$$\frac{r_2}{r_1} = \frac{T_1 + 234.5}{T_2 + 234.5}\ (For\ Copper\ Conductors) \tag{2-3}$$

And so we can easily derive the following equation :

$$\frac{s_{T1}}{s_{T2}} = \frac{T_1 + 234.5}{T_2 + 234.5}\ (For\ Copper\ Conductors) \tag{2-4}$$

Term S_{T1} is the motor slip at temperature T_1, and since other variables are already measured, T_2 can be calculated which is the rotor temperature at thermal steady-state mode of operation.

As mentioned in 2.2.3 at Table 2.7 the thermal coefficient of resistance for the CuCrZr alloy assumed to be the same as copper, and because of that in Equations (2-3), and (2-4) the constant (1/α) for copper at 20 °C is “234.5”.

2.4.1.3. Load Test Results

Reference Motor’s test result is included in Table 2.10

Table 2.10. *Performance Comparison under Rated Load 50Hz 100kW*

	Test Result Thermal S.S	FEM 2D	Description
Voltage(rms),	372.24	373	Line-Line
Connection	Y	Y	
Current (A rms)	197.9	194.0	
Shaft r.p.m	1461	1463	
Torque (N.m)	648	649.8	
Input Power(kW)	110.66	107.07	$Va(t)Ia(t) + Vb(t)Ib(t) + Vc(t)Ic(t)$
Power Factor	0.867	0.85	$\cos(\varphi) = Pin \div (3 \times Vph \times Iph)$
Output Power(kW)	99.17	99.55	
Direct Total Power Loss (kW)	11.48	7.52	P in - P out
Indirect Total Power Loss (kW)	10.057	9.015	P cu, s+Pcu, r+Pcore+Pf&w+Pstray
Direct Efficiency %	89.6	92.9	P out / P in
Indirect Efficiency %	90.8	91.6	(P out)/ (P out + P loss)

As it can be seen form Table 2.10 there is a good agreement between the performance parameters. However there is a noticeable difference on the direct total power loss when comparing the FEA and the measurement data. Direct total power loss is defined as the output power subtracted from the input power. The reason of this difference is the fact that that input power in FEA does not include all the loss component and does not reflect the actual input power to the system, because of two reasons first reason is the core loss calculation method in ANSYS MAXWELL which is selected as a post processing operation, meaning the core loss will not affect the solved parameters and calculated after each iteration is solved, as this result the effect of the core loss won’t be considered in current estimations and the input, and the second reason is the mechanical loss components namely friction and windage losses, which are not present is a FE environment.

Another method for measuring the total loss is the indirect methods, in which all the loss components are calculated individually and added up to determine the “indirect total power loss”. By using this method, total losses of FEA and test results will be much closer.

In test results while calculating the total power loss through direct and indirect method, there exist a difference between the two methods. This difference is due to the core loss calculation and the stray load loss estimation methods. The core loss achieved through no-load operation, is lower than core loss under load. And the stray loss is estimated through constant percentage of input rather that accurate measurement.

2.4.1.4. Loss Segregation Under Load

Measurement data are recorded at an instance in which the motor has reached a thermal steady state. So that the resistance measurement at the end of the test reflect the actual temperature of the stator winding.

Table 2.11. *50Hz 100kW 648 Nm Load, Loss Components’ Comparison*

	Test	FEM 2D	Description/ Definition
Input Power(kW)	110.6	107.07	Absorbed power
s	0.026	0.025	Slip
$P_{cu,\, s}$ (kW)	4.27	4.27	Stator copper losses
Pf_e (kW)	2.23	1.76	Core loss
P_{stray} (kw)	0.55	-	P stray = 0.005 × P_{in}
$P_{cu,r}$ (kW)	2.69	2.68	Rotor conductor losses= P (rotor bars) +P (end rings)
P_{mech} (kW)	0.305	0.305	Mechanical Losses(f&w)
Solid Loss (FEM)[kW]	-	1.61	Ohmic loss in “rotor bars”
$P_{er,\, rotor}$ (kW)	-	1.076	Rotor end rind ohmic loss (calculated analytically)
P_{total} (kW)	10.057	9.015	Ptot=Pcu, s+Pcu, r+Pfe+Pmech+Pstray

In comparing the loss values between the measurement and FEA, all components except core loss are closely matching. First reason for this is the fact that the material used is not exactly known, and the second one is the ANSYS Maxwell calculation method which estimates core loss as a post process.

2.4.2. Reference Motor No-Load Test

The No-Load measurement is performed based on the standards regarding the polyphase induction motors (either IEC or IEEE), in which motor is operated at no-load while taking measurements as you gradually decrease the voltage from approximately 125% rated voltage. and plotting the power with respect to voltage to determine the core loss and mechanical losses. In order to properly calculate the friction and windage loss as well as No-Load core loss, cold resistance is measured at the very beginning and before each test, temperature is measured through resistance method before and after the test, in addition two PT100 sensors' data are logged to verify the data provided by resistance measurement method. The resistance measurement is detailed in Table 2.12.

As seen in Figure 2.8 by fitting a linear line at the bottom linear portion of the curve (Dot-Dashed Red Line) the mechanical losses can be easily determined. And consequently, core loss at the desired voltage rating can be calculated. The results for the test voltage are included in Table 2.13.

Table 2.12. *Test Motor Temperature Estimation Based on Measurement @ No-Load Test 50 Hz, Grid*

Reference Test Motor	*Before Test*	*After Test*
Ambient Temperature	-	20.1 ˚C
Resistance per Phase	-	23.73 mΩ
Avg. St. Winding Temperature	-	25.5 ˚C
PT100 #1 / #2	-	25 ˚C / 25 ˚C
Test Duration	9 Minutes	

No-Load Core Loss Estimation:

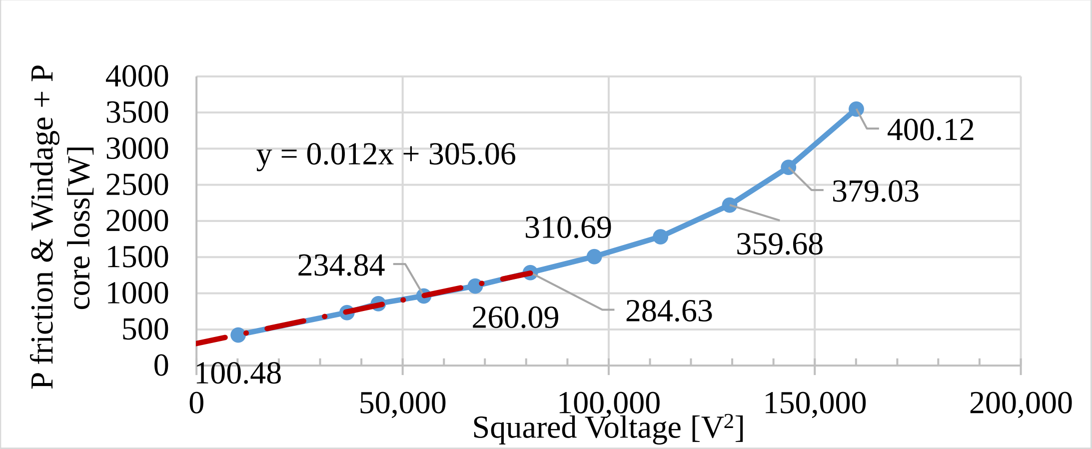

Figure 2.8. No-Load P-V Curve Based on Measurement Data, Under 50 Hz Sinusoidal Source ,Test Motor ,(x-axis is Squared Voltage, Data Points on the Plots are the Voltage Levels)

Table 2.13. *50 Hz,372 Volts, Test Motor No-Load Core Loss under Sinusoidal Source*

	Voltage	F [Hz]	Resistance	Temp.	Current [A]	P mech [W]	P iron [W]
Test result	372.2	50	23.73 mΩ	25 ˚C	76	305	2232

2.4.3. No-Load Test – Parameter Extraction

In a no-load test rotor is rotating at a speed approximately the same as the supplied frequency, and as the result the “slip” value becomes very small. If it is to be referred to induction motor equivalent circuit, it can be noticed that this will lead for the active input power to be distributed among the core loss resistance and the stator resistive loss. So, the parameters can be extracted from the measurement data taken.

$$S_{nl} = 3 \times V_{nl} \times I_{nl} \tag{2-5}$$

$$Q_{nl} = \sqrt{{S_{nl}}^2 - {P_{nl}}^2} \tag{2-6}$$

$$X_{nl} = \frac{Q_{nl}}{3 \times {I_{nl}}^2} \tag{2-7}$$

$$X_{nl} = X_1 + X_m \tag{2-8}$$

$$P_{nl} = 3 \times R_s \times {I_{nl}}^2 + P_{core} \tag{2-9}$$

$$R_c = \frac{{I_{nl}}^2}{P_{core}} \tag{2-10}$$

The results are included in Table 2.14.

Table 2.14. *No-Load Test Parameter Estimation 50Hz*

Ohm	Measurement @17˚C	FEM 2D @ 25˚C	RMxprt @ 25˚C
rs	0.023	0.0249	0.0249
X_{nl}	2.84	2.98	2.4
Rc	49	50.2	56.8

Regarding the data presented in Table 2.14 motor is assumed to be at ambient temperature of 25˚C during the test.

2.4.4. Reference Motor Locked Rotor Test

Based on IEEE and IEC standards , the motor's been locked, and locked rotor measurements performed on the motor. In Table 2.15 R_{LR} is the total stator and rotor resistance, and r_2' is the per phase rotor resistance estimated from the test. The locked rotor test loss is P_{LR} , and X_{LR} is the total reactance which is the summation of the rotor and stator reactance in the equivalent induction motor circuit .

P_{LR}= total input power – core loss = Stator copper loss + rotor copper loss =4920 W

Table 2.15. *Locked Rotor Test Results, on the Reference Test Motor at 50 Hz*

Parameter	Value
R_{LR}	0.050
r_2'	0.0251 @ 25°C
Z_{LR}	0.192
X_{LR}	0.186

The locked rotor test is also performed in 2D FEA, the comparison results are included in Table 2.16.

Table 2.16. *Locked Rotor Parameter Estimation 50 Hz*

	Measurement	FEM 2D	RMxprt
R_{LR}	0.059	0.050	0.054
X_{LR}	0.164	0.186	0.135
Z_{LR}	0.1743	0.192	0.143
r_1	0.023	0.0249	0.0249
r_2	0.036	0.02589	0.0252

2.5. Finite Element Modelling

For modelling and simulating this prototype, as mentioned throughout the text, Finite Element analysis have been utilized (ANSYS Maxwell software). However for a FE model to be accurate enough, reliable enough, and fast enough there are parameters than need to be configured properly.

2.5.1. Boundary Condition

Regarding the computational time the symmetry boundary condition is used to reduce the complexities of the model and reduce the solution time, however since the Electrical machine used in this study comprised of 36 stator slots and 46 rotor slots, it does not allow us to use the per pole symmetry, and we are forced to use one pole pair for the analyses. And for this purpose, a Master/Slave Boundary condition has been defined as well as a vector potential. The boundary conditions are shown in Figure 2.2

In this figure two red vectors represent the Master/Slave Boundaries, and the vector potential is the outer layer of the stator representing the active area for FE solution.

2.5.2. Excitation

There are two main modules used in the simulation model, the first one is the “Voltage Excitation” used for the stator 3-Phase winding arrangement. And the second one being the “End Connection” representing the end connection and electrical properties on how 2D rotor bars will interact with each other and the stator end windings should be considered.

2.5.2.1. Stator 3-Phase Winding Arrangement

A typical setting for Phase-A of a 50Hz pure Sinusoidal excitation as an example is included in Table 3.9. The simulations used in this study uses sinusoidal excitation unless mentioned otherwise.

Table 2.17. *FE 2D Stator Winding Voltage Excitation*

Parameter	*Value*
Type	Voltage
Initial Current [A]	0
Stator Phase Resistance [mΩ]	38.18
End winding Inductance [H]	1.33e-04
Voltage	303.7 × sin(2×pi×50×time)
Number of parallel branches	2

The inductance included in this table is the stator end winding leakage inductance (including both sides) which is modeled as an external element which is shown in Figure 2.10

2.5.2.2. Rotor Squirrel Cage

Rotor conductors (bars, and short circuit end rings) are modelled in FE in two separate parts. The rotor bars are included in the 2D FE model itself, however the rotor end rings, and the extensions of the rotor bars are included in the model through their resistance and inductance values as external parameters. These parameters are calculated analytically and imported to the FE model. Rotor end connection can be seen in Figure 2.9. And the values for the Reference Test Motor are included in Table 2.18.

Table 2.18. *Reference Test Motor's Rotor End Connections Parameters*

Parameters Imported	Value
End Resistance between Adjacent Conductors [Ohm]	1.85e-06
End Inductance between Adjacent Conductors [H]	6.64e-09

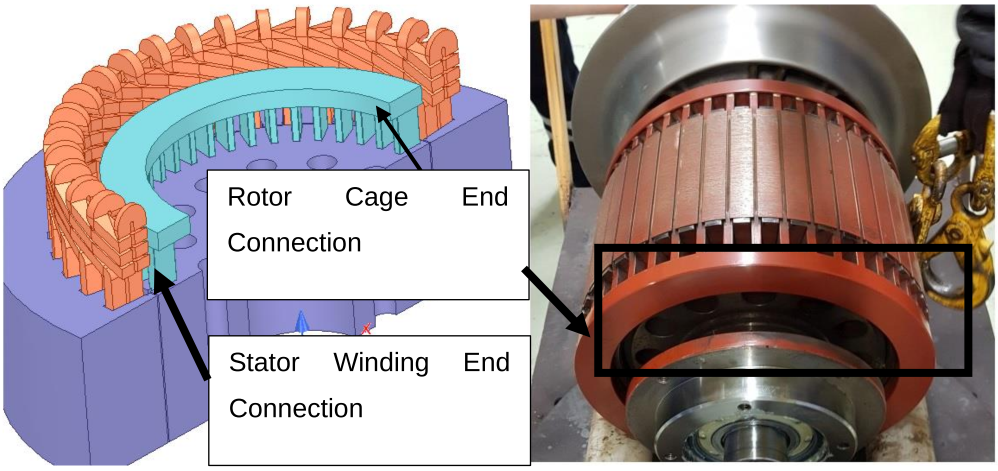

Figure 2.9. Stator and Rotor's End Connections. From Left: 3D Representation of the End Connections, Reference Test Motors's Rotor and its Copper Cage

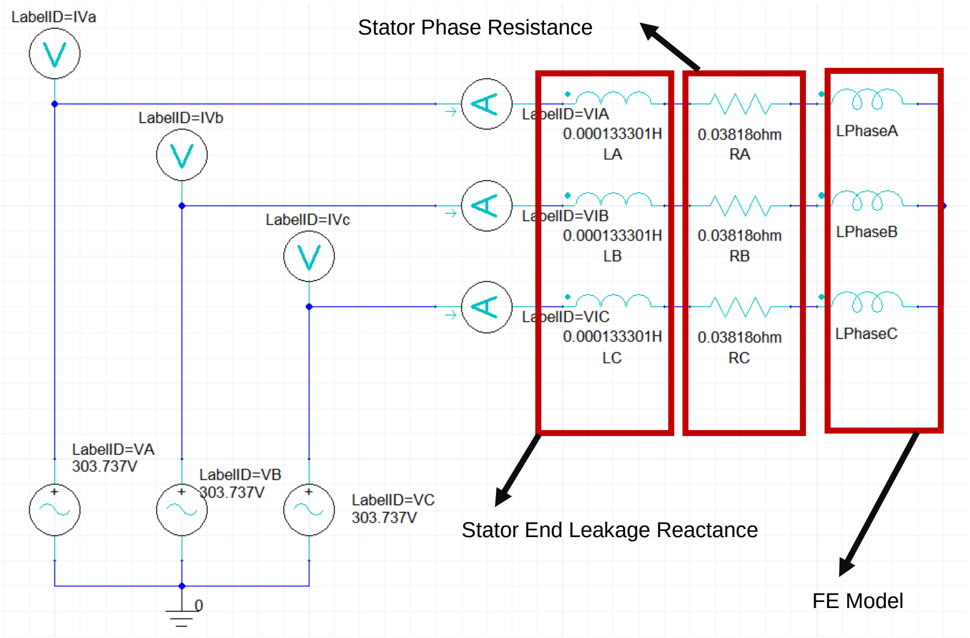

Figure 2.10. A Typical External Circuit with End Winding Parameters Used by FE Calculations

2.5.3. Meshing

Maxwell generates an initial mesh, which includes surface approximation settings. Mesh operations are used to refine the mesh elements (maximum element size, maximum element number). If you are performing an adaptive analysis, Maxwell uses the current finite element solution to estimate the regions of the problem domain where the exact solution has strong error. Tetrahedra in these regions are refined. Maxwell generates another solution using the refined mesh. Maxwell recomputes the error, and the iterative process (solve — error analysis — adaptive refinement) repeats until the convergence criteria are satisfied or the maximum number of adaptive passes is completed.

The solution type being used in the modeling is the transient mode in which the adaptive meshing is not allowed. However in a magnetostatics mode we can use the adaptive meshing and link the mesh to the transient mode. The adaptive mesh gives us an idea of what should be the maximum element size in each subject.

As a result at a specific time, motor is frozen, and the magnetostatics problem is solved on the motor with adaptive meshing. Based on the data acquired, final mesh sizes is determined. The mesh elements that are used for simulating the reference test motor is at Table 2.19.

Table 2.19. *Reference Test Motor Mesh Numbers in Various Motor Parts*

Mesh Refinement	*Maximum Element Length*	*Mesh Elements*
Air gap	0.15 mm	73084
Bars	2 mm	4830
Rotor	4 mm	28977
Stator	4.5 mm	15155
Sum	-	128269

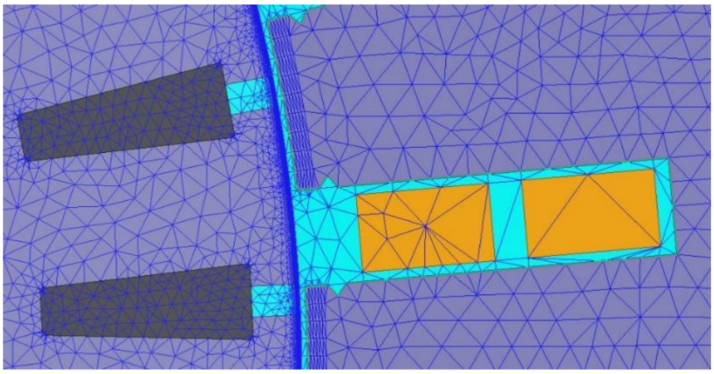

Figure 2.11. Reference Test Motor 2D FE Mesh Elements

2.5.4. FE Solution Setup

The Transient setup and time settings are defined based on the time it takes the waveforms to reach steady state. The most important parameter in the solution setup is the nonlinear residual. This value specifies how close each solution must come to satisfying the equations that are used to compute the magnetic field. Table 2.20 presents the values used in this study.

In order to speed up the computational time, only one electrical period is being solved after system reaches steady state, however in order to do so a coarse time step is chosen to reach this steady state point much faster. By doing so the computational time dramatically decreases.

Table 2.20. *FE Solution Time Setup Configuration*

Setting	*Value*
Stop time	0.15
Time step	Table 4.9
Nonlinear residual	1e-08
Nonlinear iteration per time step	8~10

Table 2.21. *Adaptive Time Step Setting*

Time Ranges [sec]	*Time Step*
[0, 0.1)	800 µs
[0.1, 0.12)	400 µs
[0.12, 0.13)	200 µs
[0.13, 0.15)	50 µs

The system used for solving the FEA is summarized Table 2.22

Table 2.22. *Computer Configuration Used for FEA*

Component	*Configuration*	*Frequency*
CPU	Intel Xeon E3-1270 v6 4 Cores	4.2 GHz 1C/ 4.0 GHz 4C
RAM	32 GB	DDR4-2400 (1200MHz)
Hard Disk	SSD-256GB	SATA-III 6.0 Gb/s

2.5.5. Finite Element Analysis Simulation Results

In order to verify the simulation model, the results need to be verified with the test data. A FEA 2D transient model is constructed as explained in Sections 2.5.1 to 2.5.4. The model uses voltage excitation as included in Table 2.17 and the test condition is briefed in Table 2.23.

Table 2.23. *Operating Condition – Rated Load 648 N.m, 50 Hz, 360 Volt*

Operating Condition	Maxwell 2D
Stator operating temperature[°C]	163
Rotor operating temperature[°C]	120
Voltage Ref. [V], (L-L), rms	360
Frequency [Hz]	50
Output Power[kW]	100

The temperature data for FEA is obtained from the measurements. The performance and loss components results are included in Table 2.10 , and Table 2.11.

Table 2.24. *Full Load Stator Resistance Comparison, 100kW 50Hz*

Stator Resistance	Test	FEM 2D
Ambient Temp	0.023 (17 ˚C)	0.024 (20 ˚C)
Operating Temp	0.0363 (163˚C)	0.03818 (163˚C)

The parameters in Table 2.10 ,and Table 2.11 regarding the FEA are obtained while in steady state. For example the motor torque is plotted in Figure 2.12 the plot represent the electrical transient of electromagnetic torque in the FE model.

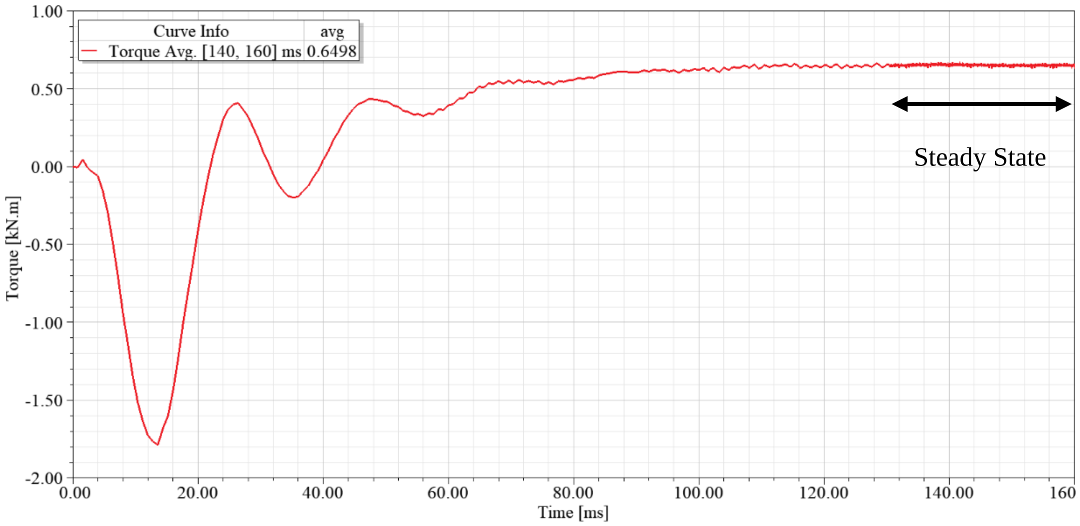

Figure 2.12. Reference Test Motor 2D FE , Progress of Torque Output, 50 Hz Sine Excitation

2.5.5.1. FEA Loss Calculation

The individual loss components are calculated in in included in Table 2.11 the stator copper loss calculation is trivial; however as included in Table 2.23 stator operating temperature is known and it is calculated as "R × I^2".

The rotor cage in FE 2D is modeled partially through FE environment and partially through external circuit. In order to calculate the overall rotor copper loss for our FE model as included in Table 2.25the end ring copper loss is calculated analytically.

$$i_{bar} = \frac{2 * N_s * k_{ws} * m_s}{Q_2} \times i_2' \tag{2-11}$$

$$i_2' = i_1 \times cos\varphi \tag{2-12}$$

$$i_{er} = \frac{Q_2}{p \times \pi} \times i_{bar} \tag{2-13}$$

$$R_{er} = \frac{\rho \pi D_m}{A_{er}} \tag{2-14}$$

$$P_{er} = 2 \times R_{er} \times {i_{er}}^2 \tag{2-15}$$

As all the details are knows the end ring copper loss can be easily determined. The term "i_{bar}" is the rotor bar current, $k_{\omega s}$ refers to the winding factor of the stator. And Q_2 is the rotor bar number, which in our case Q_2=46. Currents i_1 and i_2' refer to stator phase current and rotor side phase current respectively. "p" here in Equation (2-13) refers to the pole number. Equation (2-15) is used to calculate the end ring resistance, D_m being the average end ring diameter, and A_{er} being the end ring cross section. The calculated results are in Table 2.25.

Table 2.25. *Reference Motor's Rotor End Ring Analytical Calculations, 100kW 50Hz*

Rotor Cage Properties	Input to 2D FE Model
Cage resistivity at 120 ˚C	2.96e-08
Rotor bar length [mm]	203
End ring cross section [mm^2]	439.6
Bar Current [A]-analytical	813.0
End ring Current [A]	2976.1
End ring resistive loss @120 ˚C [W]	1076.2
πD_m (end ring length) [mm]	901.0
Bar conductor area [mm^2]	148.17
Bar Current Density [A/mm^2]	5.48
Rotor Ring Current Density [A/mm^2]	6.76
Stator series turns per phase	42

Stray load loss component is specific to the test results as it is defined by the standards, however in FE calculations the loss components due to the higher order harmonics in the air gap flux density variation is already included in the core loss component. And so for calculating the indirect total power loss it is not added as a FE loss value.

2.5.5.2. FEA Magnetic Flux Density

As stated earlier in this chapter, the purpose of this model is to act as a reference design point for the later variations. For this purpose the simulated motor that is compared with its test results and verified, will be further analyzed and investigated to create design constraints for further modifications.

In order to calculate the magnetic flux density, motor's various cross sections have been selected which is shown in Figure 2.13.

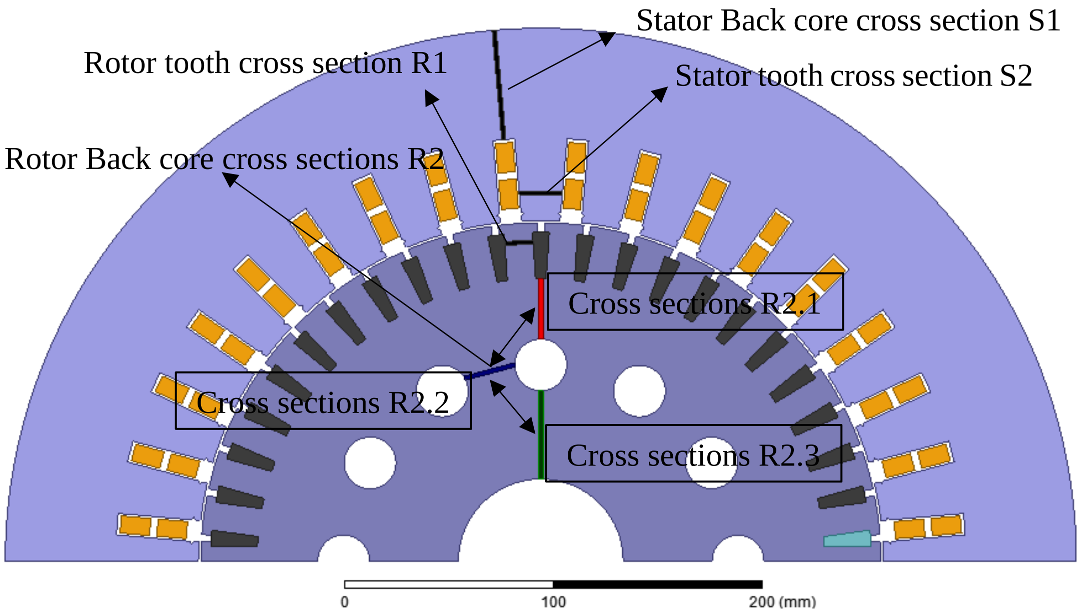

Figure 2.13. Cross Sections for Flux Density Distribution Measurement on Critical Sections

In order to acquire the flux density distribution along these cross two different waveforms are obtained, first one is the flux density time variation as in Figure 2.14,

Figure 2.15, and Figure 2.17 and the second one is the flux density distribution at one time instance along a specified cross section as in Figure 2.16, and Figure 2.18. The B values are obtained in the calculator tool of the ANSYS MAXWELL, and it is assumed that the B distribution is mainly comprised of normal component.

Air gap Flux Density:

Air gap flux density or magnetic loading has been calculated analytically. Since we know the flux per pole value it is trivial to calculate the magnetic loading as like Equation (2-17). The integration line is shown in Figure 2.13 as "*S1*".

$$\varphi_{pole}/_{2} = core\ length \times \int B.dS1\ ;\ S1 \stackrel{\text{def}}{=} integration\ line \qquad (2\text{-}16)$$

$$\bar{B}_{gap} = \frac{P \times \varphi_{pole}}{\pi \times D_i \times l_{core}} \qquad (2\text{-}17)$$

The flux density distribution alongside the airgap periphery can be obtained through ANSYS MAXWELL calculator on a line spaced in the middle of the air gap. The obtained curve will be later used in an FFT analysis to calculate the harmonic content and higher order loss components. The plot is shown in Figure 2.14.

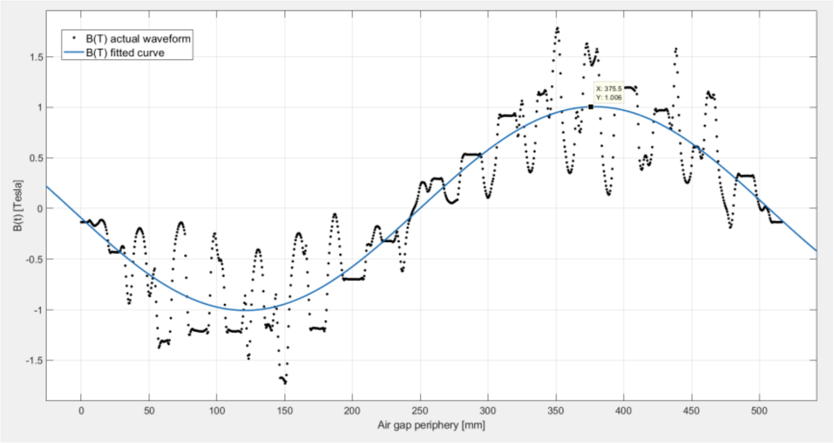

Figure 2.14. 50 Hz 100kW Rated Condition Flux Density Distribution @ t=0.4 s at Steady State

Stator Back Core :

Stator yoke flux density is measured at a cross section “S1” shown in Figure 2.13. To acquire the mentioned plot, magnetic flux density is averaged at each time step along the “S1” line and creates a single point on Figure 2.15, in order to achieve Figure 2.15 model is operated for one electrical period and averaged data point are plotted with respect to time. However in order to further investigate the B variations, the motor is frozen at a single time step and B’s variation along the distance of the cross-section line is captured. For example rotor “R2.2” cross section’s B variation is plotted in Figure 2.16.

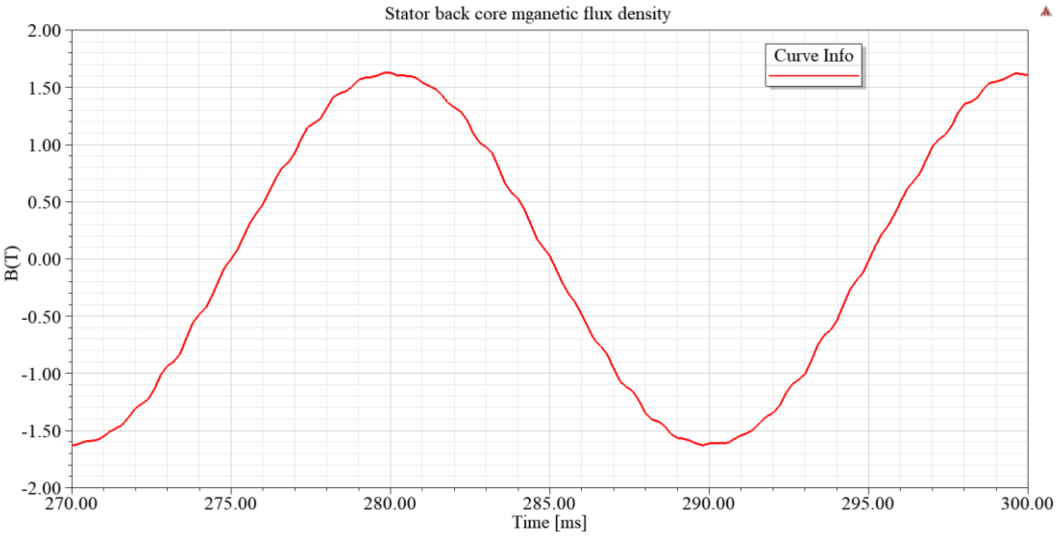

Figure 2.15. Averaged Stator Back Core Flux Density Along the “*S1*”Cross Section” w.r.t Time

Rotor Back Core:

Due to the ventilation implemented in the rotor back core , there is not a uniformly distributed rotor back core flux density distribution. For this purpose as shown in Figure 2.13 three different cross sections of “*R2.1, R2.2, R2.3*” have been selected.

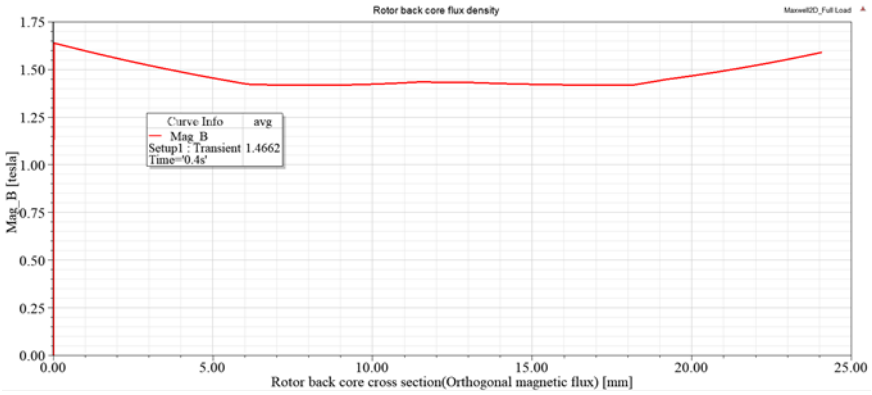

Figure 2.16. Rotor Back Core Flux Density @ t=0.4 s Along the "*R2.2*"Cross Section Directed Radially from Center Towards Outside

Time varying magnetic flux density distribution along all three "*R2.1, R2.2, R2.3*" cross sections is seen in Figure 2.17.

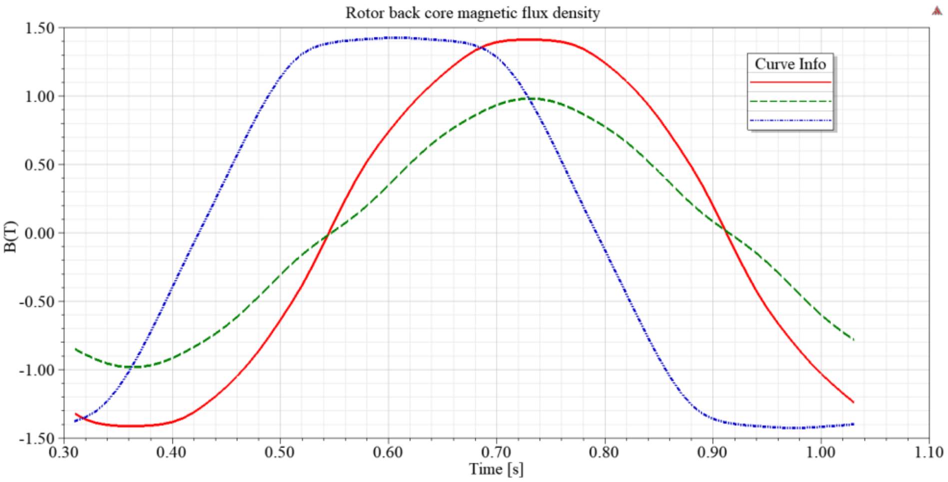

Figure 2.17. "Averaged Rotor Yoke Flux Density along the Cross Sections" w.r.t Time (Solid Red- R.1, Dot Dash Blue- R2.2, and Dashed Green- R2.3)

Rotor Tooth:

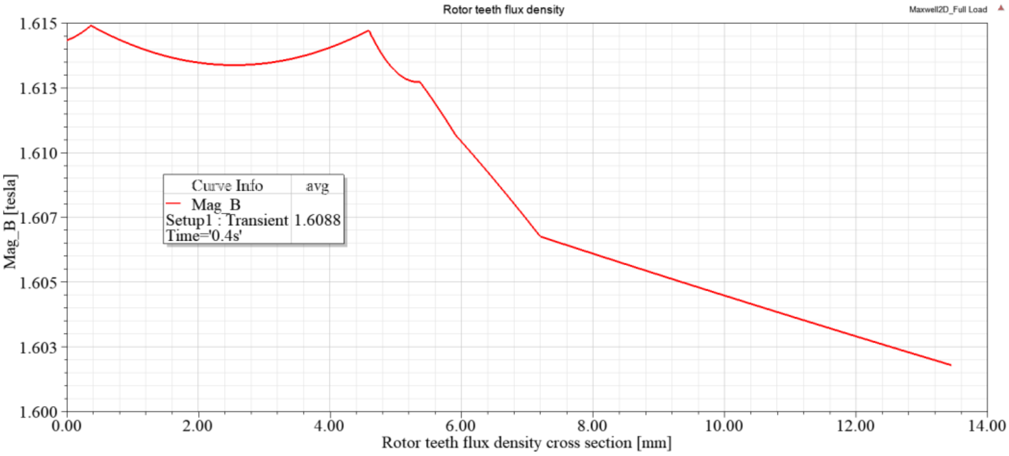

Figure 2.18. Rotor Tooth Flux Density @ t=0.4 s over "*R2*" Cross Section

The magnetic flux densities over specified cross sections is included in Table 2.26. These values will be later used as the reference values for the design of the new traction motor.

Table 2.26. *Magnetic Flux Density Critical Values at Full Load 100kW 50Hz*

	B peak(Tesla)		B average(T)	
	RMxprt	FEM 2D	RMxprt	FEM 2D
Stator-Teeth Flux Density (T) -S2	1.37	1.51	0.87	0.96
Rotor-Teeth Flux Density (T) -R1	1.7	1.6	1.08	1.01
Stator-Yoke Flux Density (T) -S1	1.67	1.63	1.06	1.04
Rotor-Yoke Flux Density (T) R2.2	1.1	1.47	0.7	0.94
Air-Gap Flux Density (T)	0.97	1	0.61	0.64

Table 2.26 represent the peak value of the flux density waveform plotted against time at each cross section. And in calculating the B $_{\text{average}}$ it is assumed the flux density waveforms are sinusoidal and so the B $_{\text{average}}$ is calculated as $\frac{2}{\pi} \times B_{peak}$.

2.6. Thermal-Fluid Flow Modelling, Analysis, and Verification

For a successful motor design, thermal performance of the motor is important. For this reason, thermal analysis of the reference test motor is performed to develop a model to predict the temperature values recoded in tests. The model developed will later be used to predict the performance of the new traction motor design. The 3D drawing of the motor is included in Figure 2.1.

The Reference Test Motor design is cooled with a fan installed on the shaft of the motor shown in Figure 2.20. This motor is tested at full load condition (50Hz, 650Nm) until it reached thermal steady state. From the measurements the distribution of motor loss is obtained through loss segregation method based on Standard IEC 60439-2:2000. The losses of this motor in its various parts are given in Table 2.27 in first column, The loss per unit volume of the related part is tabulated in third column of the same table. During the tests the air intake to the motor is also measured as 0.14 m3/s.

In thermal analysis of the motor . However the fan shape is not accurately known, for this reason a fan is modeled in the motor fluid flow model and shaft speed is increased until the fan in the model gives the same air flow rate at intake as measured.

2.6.1. Reference Test Motor’s Fluid Flow and Thermal Analysis

In a CFD (Computational Flow Dynamics) analysis, the motor’s 3D geometry is known, so a fluid analysis is performed to simulate the air flow. By changing the characteristics of the model we were able to achieve the same air flow in the simulation model as the measurement data. Once the desire air flow rate is achieved , heat sources are determined based on the electromagnetic analysis and a thermal analysis is performed to estimate the temperature as various parts of the model.

Table 2.27. *Heat Generation in Parts of the Reference Test Motor, Based on Measurements-Loss Segregation Method*

Motor Part	Type of Loss	Loss Value[Thermal Analysis] [W]	Object's Volume [dm3]	Loss Value[Thermal Analysis] [w/dm3]
Stator	Core Loss	2036	14.13	144.1
Stator Winding	Copper Loss	4039	2.58	1565.5
Rotor	Core Loss	640	8.58	74.6
Rotor Cage	Copper Loss	2598	2.31	1124.7

The thermal properties of the materials used in the electromagnetic design are included in Table 2.28.

Table 2.28. *Reference Test Motor's Components Thermal Properties*

Motor Components	Material	Density [g/cm3]	Thermal Conductivity[W/m.˚K]
Stator and Rotor Laminations	JFE 50JN600	7750	28 Radial- 0.37 Axial
Rotor Cage	CuCrZr	8900	320
Stator Winding	Copper	8900	401

The model under investigation, regarding its output air ducts and rotor cooling channels is shown in Figure 2.19 and Figure 2.20.

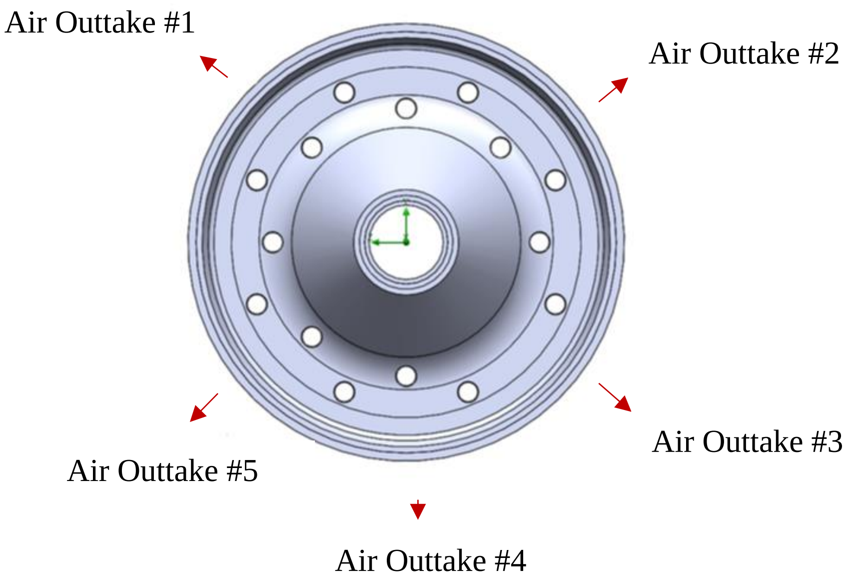

Figure 2.19. Hot Air Exit Channels of the Motor on End of Frame

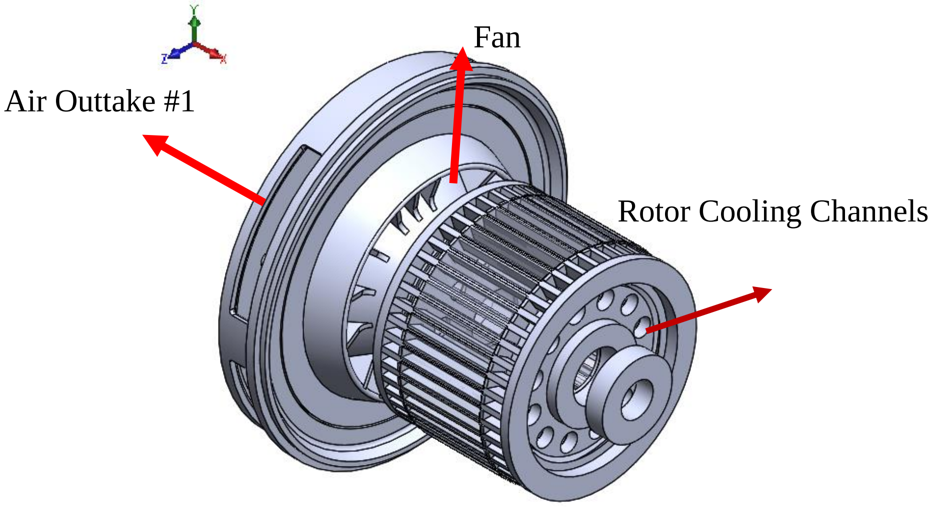

Figure 2.20. Motor, Fan, and Exhaust Outtakes' Geometry on Reference Test Motor

Thermal analysis is made with loss values in

Table 2.27, while the motor is rotating at rated speed of 1460 rpm. However it is found that the air flow at this condition is much lower than experimentally recorded of 0.14 m^3/s flow rate as seen in Table 2.29 (Intake column) . Shaft speed is increased as seen in Figure 2.21 until the same flow rate is achieved as with the experiment. And thermal analysis is repeated at that speed.

Table 2.29. *Intake-Outtake Air Flow, Total Static Pressure, Rotor Cooling Duct' Temperature and Mass Flow Rate Values for the Reference Test Motor- (Simulation Model)*

	Intake	Air Outtake #1	Air Outtake #2	Air Outtake #3	Air Outtake #4	Air Outtake #5
Air Flow velocity Simulated / Measured [m/s]	4.1 / 5	16.5 / -	17.9 / -	16.3 / -	16.5 / -	16.4 / -
Air Flow rate[m^3/s]	0.1367	0.0346	0.0383	0.0301	0.0298	0.0285

Table 2.30. *Rotor Cooling Channels and, Airgap Air Flow in "Reference Test Motor" Under 1800 rpm Fan Speed*

Type of Travel	*Average Air velocity [m/s]*	*Mass Flow Rate [m^3/s]*
Rotor Cooling Channels	17.5 per channel	0.107- (12 Channels combined)
Air gap	0.016	18.2

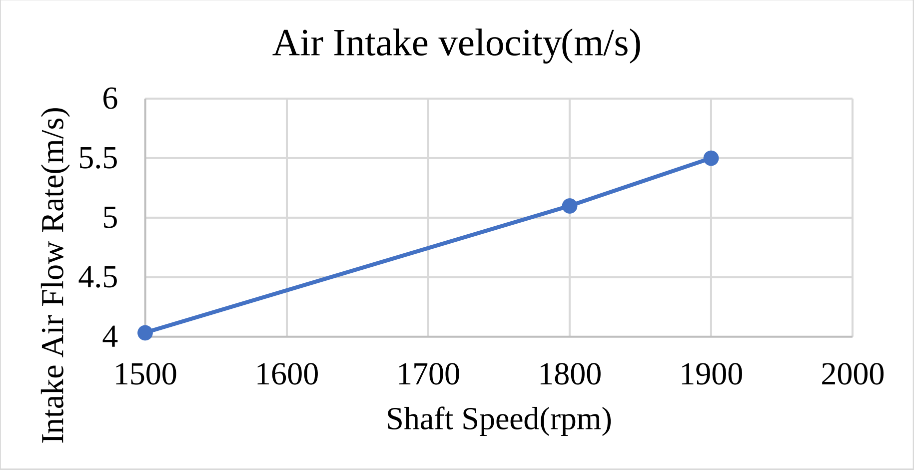

Figure 2.21. Improved Air Intake Flow Rate Variation w.r.t Fan Rotational Speed in the Improved Model – on the Simulation Model of the Reference Test Motor.

The final temperature of the components as the result of the CFD analysis after improving the model and using the rotational speed of 1800 rpm is shown in Table 2.31

Table 2.31. *Reference Test Motor, Components' Temperature as the Result of the Fluid Flow Analysis and Air Intake Flow Rate of ~5m/s @ 1800 rpm Fan Speed-(Simulation Model)*

	Loss [W]	*Average Temperature [˚C]*	*Minimum Temperature [˚C]*	*Maximum Temperature [˚C]*
Stator Winding	4039	181.6	118.5	197.58
Stator Core	2036	188.5	158.8	197.5
Rotor Core	640	158.3	140.2	194.3
Rotor Cage	2598	170.6	156.3	186.8

2.6.2. Temperature Measurements on Reference Test Motor

Given the loss values provided, which are acquired from the measurements, temperatures of the components are also calculated using the measured data. For this purpose the motor has been operated in order to reach the thermally steady state point. After which the temperature of the parts will not vary by ± 2 Degree Celsius within one-hour time frame as stated in the Standard IEC 60439-2:2000 .

As the result of the calculations the temperature of the motor parts are as included here in Table 2.32.

Table 2.32. *Steady State Temperatures of the Component in Reference Test Motor based on the Measured Values at ELSAN- Intake Air Flow @ 0.14* m^3/s

	Measured Average Temperature [˚C] based on Tests[17-05]	*Estimated Average Temperature [˚C] based on Thermal Simulation Model*
Stator Winding	163	181.6
Stator Core	163	188.5
Rotor Core	120	158.3
Rotor Cage	120	170.6
Intake Air Flow Rate [m^3/s]	-	0.14 m^3/s

The temperature data estimated using the measurement data is not reliable, since the method used for temperature estimation is highly sensitive on the slip measurement. Comparing the results of simulation model and the measurement shows the trend. However further work can be done to more accurately estimates the temperature on both the test setup and the simulation model.

It is assumed that since the motor is in thermal steady state; stator core is at the same temperature as the stator winding and that the rotor core is at the same temperature of rotor cage.

It can be seen by comparing Table 2.29 , and Table 2.32 that we were able to get a fluid flow model that is accurate in terms of air flow rate set at 0.14 m^3/s.

2.7. Conclusion

In this chapter a FE model regarding an electromagnetic design was developed and verified. The FE calculation methods used in determining the performance and loss values of the motor was verified by comparing the results obtained from FE calculations with measurement data. By doing so we ensure that the FE model is properly configured regarding the mesh element, time steps, and solution criteria. As a result we can move forward with the future models making sure that the calculated values by the FE analysis represent the real case with good accuracy.

In addition to the electromagnetic design procedure explained in the previous paragraph, a thermal model of the motor is constructed, and by applying corrections to the model's geometric details and improving the accuracy of the model we were able to model the air flow dynamics of the motor by comparing measurement took place on the motor and the Fluid Flow FE model.

In order to achieve the desired goals explained earlier. A traction induction motor which is defined as Reference Test Motor is selected. Based on the measurements performed on the motor and visual inspections on the motor a FE model have been constructed in ANSYS Maxwell environment. Several tests were performed on the Reference Test Motor including, no-load test, locked rotor test and load test based on the methods mentioned in the IEC 60349-2 Standard. The results obtained from the FE model was compared with the test data to verify the model.

Table 2.33. *Reference Test Motor Summary of Performance Comparison of Test and FE*

	Test Results	*2D FE*	*Abs. Error %*
Voltage [V]	372	373	0.3
Current [A]	197.9	194.9	1.5
Torque [N.m]	648	649.8	0.3
Output Power [kW]	99.17	99.55	0.4
Indirect total power loss [kW]	10.06	9.015	11.6

Table 2.34. *Reference Test Motor Summary of Loss Comparison of Test and FE*

	Test Results	*2D FE*	*Abs. Error %*
Stator Copper Loss [kW]	4.26	4.27	0.2
Rotor Copper Loss [kW]	2.69	2.68	0.4
Core Loss [kW]	2.23	1.76	26.7

As it can be seen from the table the developed FE model matches the test results with good accuracy. However the area that needs to further be investigated is the core loss calculations which will be discussed later.

And considering the thermal model of the motor we were able to get the same air velocity and air flow at the intake of the FE model compared to the measurement data; and by doing this now we have created a reference thermal design for the motor design procedure. By using the data gathered in this study, in a new electromagnetic design, we can calculate the volumetric loss generated at each component and given a cooling capacity or an air flow rate, we can simply make an argument that the newly designed motor can be cooled properly with the given air flow rate and the given loss values. Also this will help us to save time and computational power by not using thermal/Fluid Flow analysis at each iteration of our electromagnetic design

CHAPTER 3

DESIGN OF A NEW INDUCTION MOTOR

3.1. Introduction

In the previous chapter, an investigation in which a traction motor's performance can be accurately predicted, is concluded. This is done via comparing simulation results, with tests on an available traction motor called reference test motor.

The findings in the previous chapter will be used here to design and manually optimize the traction motor with a desired target motor performance.

Motor designs are usually based on experience obtained from previously designed and manufactured motors. Since, the manufacturing process is important on the motor performance as the material characteristics are affected by this process. This causes errors in prediction of the motor losses, also in prediction of no-load current; hence prediction of efficiency and power factor, as well as the motor torque at a given speed.

3.1.1. Design and Simulation Criteria

As explained in the previous part, because of these reasons certain design criteria are established from the study in the previous chapter. These criteria are used in an initial design which leads to a final prototype to be manufactured. In the previous Chapter the conditions for accurate simulation of a given motor are also developed. These criteria has adopted here to make sure that the performance of the new design is accurately predicted. The criteria used for design and simulation are explained in the coming sections.

Finite Element Meshing:

For modelling the motor accurately, and to be able to calculate losses correctly, mesh elements should be properly configured. However a finer mesh does not always result in the model to be more accurate. It may as well increase the computational time.

In order to determine mesh sizing at various model parts, an initial adaptive meshing is used which is explained in Section 2.5.3. A series of simulations ran on a specific model, to investigate the mesh size on critical parts, such as the air gap, and the rotor bar. Based on experience, the results from the adaptive mesh, and several runs with different mesh sizes, a default mesh size is chosen for each component of the model.

In this study 3-different mesh size scenarios are tried out as given in Table 3.1. In this investigation airgap, rotor bar mesh sizes are altered as given in Table 3.1, but other mesh sizes are the same for the 3 cases considered. Table 3.1.also presents the average torque and solid loss predicted from these simulations. It can be observed that they all lead to the same result. Therefore, case A mesh sizes are used as this meshing consumes less computational time.

Table 3.1. *Effect of Mesh Sizes on the Results and Computational Time*

	Case A	Case B	Case C
Airgap Max Mesh Element Size	0.15 mm	0.1 mm	0.15 mm
Rotor Bar Max Mesh Element Size	2 mm	2 mm	1 mm
Air gap mesh number	73084	136378	73084
Rotor Bar mesh number	5115	5104	17077
Avg. Torque [Nm]	649.8	649.8	649.7
Avg. Solid loss [kW]	1.6059	1.6058	1.6079
Avg. core loss [kW]	1.7572	1.7580	1.7579
Computational time [min]	115	243	167

Solution Type, Time Steps, Solution Accuracy, and Stop Time :

ANSYS Maxwell software is used for the electromagnetic simulations of the model, and through all design variations, transient mode of solution is used. In defining the solution setup there are parameters that need to be configured.

Accuracy of results in a FE model is closely linked to the time step selected, solution accuracy defined, and a stop time. To ensure the electromagnetic solution has reached steady state mode of operation with good accuracy it is needed to set these values accordingly. As you reduce the time step the rate of change in the B-Magnetic field variation increases, it allows for higher $dB/_{dt}$ to be included in the model.

As you reduce the time step the model allows for higher rates of change to be simulated and as such there appear surges in the core loss results , and the accuracy drops. To prevent that the convergence criteria should be more refined and in result it will increase the simulation time further. As it can be seen from the figure at 25 microsecond the result does not vary however there are surges that are considered an erroneous. Therefore, a 50 microsecond time step is used in the simulations and the convergence criteria is kept as 10^{-7}.

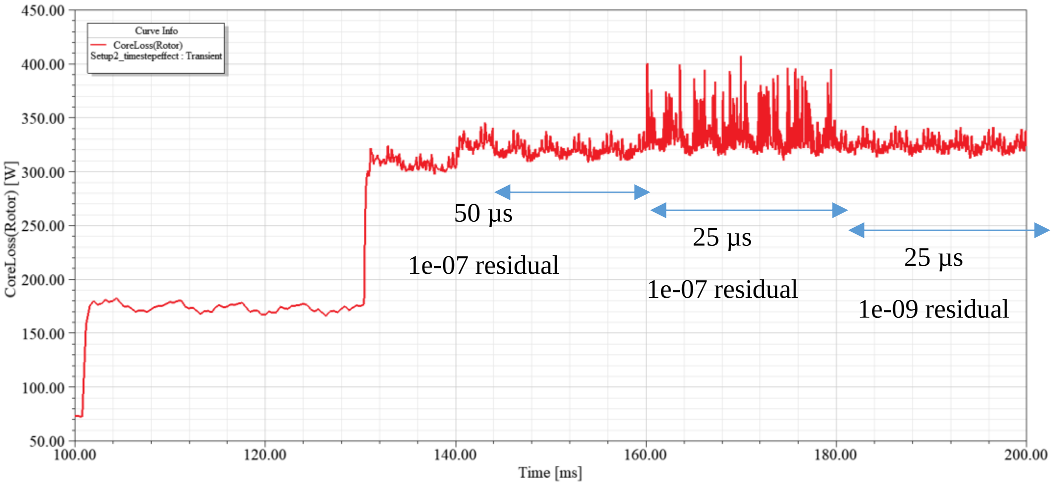

Figure 3.1. Effect of Time Step and Convergence Criteria on Transient Solution

These criteria identified from the study in Chapter 2 as summarized above is used in the simulation of the new design in the following studies.

3.1.2. Motor Material Selection

Core Material:

As it has been mentioned in 2nd Chapter, the same 50JN600 electrical steel is used in simulation models.

3.1.3. Electric and Magnetic Loading

The reference test motor FE model is verified in the 2nd Chapter, and to ease the designing process and to be able to compare the different traction motor and for benchmarking purposes the magnetic loading and the electric loading of the motor used in the traction application should be calculated.

Reference Test Motor Magnetic Loading:

$$\bar{B}_{gap} = \frac{P \times \varphi_{pole}}{\pi \times D_i \times l_{core}} \tag{3-1}$$

The magnetic loading is determined for the model using both analytical method and the FE analysis :

Table 3.2. *Reference Test Motor Magnetic Loading*

Reference Test Motor	*Analytical*	*FE*
Magnetic Loading (Air gap flux density)	0.61	0.64

Reference Test Motor Current Loading:

Current loading is defined as the total current being carried by the stator winding current per air gap periphery unit length, and as such we can calculate it based on the Equation (3-2).

$$q = \frac{3 \times 2 \times N_{ph} \times I_{ph}}{\pi \times D_i} \tag{3-2}$$

Q is the current loading, N_{ph} is the series turns per phase, I_{ph} is the rms current over stator winding phase, and D_i is the stator inner diameter. And for the Reference Test Motor with the given information of 42 series per phase, 194 Amps phase current, and 330 mm of stator inner diameter, the current loading is calculated to be 47.12 Ampere/mm.

Flux Density Constraints:

In the 2nd Chapter, section 2.5.5.2 Reference test motor is analyzed and its flux densities at critical cross section (stator back core, rotor back core, stator tooth, rotor tooth, magnetic loading) is calculated. Since the same material being used for the new design these limits are adopted in the newly designed motor.

Table 3.3. *Reference Test Motor's Magnetic Flux Density Critical Values at Full Load648Nm 100kW 50Hz, w.r.t Figure 2.13*

FEA Values	B value [T]
Stator-Teeth B limit @ S2	1.51
Rotor-Teeth B limit @ R2	1.6
Stator-Yoke B limit @ S1	1.63
Rotor-Yoke B limit @ R2.2	1.47

3.1.4. Thermal Considerations

An electromagnetic design is accompanied with thermal and fluid flow analysis to ensure the proper cooling of the motor, and to make sure that motor is within thermal limits determined by its insulation class.

By investigating the reference test motor, we concluded that a motor with a cooling structure of Figure 2.20 can dissipate 9313 Watt as included in Table 2.31 and retain temperature levels of Table 2.31. The initial design and further iterations of FEA simulation models have a similar cooling structure. As a result by knowing the air flow rate in a new design and amount of heat generated from each component, we can estimate the approximate value of the temperature to see whether it fall within our insulation class limits or not. In this approach we eliminate the need for a new thermal analysis.

3.1.5. Target Performance

In designing the new motor, the desired performance that needs to be met, is set based on the application requirements. The motor that is going to be designed and manufactured will be utilized in a traction application for a subway system. And the target performance is set based on a motor currently is use. This motor is manufactured by an Austrian company called “TSA- Traktionssysteme Austria, and its main characteristic are given in Table 3.4. Note that this motor has a frameless design.

The desired traction effort diagram of the motor (target performance) to be designed is given in Figure 3.2.

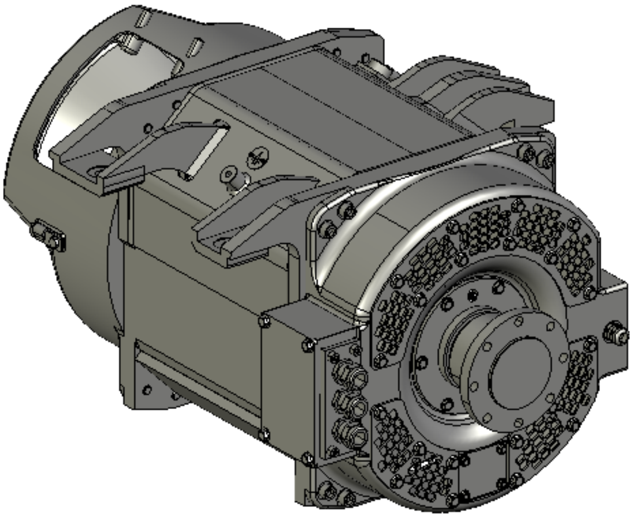

Figure 3.2. TSA Solid Model

Table 3.4. *Traktionssysteme Austria Traction Induction Motor Rated Performance under S1 Operating Condition*

Type of Travel	*M*
Voltage [L-L rms]	530
Connection	Y
Current [A rms]	184
Rated Speed [rpm]	2081
Torque [N.m]	574
f [Hz]	70
Output Power [kW]	125
Power Factor	0.78
Total losses [kW]	7.2
Stator Outer Diameter [mm]	380
Core Length [mm]	330
Motor Length [mm]	780

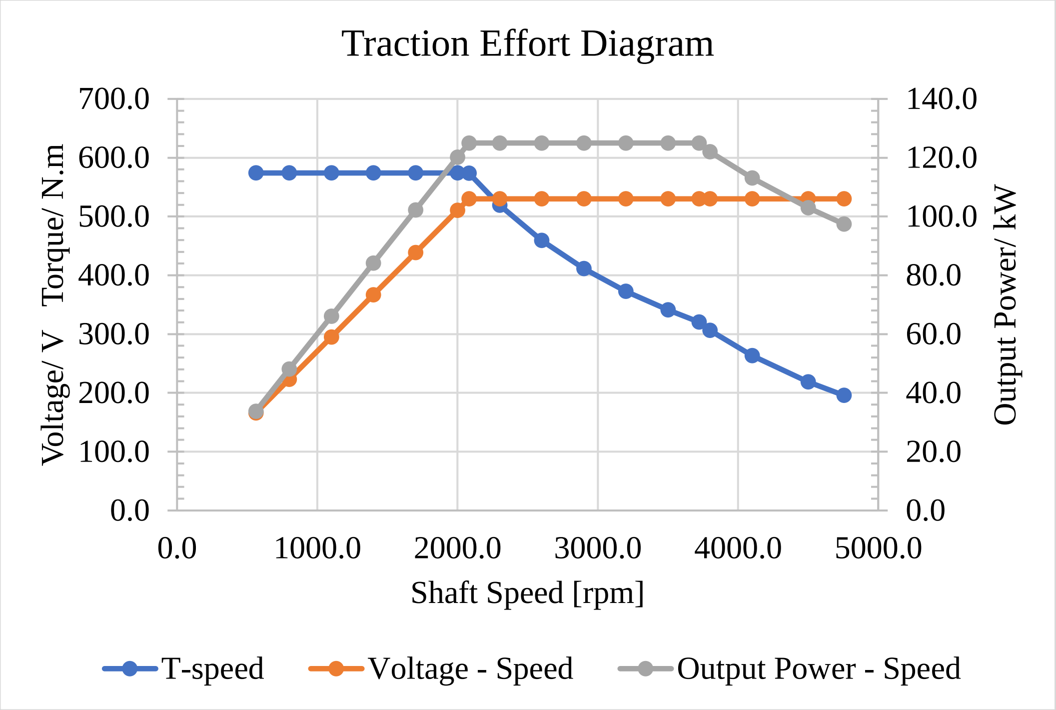

Figure 3.3. TSA Traction Effort Diagram

In designing the new motor, some constrains are in place regarding the bogie as in Figure 3.4 that limits the available space for the motor [Do max=450 mm, L core max=230].

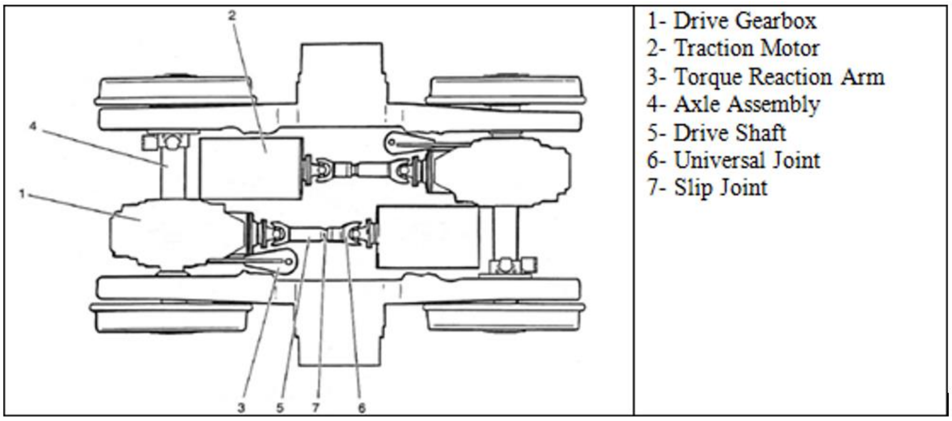

Figure 3.4. Bogie and its Designated Space for the Traction Motor

Cooling of this motor is achieved through an air flow into its air intake opening. The cooling system mounted on the bogie platform is able to push air into the motor with intake volumetric air flow of approximately 0.28 m^3/s.

Table 3.5. *TSA Cooling Capacity*

Motor	Intake Volumetric Air Flow Rate
TSA	0.28 [m^3/s]

3.2. Design Modification Method

In optimizing the design to our needs couple of options are available, first one is optimizing manually based on each iteration individually, second option is to use the ANSYS Maxwell optimization or Maxwell/MATLAB linked optimization, and the third option is to choose an analytical method for the optimization which is currently under development, and is out of the scope of this study. The method that is chosen in this chapter is to optimize the motor manually based on the result of each iteration, and the reason that this method is preferred over to the second one is because the second method does not give you the feeling of what happens at each iteration and you do not get to closely analyze each iteration. And rather in our method you closely monitor the stages of the design, regarding its electromagnetic design as well as its thermal and fluid flow analysis, and you can have more control over the system, with more flexibility on the design parameters. This chapter is dedicated to the iterative design procedure in order to achieve a design with the desire properties. As the results the design starts from an initial design and evolves into its final state.

3.2.1. Initial Design(Prototype-001)

An initial design is constructed. The design is based on the reference design parameters decided from the study of the "Reference Test Motor" discussed in Chapter 2. Additional constraints exist on the new motor, the outer diameter is limited to 420 mm and the core overall length is also limited to 779 mm. Therefore the core length cannot exceed 230 mm. The restriction on the core length comes from mechanical considerations. Furthermore the weight of the motor is restricted to 500 kg.

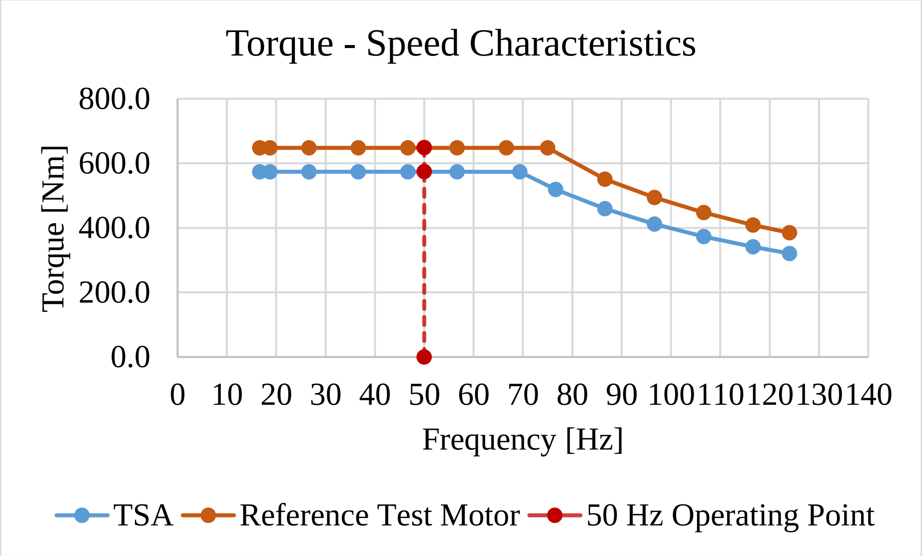

Figure 3.5. *Torque – Speed Characteristics Comparison*

According to target performance’s torque-speed characteristics plotted in Figure 3.6, the planned motor is required to provide 574 N.m torque in the constant torque operating region which in equivalent of providing 89-kW power at 50 Hz. However it has been decided to start the initial design with a margin of approximately of 12 %, the reason for considering this margin is the availability of the reference test motor and the higher validity of the FE results if compared with a similar motor. and with respect to the sizing equation given in (3-3) the motor is expected to provide 100-kW power at 50 Hz continuous operating mode.

$$S/n = G \times D_i^2 \times L \tag{3-3}$$

By keeping the coefficient G constant (the initial design main dimensions are selected based on the fact the it is capable of providing the same output as reference test motor and based on the design parameters B-(Magnetic Loading) and q-(Electric Loading) are set as of reference test motor) based on the sizing equation the new D and L is determined.

Table 3.6. *Design Parameters based on Reference Test Motor*

Ref. Mot.	G	B [T]	q [A/m]	Wire size mm	Fill factor	js	j bar	j er
FEA	4.97	0.64	47.12	8.5 × 1.5	48.35	7.6	5.48	6.76

3.2.2. Initial Design Main Dimension Determination

The reference test motor main dimensions are included in Table 3.7.

Table 3.7. *Reference Motor Main Dimensions*

Di	330 mm
Do	516 mm
L core	137 mm

Design constraints:

The initial design is a 4-pole machine and by keeping the stator outer diameter to inner diameter ration, and the fact that the outer diameter is selected as 420 mm. The core length can be calculated :

Table 3.8. *Reference Motor Parameters*

D_i^2L (constant)	14919300 mm^2
Di/Do (constant)	0.6395

$$D_{o,new} = 420\ mm$$

$$\frac{D_i}{D_o} = 0.6395 \ \rightarrow \ \boxed{D_{i,n} = 268.6\ mm}$$

$$D_i^{\ 2} \times L = 14919300\ mm^2 = \ (268.6)^2 \times l_{core,new} \ \rightarrow \boxed{l_{core,new} \ = 206.8\ mm}$$

Winding configuration :

The winding configuration is arranged in a way to keep the magnetic loading at an approximate value of 0.6 Tesla. The estimations are based on Equation (3-4).

$$e = \sqrt{2}\pi k_\omega N_{ph} f \varphi \qquad (3\text{-}4)$$

$$k_{dh} = \frac{\sin\left(h\frac{q\alpha}{2}\right)}{q * \sin\left(h\frac{\alpha}{2}\right)} \tag{3-5}$$

$$k_{ph} = \cos\left(\frac{h\gamma}{2}\right) \tag{3-6}$$

$$\alpha = \frac{2\pi \times \frac{p}{2}}{S_1} \tag{3-7}$$

The $k_\omega$is defined as the winding factor and considering the coil pitch has remained the same as to the reference motor, coil pitch is equal to 7 slot pitches. The skewing is not used in the design and manufacturing of the traction motor in this study, and so the winding factor consists of two main parts distribution factors displayed in Equation (3-5), and pitch factor written as Equation (3-6).

k_{dh} - distribution factor is linked to the slot pitch (α), defined in Equation (3-7), h which is defined as the harmonic order (h=1 being the fundamental), and q is defined as slots per pole per phase which in this case is 3. k_{ph} is defined as the pitch factor in which γ is the angle deficit of a coil pitch compare to a pole pitch, and p is the pole number of the motor.

So the winding factor in Equation (3-4) is calculated to be $k_\omega = 0.9$.

A constraint on Equation (3-4) is the Magnetic loading $\bar{B}$=0.6 (T). So to calculate the stator series turns per phase (N_{ph}) , flux per pole (φ) can be determined as shown in Equation (3-8).

$$\varphi = \bar{B}.A_{pole} \rightarrow \varphi = \frac{\bar{B} \times \pi \times D_i \times L_{core}}{p} \tag{3-8}$$

Selecting induced voltage “e” in Equation (3-4) as the input supply voltage, N_{ph} can be determined. Since all the parameters in Equation (3-4) in known.

Conductors’ dimensions:

The traction application requires a higher concentration of current in stator winding, so to increase the conductive cross section thus increasing the stator fill factor, rectangular shaped copper conductors has been utilized in this application. The conductor shape has been selected with respect to the available standard combination of width and thickness of the wire. Considering the manufacturing hurdles and to create a safety margin for the design a fill factor of 0.48 has been selected. , the effective area for the conductors is 258 mm^2. As a result the total area for the copper conductors is calculated to be 123.84 mm^2. There are total number of 6 conductors in the slot, copper area of each conductor is calculated to be 20.64. With respect to the available libraries in ANSYS RMxprt the width of the conductor has chosen to be 4.9 mm and the thickness of an individual conductor has chosen to be 4.12 mm. Resulting in a fill factor of 0.47. The results are posted in Table 3.9.

Table 3.9. *Prototype-001 Winding Configurations’ Summary*

	Turns /ph.	Conductor /slot	Parallel branch	Winding layer	Coil pitch(slot)	Pole pitch(slot)	Fill Factor
Reference Test Motor	42	14	2	2	7	9	48.35
Prototype-001v1	36	6	1	2	7	9	47.0

Slot geometry:

The new motor has an inner diameter of D_i=268.6 mm. As compared to Reference Test Motor with D_i=330 mm. The slot geometries have been scaled down with the factor of $\frac{D_{i,new}}{D_{i,Refernce\ Test\ Motor}} = 0.814$.

Stator slot specifications:

Table 3.10. *Prototype-001 Stator Slot Specifications*

	Reference Test Motor	Prototype-001v1
Hs0 [mm]	2.40	1.95
Hs1 [mm]	2.00	1.63
Hs2 [mm]	35.8	29.14
Bs1 [mm]	13.0	10.58
Bs2 [mm]	10.4	8.46
Total slot area	414.34	276.81
Effective Slot Area [mm^2]	372.32	246.52
Slot No	36	36

Rotor slot specifications:

Table 3.11. *Prototype-001 Rotor Slot Specifications*

Name	Reference Test Motor	Prototype-001v1
Hs0 [mm]	4.6	3.74
Hs01 [mm]	0.0	0.0
Hs1 [mm]	0.4	0.28
Hs2 [mm]	21.6	17.58
Bs0 [mm]	3.3	2.68
Bs1 [mm]	8.1	6.59
Bs2 [mm]	5.1	4.15
Rs [mm]	0.5	0.41
Total slot area [mm^2]	163.35	107.68
Effective Slot Area [mm^2]	148.17	97.66
Slot pitch	22.37	18.18
Slot No	46	46

For better cooling we shall introduce ducts to outer rim of the stator lamination, later we shall study how this stator ducts will affect the cooling of the motor. It is expected that altering the stator back core to house these ducts will change the flux densities and the design has to be revised to return magnetic loading, electric loading, and flux densities to designated levels.

3.3. Prototype-002

3.3.1. Introduction

In this section an initial stator ducts of 1 cm width will be placed on the stator outer rim to assist the cooling, additionally a frame will be added to the design. The frame added will be analyzed with two options of a mild steel and cast-iron characteristics, to see which material is more suited for this operation considering the design and manufacturing challenges in the process. The schematic is shown in Figure 3.6.

Based on the resistance comparison of the Prototype-002v1 with the reference motor, as in Table 3.16 the rotor and stator slots should be modified to further reduce the resistance without sacrificing the magnetic flux density in the motor.

3.3.2. Main Dimensions

The main dimension of the design has not changed compared to the previous design(001v1). The model is analyzed to investigate the inclusion of frame and stator cooling ducts.

Table 3.12. *Prototype-002v1 Main Dimensions*

Stator inner diameter [mm]	270
Stator outer diameter [mm]	420
Rotor outer diameter [mm]	267.6
Rotor inner diameter [mm]	100
Core length [mm]	205

3.3.3. Body Frame and Cooling Ducts

A mild-steel frame is placed in the FE model to house the stator laminations. The details are in Table 3.13.

Table 3.13. *Prototype-002v1 Frame Geometric Specifications*

Frame Inner diameter [mm]	420
Frame Outer diameter [mm]	440
Frame Axial length [mm]	205

The cooling ducts on the outer rim of stator is also included in the FE design with details shared in Table 3.14.

Table 3.14. *Prototype-002v1 Stator Cooling Vents' Geometric Specifications*

Single Channel span [degree]	15
Vents' Inner radius [mm]	200
Vents' Outer radius [mm]	210
Radial thickness [mm]	10
Axial length [mm]	205
#No	12

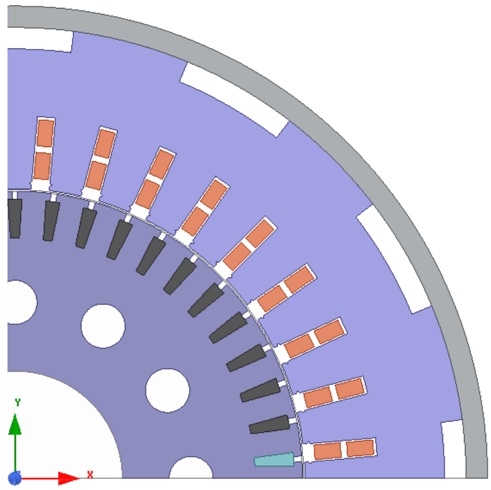

Figure 3.6. Prototype-002 Stator Cooling Vents and Motor Frame

3.3.4. Results

In this section FE results are provided for prototype-002v1 and its B and q values are calculated and compared with the reference test motor. A thermal analysis is performed with the determined loss values and based on the comparison results; several improvements are applied.

Operating conditions :

Table 3.15 *Simulation Operating Conditions*

	Maxwell 2D/RMxprt
Stator operating temperature[°C]	127
Rotor operating temperature[°C]	127
Voltage[V], (L-L), rms	360
Frequency[Hz]	50
Output Power[kW]	100
F [Hz]	50

3.3.4.1. Resistance Comparison

In Table 3.16 resistance values are calculated and compared with the reference test motor values. Calculating the resistance is a preliminary measure to determine stator, and rotor copper loss, assuming the same current levels.

Table 3.16. *Prototype-002v1 and Reference Test Motor Stator and Rotor Resistive Characteristics*

	Reference Test Motor	Design-002v1
Stator slot copper area [mm^2]	178.5	121.13
Stator Conductor per phase per slot area [mm^2]	25.5	20.188
Stator phase resistance @ 20˚C [ohm]	0.024	0.028
Stator phase resistance 127 [ohm]	0.03477	0.03974
Rotor slot copper area [mm^2]	148.16	97.65

3.3.4.2. Loss Components: [T rated = 650 Nm, f=50 Hz, V=360 Volt]

The calculated FE losses are included in Table 3.17. These values will be used for thermal analysis in Section 3.3.5.

Table 3.17. *Prototype-002v1 Full load loss component*

2F FEA	*Simulation Model*	
	Refence Test Motor	*Design-002v1*
P_{input} (kW)	107.5	109.3
slip	0.026	0.027
$P_{cu,\,s}$ (kW)	4.0	4.73
Pf_e (kW)	2.33	2.23
$P_{cu,\,r}$ (kW)	2.5	2.76
$P_{cu,r,\,bar}$	1.18	1.92
$P_{er,\,rotor}$ (kW)	1.3	0.84
P_{loss} (kW)	9.63	10.5

As it is seen from the Table 3.17 the stator and rotor copper loss values in the current design iteration are considerably higher than the reference test motor , with $P_{cu,s}$ 18 % and $P_{cu,r,bar}$ (rotor bar copper loss) 62 % higher . In order to lower the copper losses next iteration will be focused on increasing the copper cross section to reduce the copper loss.

3.3.4.3. Rotor Bar and End Ring Electrical Properties

In 2D FE analysis rotor bars are included in the model, and the calculation procedure is the same as mentioned in Section 2.5.5.1. The results are included in Table 3.18 .

Table 3.18. Design-002v1 rotor bar copper loss calculation

Analytical Calculations	Reference Test Motor	Design-002v1
Rotor Bar Current [A]	849.7	742.0
Rotor End ring Current [A]	3110.2	2716.0
Rotor End ring resistive loss @127 ˚C [W]	1304.6	839.0
ρ (resistivity) [Ohm.m]	2.35e-08	2.5e-08
Rotor End ring cross section [mm^2]	314	314
πD_m (end ring equivalent length) [mm]	901	714
Rotor Bar conductor area [mm^2]	148.17	97.66
Rotor Bar Current Density (A/mm^2):	5.7	7.6
Rotor Ring Current Density (A/mm^2):	10.54	8.6
Stator series turns per phase	42	36

As it can be seen from the Table 3.18 rotor bar current density in the current design stage 002v1 is 33 % higher compared to the reference test motor, although the bar current is lower. This issue will be addresses in the next design iteration- 002v2 by increasing the rotor bar cross section.

Stator Current Density and Electric Loading :

Electric loading and current density of the new design is included at Table 3.19 .

Table 3.19. *Stator Current Density and Electric Loading*

FEA 2D Results	Reference Test Motor	Design-002v1
Stator Current Density [A/mm^2]	7.7	9.88
Specific Electric Loading [A/mm]	47.8	50.8
Stator winding fill factor	0.48	0.47

3.3.4.4. Magnetic Flux Density at Critical Cross Sections

The material that is used in the FE model for the design-002v1 is the same as the material used for simulating the Reference Test Motor. So in order to keep the core loss under control and utilize the electrical steel laminations more effectively without saturating them, flux densities in FE environment is calculated and included in Table 3.20. The detail on how these flus densities is calculated is included in Section 2.5.5.2.

Table 3.20. *Prototype-002v1,v2, and Ref. Motor Magnetic Flux Density Comparison*

	Reference Test Motor	Prototype 002v1
	B avg	
Stator-Teeth Flux Density (T)	0.928	0.86
Stator-Yoke Wide (T)	1.03	0.89
Stator-Yoke Narrow (T)		1.03
Rotor-Teeth Flux Density (T)	1.11	1.02
Rotor-Yoke Flux Density (T)	0.92	0.89
Air-Gap Flux Density (T)	0.66	0.62
Flux per pole[Wb]	0.0237	0.027
Pole area[mm2]	35507	43471

It can be seen that the flux density at all cross sections fall below the reference test motor values and there is room to increase the electrical cross section.

3.3.5. Thermal, and Fluid Flow Analysis

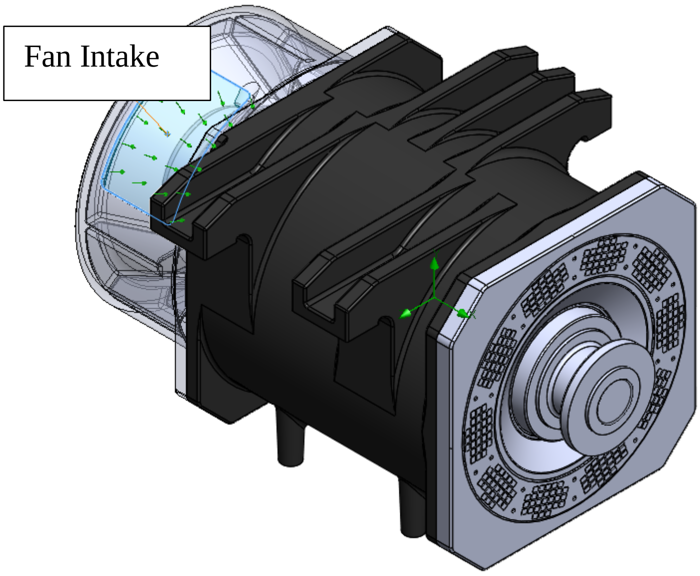

Figure 3.7. Motor's Geometry

At this stage of the design, the electromagnetic analysis is concluded, on Prototype design-002v1. Taking the loss components calculated earlier from FE analysis results given in Table 3.17 as uniformly distributed volumetric heat sources. A thermal analysis is performed on the model.

Table 3.21. *Heat Generation in Parts of the Prototype-002v1, Based on Simulation Results-50 Hz, 650 Rated Torque*

Motor Part	*Type of Loss*	*Loss [W]*	*Volume [dm^3]*	*Loss Value [w/dm^3]*
Stator	Stator Core Loss	1543	15.13	102
Stator Winding	Stator Copper Loss	4730	1.94	2438.1
Rotor	Rotor Core Loss	485	8.35	58.1
Rotor Cage	Rotor Copper Loss	2760	2.45	1126.5
Frame	Frame Core Loss	206.4	3.1	66.6

Stator cooling ducts are selected as 1 cm in radial direction as seen in Figure 3.8.

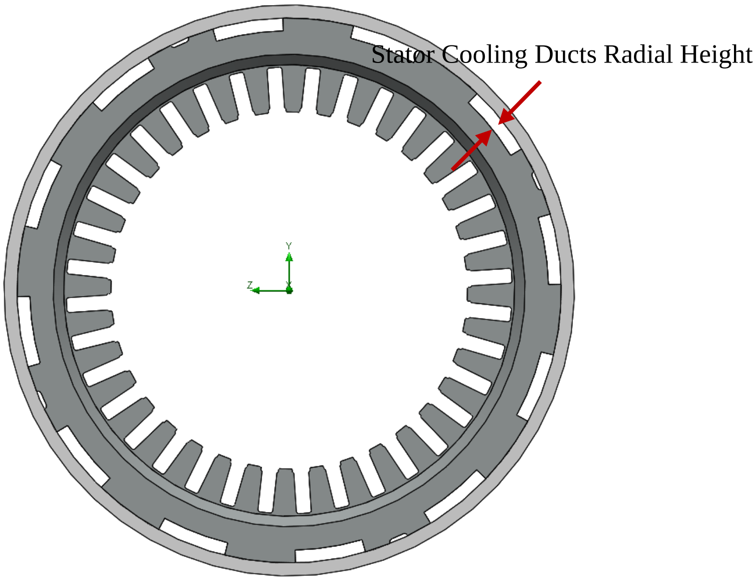

Figure 3.8. Prototype-002v1- FE model Motor’s Stator Cooling Channels-1 cm in Radial Direction

And the geometry is given in Figure 3.7 with air intake shown, here in this geometry the air is pushed into the intake by means of an external source, and as stated in Table 3.22 the air flow rate at the intake is 0.242 m^3/s which is translated to 0.3 Kg/s.

As the loss values are given in Table 3.21 and since the Fan characteristics is known and the air flow rate is determined as 0.242 m3/s. So the temperature of the motor parts can be calculated, and the results are shown in Table 3.22

Table 3.22. *Steady state Temperature of various parts of Design-002v1- as A Fluid Flow-Thermal Analysis in a Simulation Environment*

Components	*Minimum Temp. [˚C]*	*Maximum Temp. [˚C]*	*Average Temp. [˚C]*	*Pressure Drop [Pa]*	*Intake Air Flow Rate [m^3/s]*	*Loss kW*	*Measured avg. Temperature Ref motor*
Stator Winding	86.9	179.1	143.3	804.2	0.24	4730	163
Stator Core	51.6	122.3	103.5			1543	163
Rotor Core	88.5	135.2	121.8			485	120
Rotor Cage	121.7	149.3	140.6			2760	120
Frame	65.7	110.4	93.0			206	-

Table 3.22 proves the assumption made at Table 3.15 on the stator winding and the rotor cage to be approximately at the same temperature. Additionally the thermal analysis produces close results to initial temperature assumptions at Table 3.22. So no further electromagnetic- thermal iteration is required.

In conclusion of the -prototype-002v1- stator air ducts are housed at the rim of the stator laminations, and a frame is included in the design model. Magnetic properties(magnetic loading, and flux densities at critical cross sections of the design) of the design as well as its electrical characteristics(electric loading, electric current density) are analyzed. Its loss components are determined. By comparing the aforementioned data with the reference test motor as included in Table 3.17, and Table 3.20 it is obvious that the motor is under stress because of the higher heat generation in rotor bars, and stator windings. In the next iteration- prototype-002v2- a modification will be applied to increase the copper cross sections both on the stator windings and the rotor bars, while keeping magnetic flux density value at determined limits.

3.3.6. Prototype-002v2

By calculating the B-magnetic loading-, q-electric loading-, and windings' resistance c from the prototype-002v1 design iteration, and comparing it to the reference test motor values, stator and rotor slots are going to be modified. Mild Steel is selected as the frame material at this variation (Prototype-002v2).

3.3.6.1. Stator Slot Modifications

As it can be seen in Table 3.29 the resistance of the newly developed model of Prototype-002v1 exceeds the reference test motor and since we take the thermal analysis safety margin based on the reference motor, it is desirable for us to limit the loss components to the reference motor to be sure of its proper heat dissipation.

Based on Table 3.33 the stator back core flux density at the narrow section (where vent is placed) is at its limit.(prtotype-002v1=1.03 Tesla, compared to Reference Test Motor =1.03 Tesla) However, the stator tooth flux density is 0.86 Tesla, compared to Reference Test Motor at 0.93 Tesla. The modification will be centered around changing the stator slot width.

Table 3.23. *Stator Average Tooth Flux Density Comparison Ref. Motor and Prototype-002v2 before Modification*

	Reference Motor	Prototype-002v2
Stator Average Tooth Flux Density- $\bar{B}_{ts}$	0.93	0.86

$$\varphi = \bar{B}.A_{pole} \rightarrow \varphi = \frac{\bar{B} \times \pi \times D_i \times L_{core}}{p} \tag{3-9}$$

$$Mean\ tooth\ flux\ \bar{B}_{ts} = \frac{\varphi_{pole}}{\#teeth\ per\ pole\ \times tooth\ width@\frac{1}{3} \times core\ length} \tag{3-10}$$

Flux per pole is calculated using Equation (3-5) φ_{pole}= 0.027wb, and the number of stator teeth per each pole is 9, additionally the tooth width at one-third from the narrow end ($tooth\ width@\frac{1}{3}$) is found to be 17 mm. The core length is given in Table 3.14 as 205mm. Assuming flux per pole is constant , and, we keep the core length and teeth per pole constant. We want to determine the tooth width in the modified state which yields the desired flux density.

$$\bar{B}_{ts}[old] \times tooth\ width@\frac{1}{3}[old] = \bar{B}_{ts}[desired] \times tooth\ width@\frac{1}{3}[new]$$

$$\begin{cases} \bar{B}_{ts}[old] = 0.86\ (T) \\ \quad tooth\ width \\ \frac{1}{3}[old] = 17.0\ (mm) \\ \bar{B}_{ts}[desired] = 0.93\ (T) \end{cases} \rightarrow\ tooth\ width@\frac{1}{3}[new] = 15.7$$

The slot is parallel sided , so to find the new slot width after modification we calculate the slot pitch at 1/3 diameter and determine the slot width.

$$D\left[@\frac{1}{3}\right] = 292.08\ (mm)\ stator\ slot\ width = (\pi \times D) - tooth\ width$$
$$= 9.78 (mm)$$

$$\boxed{\rightarrow Stator\ slot\ width\ [Modified] = 9.78\ (mm)}$$

Table 3.24. *Prototypt-002v2 Comparing Stator Slot Width Before and After the Modification*

Stator slot width [Before modification]	8.46 mm
Stator slot width [after modification]	9.78 mm

Stator conductor dimensions:

$$\frac{new\ conductor\ width}{old\ conductor\ width} = \frac{new\ slot\ width}{old\ stator\ width} \tag{3-11}$$

Since the stator slot width have been modified by using (3-11) the new conductor width is calculated to be 5.66 mm, however due to conductor sizing standards, the closest conductor size has been selected as 5.5 mm. The new conductor size logged into Table 3.25.

Table 3.25. *Prototype-002v2 Stator Conductors' Dimensions Before and After the Modification*

	Before modification	After modification
Stator conductor dimension	4.9 mm × 4.12 mm	5.5 mm × 4.12 mm
Fill Factor	46.9	45.6

3.3.6.2. Rotor Slot Modifications

The purpose in rotor slot modification is to increase the conductor area and thus reduce the resistivity and current density on the rotor bars.

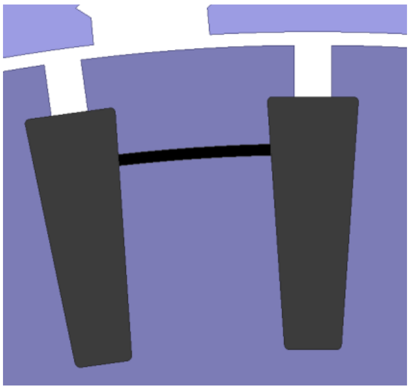

Figure 3.9. The One-Third Rotor Tooth Cross Section

The rotor slot is being modified in two directions, rotor slot width and the rotor slot height. The rotor teeth are approximately parallel to each other. The rotor shape is included in Figure 2.3 The Schematics of the rotor bar shape given is a typical format to represent the cross sections and does not represent the final shape.

Constraint limiting the rotor slot width (Bs1, and Bs2 refer to Figure 2.3), is the rotor average tooth flux density which is limited to the value of the verified reference motor value. The new rotor tooth width is going to be selected in a way that the average flux density at 1/3 of the rotor tooth (shown in Figure 3.9) is increased to its maximum allowed value which is determined by the reference motor.

Table 3.26. *Prototype-002v2 Rotor Tooth Width Before Modification*

Parameter	*Value*
φ_{pole} [Wb]	0.027
Teeth per pole	46/4
Tooth width at one-third height [mm]	11.15
Core length [mm]	205
Rotor mean tooth flux density [T]	1.02

Based on the values provided at Table 3.26 rotor mean tooth flux density can be calculated before changing the rotor slot geometry.

Assuming flux per pole is constant, and, we keep the core length and teeth per pole constant. We want to determine the tooth width in the modified state which yields the desired flux density.

$$\frac{\bar{B}_{tr}[old]}{\bar{B}_{tr}[desired]} = \frac{tooth\ width@\frac{1}{3}[new]}{tooth\ width@\frac{1}{3}[old]} \tag{3-12}$$

The desired value of B_{tr} as included at Table 3.33 is 1.11 Tesla, compared to its current state at prototype-002v1 is 1.02 T. So, there is approximately a 9% margin in which we can decrease the slot width.

Based on Equation (3-12) it is simple to calculate the new tooth width at diameter of 252 mm. It is calculated to be 10.24 mm which can be shown in Table 3.27.

Table 3.27. *Prototype-002v1&v2 Rotor Tooth Width After Modification*

Parameter	Value
Rotor Mean Tooth Flux Density before Modification [T] (Prototype-002v1)	1.02
Rotor mean Tooth Flux Density Desired [T] (Prototype-002v1)	1.11
Tooth Width $\frac{1}{3}$ before Modification [mm]] (Prototype-002v1)	11.15
Tooth Width $\frac{1}{3}$ After Modification [mm]	10.24
Diameter of Motor at One-third rotor tooth cross section [mm]	252

$$rotor\ slot\ width\ @\frac{1}{3} = (\pi \times D) - tooth\ width@\frac{1}{3} = 6.97(mm)$$

$$\begin{cases} rotor\ slot\ width \\ \frac{1}{3}\ [old] = 6.06\ mm \\ rotor\ slot\ width \\ \frac{1}{3}\ [new] = 6.97\ mm \end{cases} \rightarrow \boxed{increase\ in\ slot\ width = 0.9\ mm}$$

$$\begin{cases} Bs1[new] = \ Bs1[old] + 0.9 = 7.48\ mm \\ Bs1[new] = \ Bs1[old] + 0.9 = 5.04\ mm \end{cases}$$

Rotor bar conductor area = 110.05 mm^2

Rotor slot height modification:

In this section, after the rotor slot width dimensions have been selected(according to the mean flux density in rotor tooth.) we are going to modify the rotor slot height in a way that the current density of the rotor bar matches the current density of the Reference Test Motor.

We are trying to optimize the rotor height based on decreasing the current density from 7.6 A/mm^2 to 6 A/mm^2:

$$desired\ bar\ conductor\ area\ = \frac{Rotor\ bar\ current}{desired\ current\ density} = 123.6\ mm^2$$

$$Rotor\ bar\ conductor\ area\ = \frac{(Bs1 + Bs2)}{2} \times Hs2$$

$$\begin{cases} Desired\ rotor\ bar\ conductor\ area = 120\ mm2 \\ Bs1 = 7.48\ mm \\ Bs2 = 5.04\ mm \end{cases}$$

$$\rightarrow \boxed{Hs2\ [modified] = 19.17\ mm}$$

The Modified rotor slot is included in Table 3.28.

Table 3.28. *Prototype-002v2 Rotor Slot Geometric Modified Result*

Name	Reference Test Motor	Design-002v1	Design-002v2 [Modified]
Hs2 [mm]	21.6	17.58	19.17
Bs1 [mm]	8.1	6.59	7.48
Bs2 [mm]	5.1	4.15	5.04
Total slot area [mm^2]	163.35	107.67	134.1
Effective Slot Area [mm^2]	148.17	97.65	124.0

3.3.6.3. Resistance Comparison due to Modified Dimensions

Table 3.29. *Prototype-002v1,v2 and Reference Motor Resistance Comparison*

	RTM	Prototype002v1 [default]	Prototype 002v2 [Modified]
Stator slot copper area [mm^2]	178.5	121.1	135.9
Stator Conductor per phase per slot area [mm^2]	25.5	20.188	22.7
Stator phase resistance 20˚C [ohm]	0.024	0.028	0.0248
Rotor slot copper area [mm^2]	148.2	97.6	124.0

However by increasing the electric conductive area we are increasing the magnetic flux density but regarding the reference point we do not violate the limits as shown in Table 3.33. By making the modifications we are able to decrease the loss values, and thus reduce the heat generation in stator and the rotor windings.

Loss Components (T rated = 650 Nm, f=50 Hz, V=360 Volt):

Table 3.30. *Loss Components- Optimized Stator and Rotor Slots at Prototype-002v2*

	FEM 2D		
	Reference Test Motor	Prototype 002v1[default]	Prototype 002v2 [Optimized]
P_{input} [kW]	107.5	109.3	107.1
$P_{cu, s}$ [kW]	4.0	4.73	4.2
P_{fe} [kW] Frame Inc.	2.33	2.23	2.3
$P_{cu, r}$ [kW]	2.5	2.76	2.54
$P_{cu, r, bar}$ [kW]	1.18	1.92	1.7
$P_{er, rotor}$ [kW]	1.3	0.84	0.84
P_{tot} [kW]	9.63	10.55	9.92

It is seen that by making the modifications, we managed to decrease the rotor bar copper loss by 11 % and stator copper loss by 11%

Table 3.31. *Rotor Cage Current Ratings- Optimized Stator and Rotor Slots at Prototype-002v2*

2D FEA	Reference Test Motor	Prototype 002v2 [Optimized]	Prototype 002v1[default]
Bar Current [A]	849.7	741.2	742.0
End ring Current [A]	3110.2	2713.2	2716.0
Rotor Bar Current Density (A/mm^2)	5.7	6.0	7.6
Rotor Ring Current Density (A/mm^2)	10.54	8.6	8.6

Considering the Table 3.31, it is shown that by making the modifications the rotor bar current density is 21 % lowered.

Stator Current Density and Electric Loading :

In calculating the current density in FEA, since the conductors all are connected in series and the area of each conductor is defined, stator current density can be determined, the results are summarized in the Table 3.32.

Table 3.32. *Stator Current Ratings-Optimized Stator & Rotor slots at Prototype-002v2*

FEA 2D	Reference Test Motor	Prototype 002v1[default]	Prototype 002v2 [Optimized]
Stator Current Density (A/mm^2):	7.7	9.88	8.8
Specific Electric Loading (A/mm):	47.8	50.8	50.7
Stator winding fill factor [%]	48.0	47.0	45.57

3.3.6.4. Magnetic Flux Density Results due to Modified Slot Dimensions

By modifications made in sections 3.3.6.1 and 3.3.6.2 the rotor slots and stator slots have been increased in dimensions so that rotor bar copper loss can be decreased, and the stator winding copper loss be decreased. However in doing so the magnetic flux density will be increased and based on the calculations , the modifications are intended to keep the B values at limits set by the reference value. The results of the B field changes before and after the modifications is posted in Table 3.33.

Table 3.33. *Prototype-002v1,v2, and Ref. Motor Magnetic Flux Density Comparison*

	RTM	Prototype 002v1[default]	Prototype 002v2 [Optimized]
	B avg		
Stator-Teeth Flux Density (T)	0.928	0.86	0.95
Stator-Yoke Wide (T)	1.03	0.89	0.89
Stator-Yoke Narrow (T)		1.03	1.04
Rotor-Teeth Flux Density (T)	1.11	1.02	1.11
Rotor-Yoke Flux Density (T)	0.92	0.89	0.97
Air-Gap Flux Density (T)	0.66	0.62	0.63
Flux per pole[Wb]	0.0237	0.027	0.0276
Pole area[mm2]	35507	43471	43471

3.3.7. Prototype-002v3

This version of the design is a variant of the design prototype-002v2, the mild steel frame is being replaced by the cast iron frame in prototype-002v3. The mild steel has higher permeability than the cast iron and acts as part of the stator core . It is helping in reducing the flux density in the stator back core. However, to investigate the limitations the material, the frame has chosen to be cast iron. Since cast iron has higher reluctance compared to the mild steel, the flux density at motor parts will increase, to compensate in next iteration, core length will be modified.

3.4. Prototype-003

3.4.1. Prototype-003v1

With respect to the previous section named Prototype-002v3 and Prototype-002v2 , the magnetic flux densities in various cross sections of the motor, it is noticed that by using cast iron as the motor frame the flux density in the back core of the stator increases and need to be compensated. For this purpose, to reduce the flux density in the back core of the stator it has been decided to increase the core length.

Table 3.34. *Constraint on Stator Back Core Flux Density of Prototype-002v3 Compared to Ref. Design*

	Reference Design	Prorotype-002v3
Average Stator Yoke Flux Density (T)	1.03	1.13

New core length is calculated to reduce the flux density by increasing core length approximately 9.2% . The final results are posted in Table 3.35.

$$New\ core\ length = \frac{1.13}{1.03} \times 205\ mm = 223.9\ mm$$

$$Selected\ core\ length = 225\ mm$$

Table 3.35. *Magnetic Properties Comparison, Reference Motor and Prototype-002v3 and Prototype-003v1*

	RTM	Prototype 002v3	Prototype 003v1
	B avg	B avg	B avg
Stator-Teeth Flux Density (T)	0.928	0.97	0.87
Stator-Yoke Wide (T)	1.03	0.96	0.9
Stator-Yoke Narrow (T)		1.13	1.06
Rotor-Teeth Flux Density (T)	1.11	1.16	1.04
Rotor-Yoke Flux Density (T)	0.92	1.04	0.93
		1.02	0.93
		0.92	0.83
Pole area[mm^2]	35507	43471	43471

3.5. Prototype-004

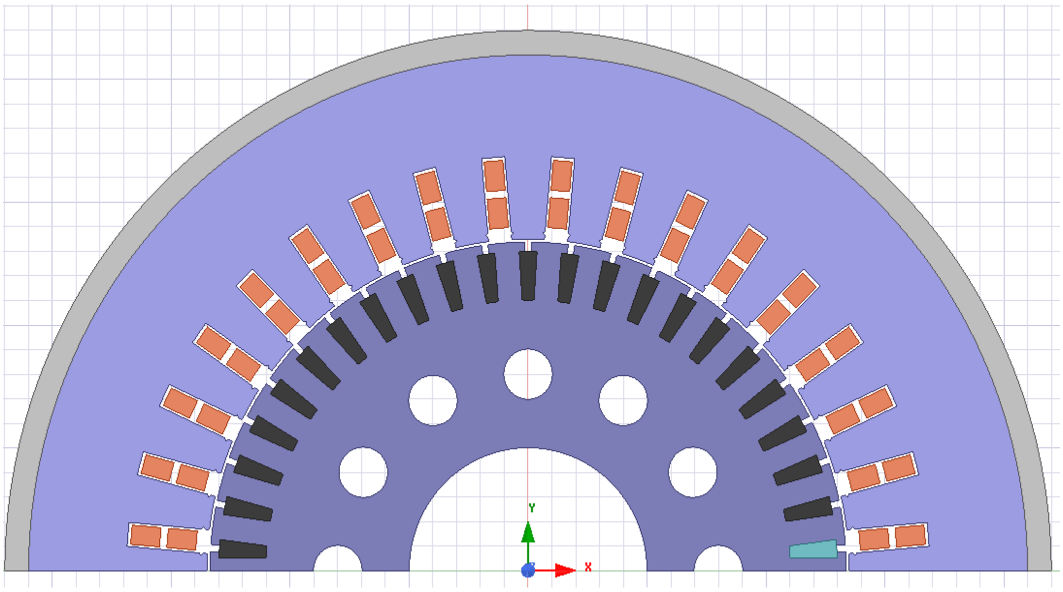

Figure 3.10. Prototype-004 FE 2D Geometric Cross Sections Across Variants

The incentive for this design variation is the rotor copper loss, specifically rotor bar copper loss. Based on the previous simulations the rotor copper loss in the rotor bars is considerably higher compared to the reference design. This much heat generation in rotor bars is endangering the integrity of the rotor cage. The cooling system would be unidirectional meaning, a fan will below air from one side and hot air will come out from the other side. And there is going to be a temperature difference between the two ends of the rotor bars. More importantly based on the fluid analyses the more heat exchange/ heating & cooling will result in frequent elongations and contractions of the rotor bars which in turn will increase the chance of the joint between the rotor bars and the end ring to decouple, resulting in a faulty motor. As such we need to reduce the heat generated in the rotor bars. This design variant is focused on analyzing the effect of the winding configurations on the loss generation in rotor bars. The stator winding configuration is going to be selected in an increasing trend, so the stator vents have been closed to release the pressure from the core, magnetic-wise.

3.5.1. Prototype-004 Variants

The main geometric dimensions remain constant throughout the variant, which is included in Table 3.36 and shown in Figure 3.10. However, the winding configurations will be varied according to Table 3.37.

Table 3.36. *Prototype-004 Main Dimensions Across All Variants*

Inner diameter [mm]	420
Outer diameter [mm]	440
Axial length [mm]	205

The variants are briefly summarized in Table 3.37.

Table 3.37. *Prototype-004 Variations'-Summarized*

	Reference Test Motor	Prototype 003v1	Prototype-004v1	Prototype-004v2	Prototype-004v3
Stator slot copper area [mm^2]	178.5	135.96	135.95	142.43	139.06
Stator Conductor per phase per slot area [mm^2]	25.5	22.66	22.66	28.49	25.28
Stator phase resistance @ 20˚C [ohm]	0.024	0.026	0.026	0.017	0.021
Rotor slot copper area [mm^2]	148.16	124.0			
Winding	2// 7+7	Series 3+3	Series 3+3	2// 5+5	4// 11+11
Series turns per phase	36	36	36	30	33
Fill factor	48.34	45.57	45.57	47.75	46.62

In order to affect the rotor bar current it has been decided to change the series turns per phase to alter the rotor bar current while trying to balance out the magnetic flux density in the machine. The main idea behind this change is related to rotor bar current equation listed here :

$$i_{bar} = \frac{2 \times N_s \times k_{ws} \times m_s}{Q_2} \times i'_2$$

In which N_s is the series turns per phase and the k_{ws} is the winding factor, and Q_2 is the number of rotor bars, and finally m_s is the number of phased here in this motor of 3 phases. Since the geometry is assumed to be fixed, and the number of rotor and stator bars have been decided another parameter that can affect the bar current based on the above equation is the series turns per phase. However as it is known based on the trivial equation of induced voltage which is mentioned here in equation below, as we decrease the N to lower the rotor bar copper loss, the flux density will increase accordingly so there should be a balance between the current and the flux. Additionally for the same reason the stator cooling vents have been closed so just to consider the effect of the winding configuration on bar copper loss, ignoring the flux density problem at this stage of the design.

Three different winding configurations have been tested here , 3+3 all turns in series (36 N_{ph}), 5+5 with 2 parallel paths (30 N_{ph}), and 11+11 with 4 parallel paths (33 N_{ph}). The results are posted in Table 3.38

3.5.2. Prototype-004 Variations' Comparison Data on Critical Design Points

Table 3.38. *Prototype-004 Magnetic and Electrical Properties Comparison Through Variants*

2D FEA	Reference Test Motor	Prototype 003v1 L=225 cast	Prototype-004v1 [cast iron],[L=225],[stator vents removed]	Prototype-004v2	Prototype-004v3
Bar Current [A]	849.7	743.9	743.0	620.4	676.9
Solid Loss (FEM)[kW]	1.18	1.73	1.72	1.54	1.57
Rotor Bar J (A/mm^2):	5.7	6.0	6.0	5.0	5.45
N ph	42	36	36	30	33
	B peak				
Stator-Teeth Flux Density (T)	1.46	1.36	1.36	1.65	1.51
Stator-BC Wide (T)	1.62	1.42	1.42	1.61	1.49
Stator-BC Narrow (T)		1.67			
Rotor-Teeth Flux Density (T)	1.74	1.63	1.63	2.0	1.82
Rotor-Yoke Flux Density (T)	1.44	1.47	1.48	1.77	1.64
		1.47	1.47	1.76	1.63
		1.3	1.3	1.56	1.44

As it can be seen from Table 3.38 by decreasing the Nph, so does the rotor bar current and the rotor bar copper loss decreases, however pushing the Nph to 30 will result in higher than acceptable values for the flux density, so as a compromise the value of 33 series turn per phase is elected at this point, in which the bar copper loss is reduced approximately 12 % compared to prototype-003v1 with 36 turns per phase.

3.6. Prototype-006

The main motivation behind this design variation is to decrease the rotor bar copper loss and also decrease the magnetic flux density (due to the decrease in Nph) by increasing the core length. However in this design variation the approach to this problem is by changing the geometry, as in the Design-004 we did this by changing the electrical configurations. In comparing the prototype-004v3(1.49 T peak) and the Reference Test Motor (1.62 T peak), it can be noticed that the stator back core flux density is comparably lower, and further can be stressed.

We decreased the stator back core and increased the Di , expanding the machine radially. However we fixated the rotor back core and allowed the rotor bar height to increase.

With this approach the rotor bar conductive area increases and further decreases the resistance and the copper loss as the results. Also by expanding the machine and increasing the D_i , magnetic flux tension will slightly decrease.

3.6.1. Geometric Modifications

3.6.1.1. Stator and Rotor Geometric Modifications

The radial expansion of the motor takes place by fixating the stator outer diameter, shaft diameter, and the rotor back core height, while stretching the stator inner diameter, and as such some other geometric properties will change in the process. The summary of the modifications and results is included here.

In Table 3.38 fifth column, it is noted that the stator back core flux density in the selected design (Prototyoe-004v3) is calculated to be 1.49 Tesla, however based on the reference point it can increase to approximately 1.62 Tesla. It allows for stator back core to shrink by a factor of 0.94.

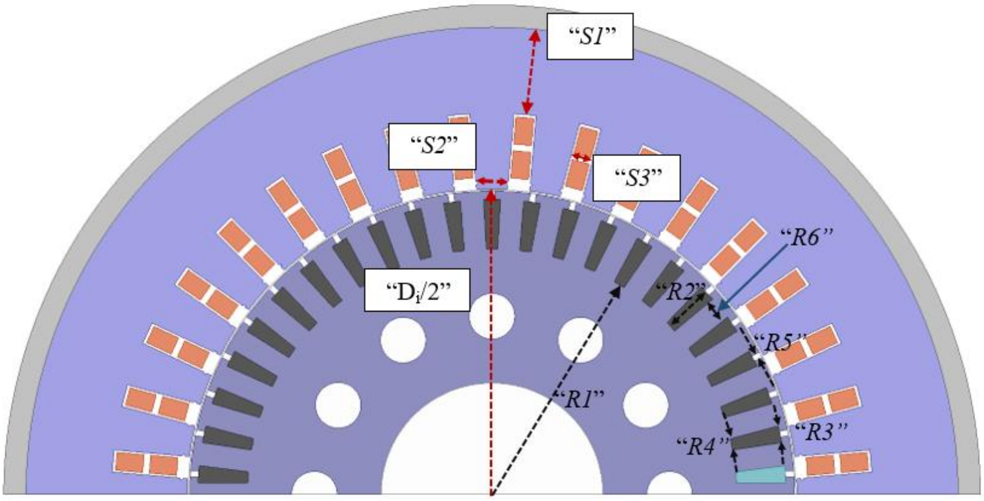

Figure 3.11. Stator and Rotor Lamination Schematics in Prototype-006

By keeping R1 constant, S1 is decreased by 2.46 mm, and as the results Di increases as well, due to the increase in the motor's inner radius S2, S3, R3, R4, and R6 is expanded. And by keeping R1 fixed, R2 is increase exactly as 2.46 mm. By this change we are able to increase the stator and rotor slot are, and thus decrease the resistance and copper loss in the conductors. The results are included in Table 3.41, and Table 3.42.

Table 3.39. *Prototype-006 Stator Slot Modification by Radially Expanding Stator Inner Diameter*

	Prototype-004v3	*Prototype-006v1*
Di [mm]	270	274.92
Slot pitch [mm]	23.56	24
S2 [mm]	13.78	14.03
S3 [mm]	9.78	9.97
S1 [mm]	41.16	38.69

Table 3.40. *Rotor Slot Modified Parameters in Prototype-006 based on Figure 3.11*

	Current Values	Modified Values
Rotor outer diameter [mm]	267.6	272.52
Slot pitch [mm]	18.27	18.61
R6 [mm]	15.59	15.89
R5 [mm]	2.67	2.72
ΔR2 [mm]	-	+2.46
R3 [mm]	7.46	7.6

3.6.2. Results and comparison

The main purpose of this modification was to increase the conductive area of the rotor bars in order to decrease the heat generation from the rotor bars. It is noted that the rotor bar resistive loss has dropped by an approximately 10 % to 1.43 kW.

Table 3.41. *Rotor Bar Copper Area Comparison After Radially Increasing the D_i*

	FEM 2D		
	Reference	Prototype-004v3	Prototype-006v1
Rotor slot copper area [mm^2]	148.16	124.0	142.0
Solid Loss (FEM)[kW]	1.18	1.57	1.43

Table 3.42. *Magnetic Properties After Rotor Bar Copper Area Expansion Due to Radially Increasing the D_i*

	B Peak		
	Reference	Prototype-004v3	Prototype-006v1
Stator-Teeth Flux Density (T)	1.46	1.51	1.46
Stator-Yoke (T)	1.62	1.49	1.55
Rotor-Teeth Flux Density (T)	1.74	1.82	1.73

3.7. Prototype-007- Modelling Defects, and Corrections

After inspecting the 3D model sent to us by ELSAN we noticed that the rotor bar and end ring connection have not been truly reflected in the computer model. There was a slight miscalculation in the modeling. Additionally, the temperature setting of the rotor cage was not representing the actual condition of the simulation that we had planned. These two problems are going to be discussed in this section.

3.7.1. Rotor Bar and End Ring Connection Re-Modelling

The 3D model of the connection of the rotor bars and the rotor end ring is as follows:

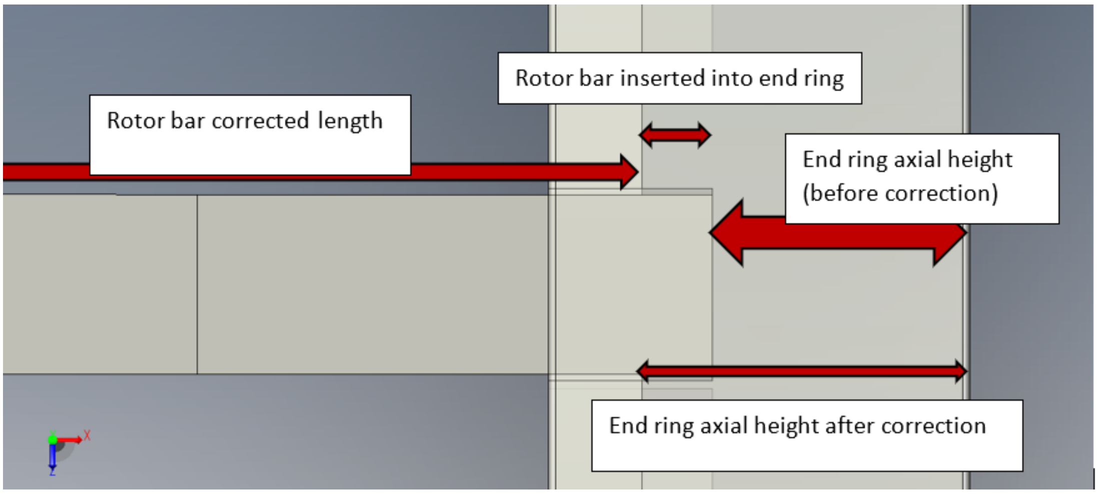

Figure 3.12. 2D Schematic of the Rotor Bar and Rotor End Ring Connection of the Actual Motor

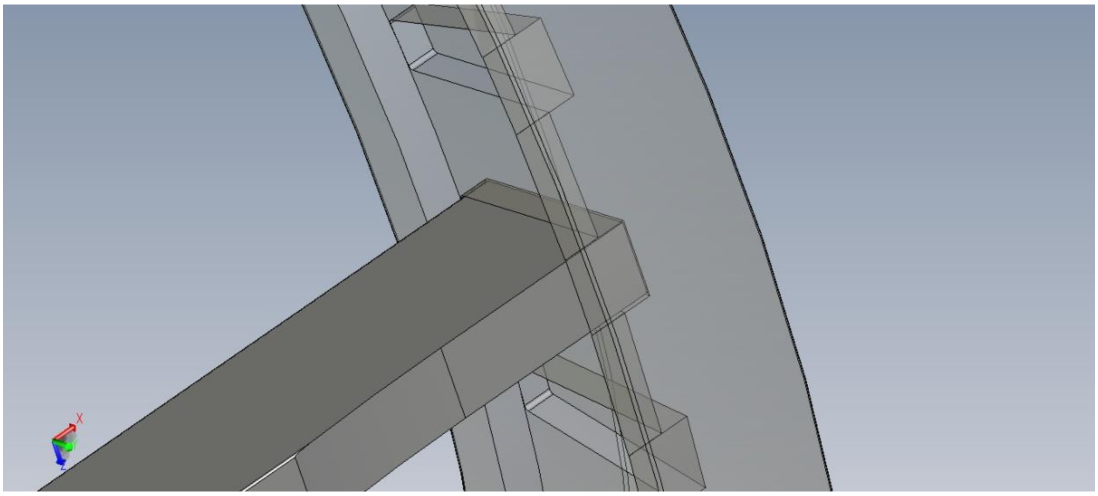

Figure 3.13. 2D Schematic of the Rotor Bar and Rotor End Ring Connection of the Actual Motor

In obtaining the rotor bar length and rotor end ring axial length the wrong values have been selected. However, after an observation the values have been updated accordingly, and the simulations are repeated by just correcting this parameter, all the other settings remain the same. The prototype-007v1 is the updated version of the prototype-006v1 after the rotor bar connection is fixed.

3.7.2. Rotor Cage Temperature Setting in ANSYS Maxwell

In constructing the FE 2D model some parameters are inherited from the RMxprt. One being the temperature of the rotor bars and the rotor short circuit end rings.

The ANSYS shared material library includes the materials with their properties at the standard reference point of 20 degrees Celsius. And as you set a temperature for your operating conditions in RMxprt, it changes the material properties and create a new material at the operating temperature to be used in the FE environment. However when selecting a material in RMxprt environment for the rotor bars and the rotor end rings the selected materials properties should be at 75 degrees Celsius. In the previous simulations the material selected in the RMxprt was in 20 degrees Celsius.

In these simulations this problem has been fixed and the correct material at correct temperature have been used in both RMxprt and the FEM environment. The resistivity of the material selected for the FEM simulations reflects the correct resistivity at the operating temperature.

Since our design method is an iterative process and we took the Reference Test Motor as the reference, this resistivity change does not change the design and selected values since we took actions based on the reference point. And since changing resistivity will also change the reference point so our parameters and design criteria are in the desired range. However, this action will represent the true and correct values of the rotor resistance.

The Changes discussed in this section will be applied and the results from this pint forward use the updated values.

3.8. Stator Cooling Ducts Thermal Investigation

We would like to investigate the effect of the stator cooling ducts , but this requires an iterative process, to avoid iterations I assume a fixed loss values for different cases of a thermal analysis and monitor the temperature levels from the fixed losses, and by doing this it gives us an idea which duct dimension to use.

In order to further investigate the effects of the geometry on the fluid flow and thermal stability of the system, 3 different design variation have been inspected regarding the stator cooling channels.

- Scenario A: Stator vents radial height set to 1 cm.
- Scenario B: Stator vents radial height set to 0.5 cm.
- Scenario C: Stator vents totally closed.

Schematics corresponding to the three scenarios can be seen Figure 3.14, Figure 3.15, and Figure 3.16. Loss Values for investigation is the loss values calculated from the electromagnetic analysis of design-002v1. The results are included in Table 3.43.

Table 3.43. Loss Components Used as Heat Source in Stator Cooling Ducts' Thermal Investigation

Motor Part	*Type of Loss*	*Loss [W]*	*Volume [dm^3]*	*Loss Value [w/dm^3]*
Stator	Stator Core Loss	1543	15.13	102
Stator Winding	Stator Copper Loss	4730	1.94	2438.1
Rotor	Rotor Core Loss	485	8.35	58.1
Rotor Cage	Rotor Copper Loss	2760	2.45	1126.5
Frame	Frame Core Loss	206.4	3.1	66.6

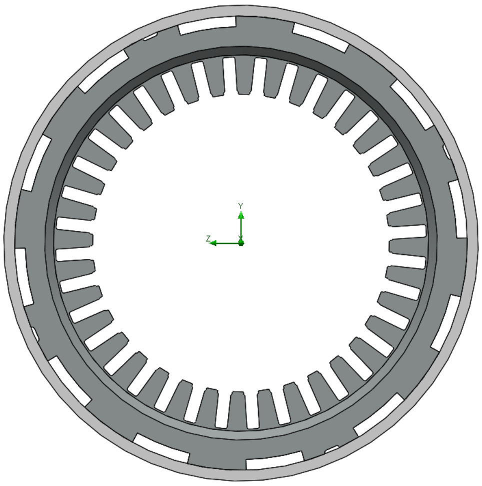

Figure 3.14. Scenario A : Stator Vents' Radial Height Set to 1 cm

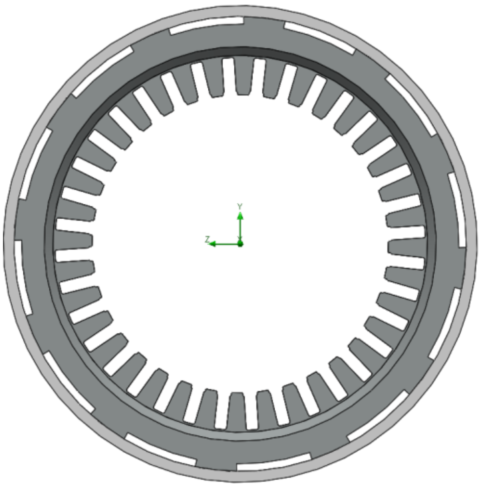

Figure 3.15. Scenario B : Stator Vents' Radial Height Set to 0.5 cm

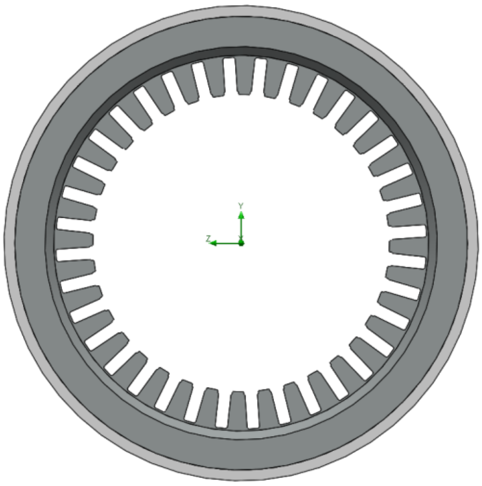

Figure 3.16. Scenario C: Stator Vents' Radial Height Totally Closed

Result of the Fluid Flow and thermal analyses performed in these three different scenarios, is shown in Table 3.44.With that in mind closing the stator cooling channels is not suggested since it noticeably reduces the air flow and the fan's utilization factor drops. Because when closing the ducts the pressure drop is significant compared to the others and so cooling capacity decreases.

Table 3.44. *Average Temperature Comparison on Motor's Components Regarding the Stator Cooling Channels' Configuration*

Component	*Scenario A*	*Scenario B*	*Scenario C*
Stator winding temperature [˚C]	140.7	143.3	138.6
Stator Core Temperature [˚C]	107.1	103.5	115.2
Rotor Core Temperature [˚C]	116.9	121.8	114.9
Rotor Cage Temperature [˚C]	133.8	140.6	137.1
Frame Temperature [˚C]	100.5	93	115.1
Pressure Drop [Pa]	789.4	804.2	1287.7
Air Flow [m^3/s]	0.243	0.242	0.193

However considering the two remaining options, the two options have a close thermal outcome and in order to favor the magnetic flux density in the stator back core stator cooling channels with 0.5 cm radial height is favored.

3.9. Prototype-008 (Final Design)

Development and manufacturing of a motor is not merely based on the electromagnetic solution and analysis. For cooling purposed in addition to the cooling ducts on the rotor core , a stator ventilation system also has been considered and analyzed concerning the fluid dynamics aspect of the problem. 3 different scenarios have been analyzed regarding the thermal management. And it has been decided to use a 0.5 cm stator cooling ducts.

Based on the previous iterations, including the ducts will further increase the magnetic flux density in the air gap. 2 different scenarios have been investigated.

1. include the 0.5 ducts on prototype-007v1

2. reduce the duct from 1 cm to 0.5 cm on prototype-003v1

In the final design based lamination of the prototype-003 and the winding configuration of the prototype-007is selected. As well as increasing the core length to maximum 230 mm to compensate for the increase in the flux density.

3.9.1. Motor Data

In this section the characteristics and details of the model is given, and the detailed performance of the motor is discussed in chapter 4.

3.9.2. Main Dimensions

Motor’s main dimensions which has been determined is logged in Table 3.45.

Table 3.45. *Pototype-008 Main Dimensions*

Geometric Components	*Value*
Stator Outer Diameter [mm]	420
Stator Inner Diameter [mm]	270
Rotor Outer Diameter [mm]	267.6
Rotor Inner Diameter [mm]	100
Core Length [mm]	230
Frame Inner Diameter [mm]	420
Frame Outer Diameter [mm]	440
Stator Slot	36
Rotor Slot	46

3.9.2.1. Stator Slot

The stator slot typical schematics is shown in Figure 2.3 And the dimensions are given in Table 3.46.

Table 3.46. *Prototype-008 Stator Slot Dimensions*

Parameter	*Value*
Hs0 [mm]	1.8
Hs1 [mm]	1.63
Hs2 [mm]	30.5
Bs1 [mm]	10.57
Bs2 [mm]	8.46
Number of Slots	36

3.9.2.2. Rotor Slot

Rotor slot schematics is also as shown in Figure 2.3. Table 3.47 provides the data for the design.

Table 3.47. *Prototype-008 Rotor Slot Dimensions*

Parameter	*Value*
Hs0 [mm]	3.74
Hs01 [mm]	0
Hs1 [mm]	0.2856
Hs2 [mm]	17.58
Bs0 [mm]	2.68
Bs1 [mm]	6.58
Bs2 [mm]	4.14
Rs	0.4
Number of Slot	46

3.9.3. Winding Configuration

3.9.3.1. Stator Winding Arrangements

The winding of the motor is a hairpin type winding, and the using the hairpin winding gives us some advantages over to the stranded type winding. The application intended in this study is geared towards traction applications so it is beneficial to use the hairpin winding. By doing so we utilize the space available more efficiently and as such the current density drops and so reduces the copper loss generated in the stator windings, and next considering the same condition for both types it gives us the flexibility to increase the series turns per phase. The winding configurations selected in Chapter 3 is summarized in Table 3.48.

Table 3.48. *Winding Configurations Designed for the Manufactured Prototype*

Parameters	*Winding v1.0*	*Winding v1.1*	*Winding v2.0*
Coil Pitch	7 slots	7 slots	7 slots
Winding Type	hairpin	Stranded	Hairpin
Conductor per Slot	11+11	11+11	6+6
Parallel Branch	4	4	2
Strands per Conductor	2 strands	7 Strands	1 Strand
Conductor Size	3.55 mm (Width) × 0.94 mm (Height)	1.1 mm	7.6 mm (Width) × 2 mm (Height)
Winding Layers	2 Layers	2 Layers	2 Layers
Net Copper Area [mm^2]	146.83	146.35	182.4
Fill factor %	49.2	49.1	61.1
Series Turns per Phase	33	33	36

The reason for selecting three different variants for the winding configuration is the manufacturing difficulties and challenges. In order to be able to perform the tests it was decided to do the winding as stranded type in the ELSAN, 1st manufactured prototype with stranded winding. The manufactured prototype which has been used in taking the measurements, utilizes the winding v2.0.

As it can be seen in Table 3.48 using the hairpin winding allows for the fill factor to increase by approximately 24 %. Which gives us the flexibility to utilize the extra space on increasing the turns per phase while keeping the per phase resistance at a desired level with its counterpart, so that we can further address the increased flux density at cross section on the motor.

3.9.3.2. Rotor Winding Arrangements

The rotor cage consists of two main parts, rotor bars and end short circuit rings. The bars and end rings are a copper alloy named CuCrZr, which are inserted into slots and by using a silver based soldering solution they have been connected to each other. The rotor bars are constructed to fit the rotor slots, with the end connections are detailed at Table 3.49.

Table 3.49. *Rotor Bars and End Rings End Connection- Prototype-008*

Parameter	*Value*	*Description*
End Length [mm]	33	Single-side end extended bar length
End Ring Width [mm]	14	One-side width of end rings (in axial direction)
End Ring Height [mm]	31.4	Height of end rings (in radian direction)

3.9.4. Material

The material that has been used in the motor is as included in Table 3.50.

Table 3.50. *Material Used in Simulation Model of Prototype-008-“ Manufactured Motor”-*

Component	*Material*
Stator Lamination	COGENT SURA M530-50A
Stator Winding	Hairpin Copper winding
Rotor Lamination	COGENT SURA M530-50A
Rotor Cage	CuCrZr
Frame	Cast Iron

. For the core material a typical non-grain-oriented steel has been selected and a new material has been created in ANSYS Maxwell’s Library.

Considering the rotor bars and the short circuit end rings , as it has been discussed in the literature [21]–[24] due to its strength of added zirconium and it being a copper alloy , CuCrZr is preferred for traction applications. As this is a traction application which requires a lower resistance compared to a more convenient Aluminum option, a Copper alloy is used for this purpose. The alloy selected offers approximately 80 % IACS, in which 100% IACS conductivity is 58.2 MS/m. A manufacturer in Italy named “METALMINOTTI” offers rotor bars and short circuit ring with 47 MS/m, which is used in our motor.

CHAPTER 4

DEVELOPMENT, MANUFACTURING, AND TESTING THE FINAL PROTOTYPE

4.1. Introduction

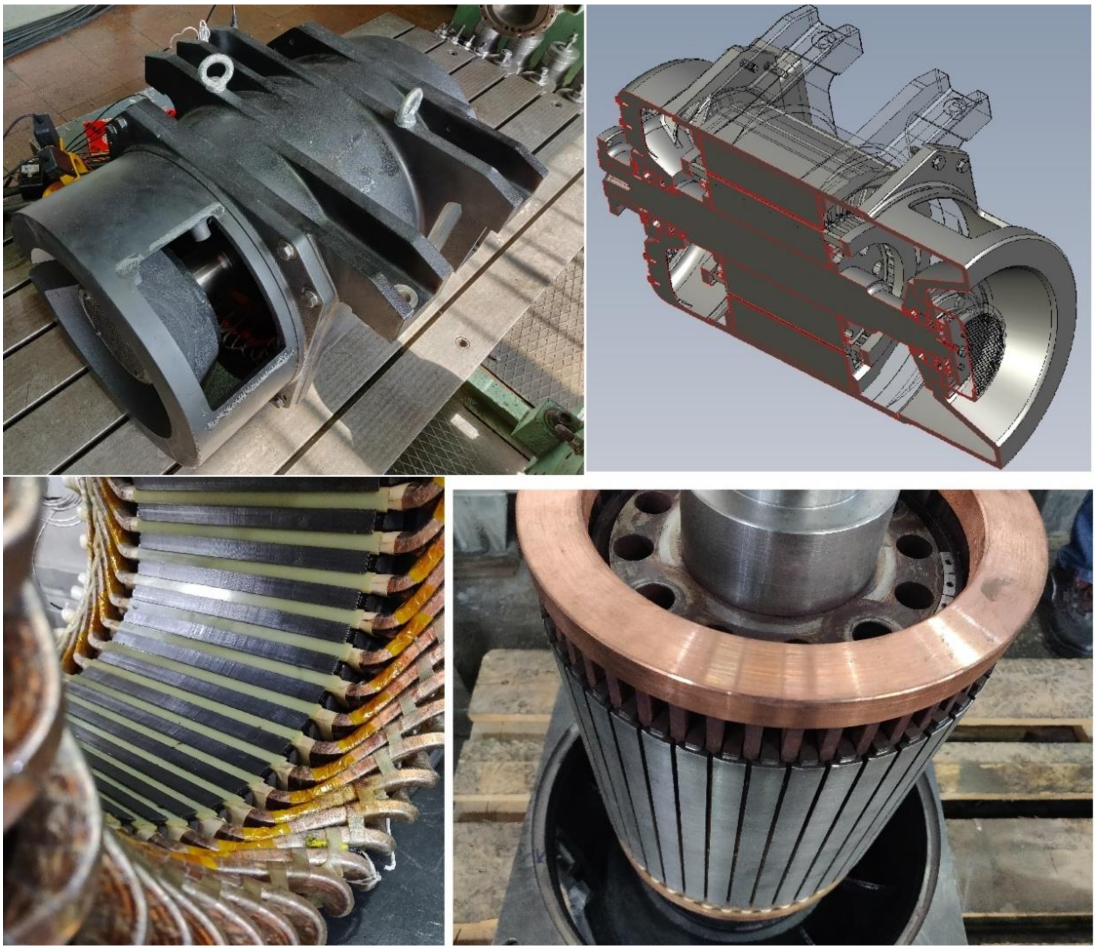

Figure 4.1. Top Right : 3D Model of the Motor, Top Left: Completed Motor, The Fan Intake is Visible-No Fan is Connected, Bottom Right: Rotor Core and Rotor Cage, The Rotor Short Circuit Ring and Rotor Cooling Channels are Visible, Bottom Left: Stator Core and Flat Type Windings are visible

In this chapter the tests have been performed on manufactured traction induction motor with respect to IEC 60349-1,2,3 , IEEE Std 112-1996, and IEEE Std 11-2000 standards .The motor is expected to meet the characteristics that was set by the target performance, and Finite Element analyses have been carried out to be compared with the measurement data so that the FE model and methods can be verified.

4.2. Target Performance

The manufactured motor should be able to satisfy the target performance required by the traction application, the tractive effort and requirements of the motor is explained in Section 3.1.5.

4.3. Manufactured Motor Characteristics

4.3.1. Rated Performance

The rated values of the designed and manufactured motor are included in the Table 4.1. The motor’s main dimensions are included at Table 3.45, with stator winding configuration of v2.0 as mentioned in Table 3.48. The materials used in the motor is mentioned in 3rd Chapter at Table 3.50.

Table 4.1. *Manufactured Prototype- Rated Performance*

	Value
Connection	504 V
Frequency	70 Hz
Shaft Speed	2068 rpm
Pole Number	4
Rated Current	181.1
Power Factor	0.87
Output Power	125 kW
Cooling System	Outer Fan cooled

4.4. Finite Element Modelling

The FE modelling procedure is exactly the same as already discussed in Sections 2.5.1, 2.5.2, 2.5.3, and 2.5.4 , with a slight change in the mesh element which is included at Table 4.2.

Table 4.2 *Mesh Operations Used for Modelling Manufactured Motor*

Mesh Refinement	*Maximum Element Length*	*Mesh Elements*
Band	0.2 mm	59248
Bars	2 mm	4738
Frame	3 mm	3420
Inner Band	1 mm	21666
Outer Band	1 mm	1040
Rotor	3.5 mm	18412
Stator	3.5 mm	14090
Sum	-	126694

4.5. Measurement

4.5.1. Test Setup

The test setup is already explained at Section 2.3, the same exact test bench is used with the same measuring equipment as shown in Figure 2.5, and Figure 2.6.

4.5.2. Current Transformers

HIOKI 3194 Current sensor is limited to 65 Amps and for this reason it is accompanied by the current transformers which are shown in Figure 4.2. However, using the current transformers in the measurement has some disadvantages which will be discussed. Such as applying a phase shift and thus altering the power factor and as the result changing the active power recorded by the device.

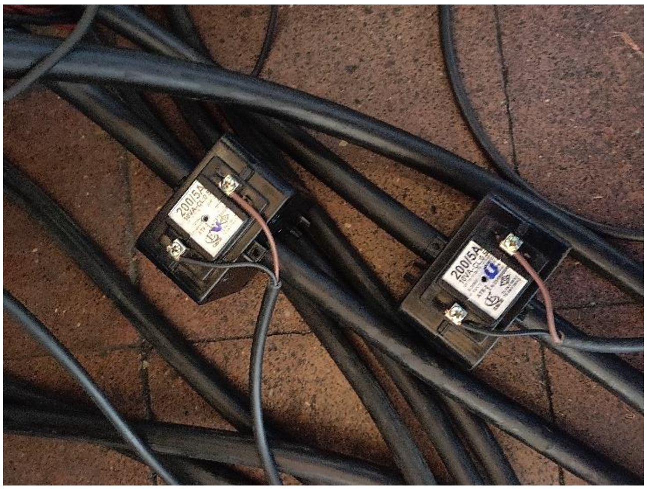

Figure 4.2. Current Transformers

Table 4.3 includes the calibration data for the 50 Hz mode of operation. As it can be seen based on the true magnitude of the current and the power factor the phase shift is recorded. For example, if a current of 100 Amp with a PF of 0.05 is being measured, the recorded value by the device will be equal to 0.0546 which is the result of reducing the phase shift by 0.27 Degrees.

By utilizing MATLAB and using its interpolation function the corrections are done, based on the current logged by the device.

Table 4.3 *The Phase Displacement Introduced by the CTs in Degree*

50 Hz	0.05 PF	0.08 PF	0.2 PF	0.5 PF	0.8 PF	1.0 PF
	Phase Displacement in Degree					
2 Amps	-0.16	-0.17	0.05	0.71	1.40	2.23
10 Amps	-0.22	-0.20	-0.10	0.35	0.83	1.46
20 Amps	-0.26	-0.23	-0.14	0.18	0.52	0.99
40 Amps	-0.27	-0.25	-0.17	0.09	0.37	0.79
100 Amps	-0.27	-0.26	-0.20	-0.03	0.20	0.56
200 Amps	-0.28	-0.27	-0.22	-0.06	0.04	0.35
240 Amps	-0.28	-0.27	-0.22	-0.08	0.03	0.33

However if we calculate the error percentage introduced by the CT in the power factor measurement as seen in Table 4.4, we notice that the phase shift is only important in the No-Load operations with low power factor. And as the power factor increases the effect of the CT is being greatly diminished in which at 0.8 to 1.0 PF the CTs maximum PF change is only 1.8 % which happens at very low current values of 2 to 10 Amps.

As the results The CTs are taken into effect in the no-load operations.

Table 4.4 *Power Factor Error Percentage Introduced by the CTs*

50 Hz	0.05 PF	0.08 PF	0.2 PF	0.5 PF	0.8 PF	1.0 PF
2 Amps	5.5	3.8	-0.4	-2.1	-1.86	-0.076
10 Amps	7.8	4.3	0.9	-1.0	-1.09	-0.032
20 Amps	8.9	5.1	1.2	-0.5	-0.68	-0.015
40 Amps	9.2	5.4	1.4	-0.3	-0.49	-0.010
100 Amps	9.3	5.5	1.7	0.1	-0.26	-0.005
200 Amps	9.8	5.8	1.8	0.2	-0.05	-0.002
240 Amps	9.7	5.8	1.9	0.3	-0.04	-0.002

4.5.3. PT100 Temperature Sensors

In order to measure the temperature of the motor, PT100 sensors are connected to four different spots of the motor and also by using the infrared thermometer the outer temperature of the frame is measured at designated spots on the motor, and also for measurement of the stator winding temperature, the resistance measurement method is used based on the standard IEC 60439-2:2000. PT100 sensors are located at the end windings of the stator, 4 PT100 sensors are used in 2 pairs located at axes perpendicular to each other, as is seen in Figure 4.3.

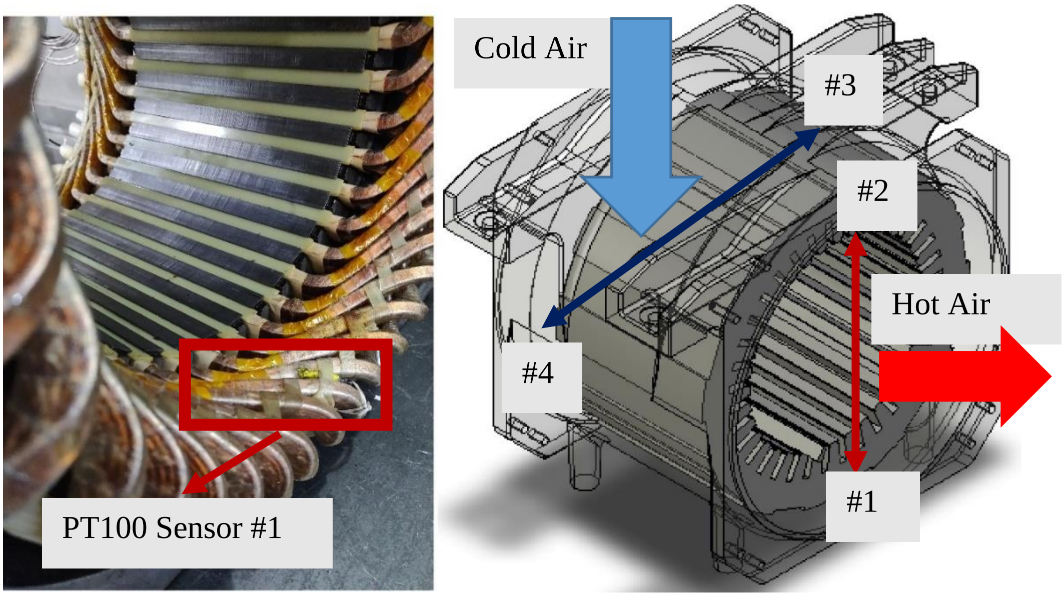

Figure 4.3. PT100 Locations

4.6. Results

The manufactured motor is tested under different scenarios and the results are included in this section. However the purpose of performing these tests is to verify the manufactured motor by comparing the test results with the target performance. The target performance is already determined in Section 3.1.5 with its tractive effort diagram Figure 3.3 and its rated performance at continuous mode at Table 3.4.

Our manufactured motor is tested at 5 different frequencies and its tractive characteristics is included at Section 4.7.

4.6.1. 50 Hz – Sinusoidal Drive

In this test the motor is directly connected to the generator in order to omit the effect of the loads in the factory, affecting the test condition.

4.6.1.1. No-Load Test

The No-Load have been performed for the same machine with 4 parallel paths, and in order to create the same condition for the rated voltage of 360 Volts, the test are performed at 180 Volts. The No-Load test is shown in Figure 4.4.

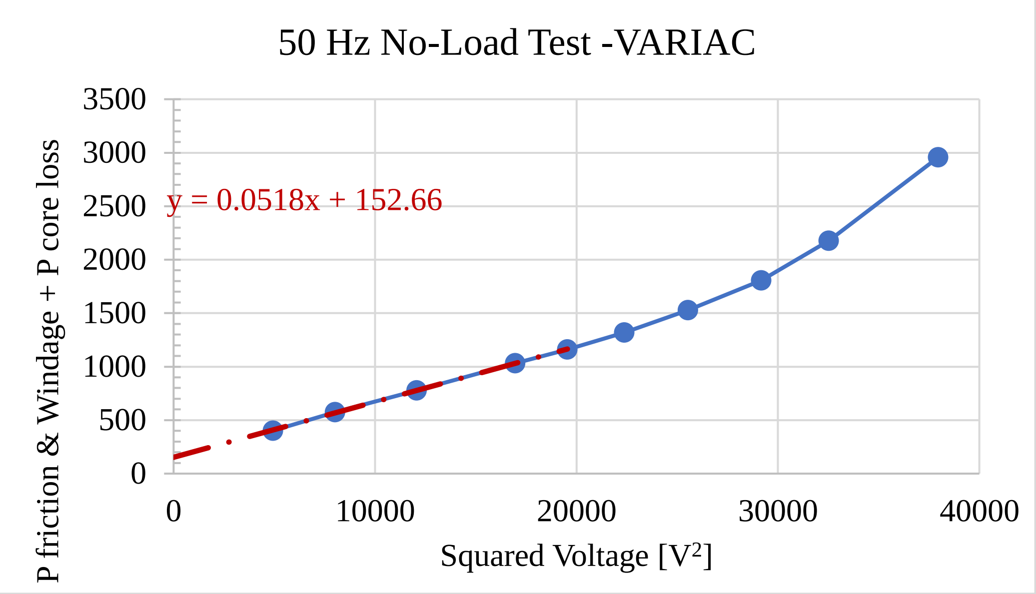

Figure 4.4. 2nd Prototype- 50 Hz No-Load Test Plot-VARIAC-(Solid Blue Line is Measured Power; Dashed Red is the Linear Curve Fit)

Table 4.5 *2nd Prototype- 50 Hz No-Load Test -VARIAC Results*

Voltage [L-L rms]	Voltage [L-L rms]	P mech [W]	P fe [W]
Not Calibrated	180	152.7	2023
Calibrated	180	156.0	1817

However, in the final prototype the winding configuration has corrected to the originally estimated 2 parallel paths. And the core loss and mechanical loss values calculated in this section will be used.

No-Load test has been performed with both sinusoidal source and PWM source and the results is visible in Figure 4.5.

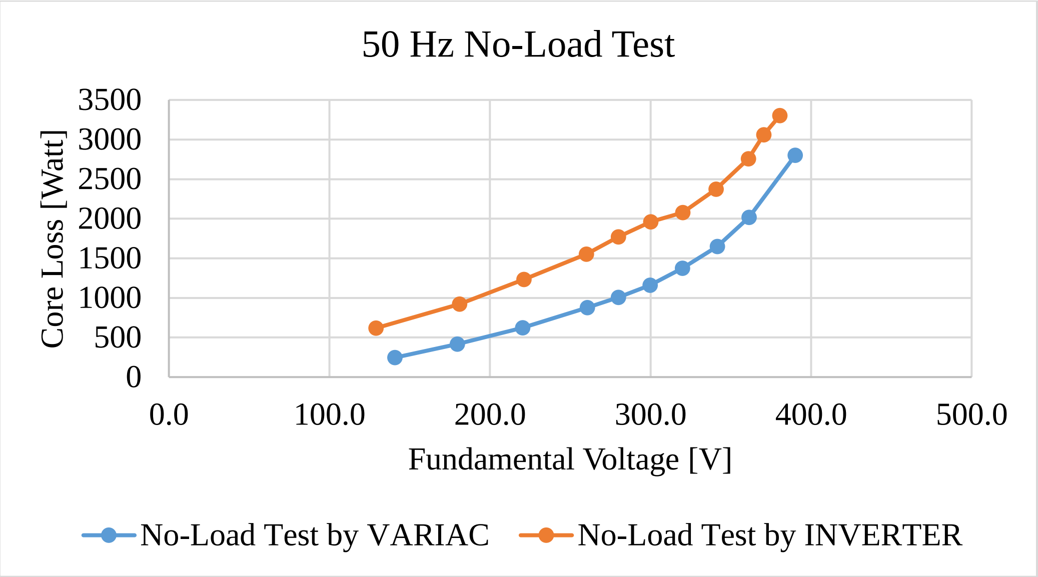

Figure 4.5. 2nd Prototype- 50 Hz No-Load Test comparison Plot, Inverter Vs. Sinusoidal source

After Calibrating the data recorded by the HIOKI 3194 and correcting the phase shift due to the Current Transformers the corrected data is included in Table 4.5.

4.6.1.2. Steady State Temperature, Resistance Measurement:

In order to determine the performance parameters of the motor it has been tested under a condition mentioned in to reach thermal steady-state.

Table 4.6. Testing Condition for 50 Hz, Sinusoidal Drive Mode, 574 Nm Torque

Parameter	*Value*
Measuring Equipment	HIOKI-3194
CT Connected	YES
Test Type	Under-Load
Main Source/ Connection	Gen -Motor
Rated Voltage	360 V-LL-rms
Rated Frequency	50
Rated Torque	574 N.m
Fan Connected	YES

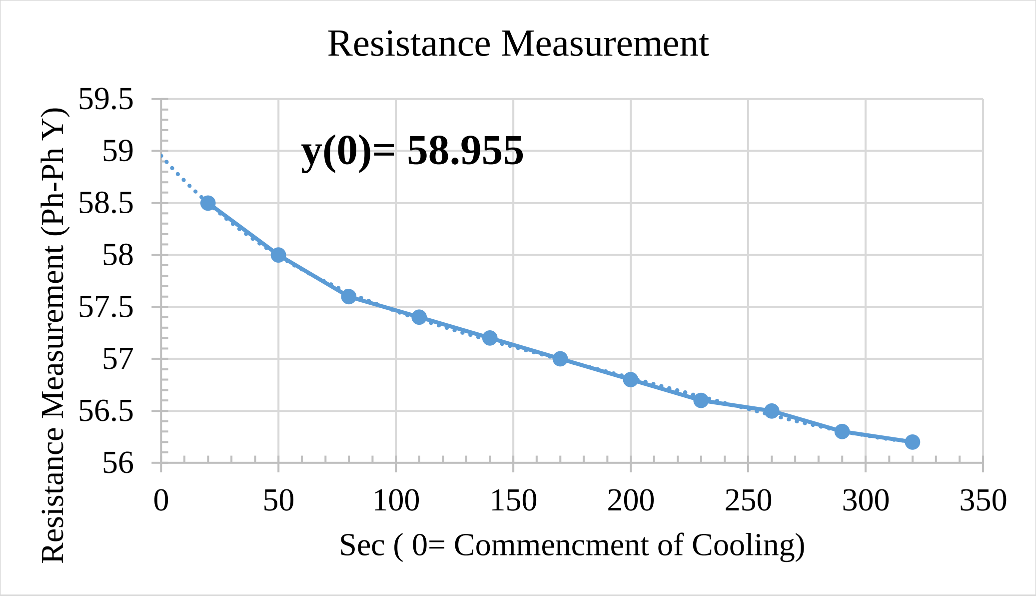

Figure 4.6. Temperature Measurement Based on the Resistance Method, 50 Hz, 574 Nm, Sinusoidal Source

In order to determine the average temperature of the motor at operating condition, based on Standards IEC 60349-2, since it takes time to stop the motor to standstill a series of resistance data should be taken so that it is possible to extrapolate to find the resistance at the instance of shutting the motor down.

Based on the plot the average resistance of the motor while operating is estimated to be 29.47 mΩ. Motor's cold-steady-state, and operating temperature is at Table 4.7.

Table 4.7 *Averaged Steady State Cold temperature*

Motor Temperature [˚C]	16.5
Stator Per Phase Resistance [mΩ]	22.3 Ph-Ph

And in order to estimate the temperature at the operating point the following Equation (4-1) is used.

$$\frac{R_2}{R_1} = \frac{T_2 + 235}{T_1 + 235} \qquad (4\text{-}1)$$

4.6.1.3. Performance Evaluation Under Load: [T rated = 574 N.m]

In all the load tests the fan is installed on the motor. It is worth noting that the test is carried out as the motor was in thermal steady state, and in order to analyze the test data, FE simulations have been run so that the FE model and the manufactured motor could be verified. The FE simulations are being simulated in ANSYS MAXWELL in a 2D environment.

Resistance comparison:

Table 4.8. *Resistance Comparison 50 Hz under Thermal Steady-State with 574 Nm Torque*

1st Prototype	Test	FE
Ambient Temp	16.5 ˚C	-
Avg. Resistance @ 16.5 ˚C [Thermal S.S.]	22.3 mΩ	22.5 mΩ
Estimated Op. Temp. at 574 N.m	29.47 mΩ ≙ 97.54 ˚C	100 ˚C
PT100 Sensors [#1] – [#4] Sinusoidal @ Thermal S.S	98 ˚C – 52 ˚C	-
PT100 Sensors [#1] – [#4] Inverter @ Thermal S.S	114 ˚C – 63 ˚C	-

results posted here is related to the rated torque operating condition. All the parameters are obtained with HIOKI 3194 while Filter off, unless mentioned otherwise, and the fan is connected to the motor while motor is under load.

4.6.1.3.1. Results: [T rated = 574 N.m]

Table 4.9 *Manufactured Motor Performance Comparison FE, Measurement, 50 Hz, 574 Nm*

	2nd Prototype			Description
	Test Sine	Test Inverter	FE 2D Sine	
Test Condition	-	-	-	Thermal Steady State
St. Wdg. Avg. Temp.	97.4 ˚C	104.9 ˚C	100 ˚C	
PT100	98/52	114/63	-	[#1] / [#4] ˚C
Voltage [V,rms]	360	360	360	Line-Line
Connection	Y	Y	Y	
Current [A rms]	181.0	178.7	171.1	
Shaft Speed (r.p.m)	1470.0	1468	1468.1	
Torque [N.m]	574.9	574.0	575.5	
Actual Power input	98.60	98.65	94.876	Pin=Pout+Total loss [kW]
Reactive Input Power	55.08	55.64	51.67	kVar
Power Factor	0.8730	0.8710	0.8782	$cos(\varphi) = Pin \div (3 \times Vph \times Iph)$
Output Power(kW)	88.5	88.23	88.407	torque × Shaft speed
Total Power Loss (Indirect) [kW]	7.432	8.267	6.476	P cu, s+Pcu, r+Pcore+Pf&w+Pstray
Total Power Loss (Direct) [kW]	10.099	10.416	-	P in – Pout
Efficiency Indirect	92.25	91.4	93.18	(P out)/ (P out + P total loss)
Efficiency Direct	89.7	89.4	-	Pout/Pin

4.6.1.3.2. Loss components: [T rated = 574 N.m]

Table 4.10 *Manufactured Motor Loss Segregation Comparison FE, Measurement, 50 Hz, 574 Nm*

	2nd Prototype			Description/ Definition
	Test Sine	Test VACON	FE 2D Sine	
Airgap [mm]	1.2	1.2	1.2	Radial Gap
Time step	-	-	50	
Non-linear residual	-	-	1e-08	
s	0.02	0.021	0.021	Slip
Pcu, s (kW)	2.899	2.887	2.78	Stator copper losses
Pfe (kW)	2.023	2.76	1.476	Iron losses
Pfe (kW) + Core Effect	2.023	2.76	2.185	
P stray (kw)	0.493	0.493	-	P stray=0.005× P in
Pcu, r (kW)	1.863	1.973	2.072	Rotor copper losses
Pmech (kW)	0.153	0.153	0.153	Mechanical Losses(f&w)
Solid Loss (FEM)[kW]*	-	-	1.58	FEA Loss “Solid Loss”
$P_{er,\ rotor}$ [kW]	-	-	0.493	Rotor end rind ohmic loss (analytical)
P out [kW]	88.5	88.23	88.407	
Total Power Loss (Indirect)	7.432	8.267	6.474	Ptot=Pcu, s+Pcu, r+Pfe+Pmech+Pstray
Total Power Loss (Direct)	10.099	10.416	-	P in – Pout

4.6.2. 50 Hz- Inverter Drive

In this test the motor is being driven by the VACON inverter with the switching frequency of the 6kHz setting. The inverter is being fed by the grid. The tests performed with the inverter supply and the supply frequency of the 50 Hz are at the thermal steady state .

4.6.2.1. No-Load Test

In order to estimate the friction and windage losses as the motor is driven from the inverter source the data from the previous section is used (since the shaft speed is the same the friction and windage losses are assumed to be the same as well). However in order to calculate the core loss at the rated voltage the no-load test with inverter supplied is used. The same exact procedure in Section 4.6.1.1 is applied to determine the no load loss.

Now that the raw data of the tests are obtained, since current transformers have been used in this test as well the recorded data should be calibrated , the results is included in Table 4.11.

Table 4.11. *50 Hz PWM No-Load Test Data Calibration w.r.t CT*

	Voltage [rms]	R	Temp	P mech [W]	P fe [W]
NOT Calibrated	360	23.50 mΩ	29.54 ˚C	153.0	2760.0
Calibrated	360	23.50 mΩ	29.54 ˚C	156.0	2474.0

4.6.2.2. Steady State Temperature, Resistance Measurement

The motor is tested under the condition stated in the Table *4.12* And the operating temperature is determined based on the resistance measurement method explained in Section 4.6.1.2 by extrapolating the resistance measurement. The estimated average stator winding's temperature is 104.9 ˚C,

Table 4.12. *2^{nd} Prototype, 50 Hz Inverter Driven Testing Condition*

Parameter	*Value*
Measuring Equipment	HIOKI-3194
CT Connected	YES
Test Type	Under-Load
Main Source/ Connection	Grid -Inverter
Rated Voltage	360 V-LL-rms
Rated Frequency	50
Rated Torque	574 N.m
Fan Connected	YES

Table 4.13. *Manufactured Motor's Estimated Operating Temperature at 50 Hz, 574 N.m- Sinusoidal Source Compared with Inverter Source*

Temperature Measurement based on Resistance Method	Cold Steady State Temperature	Steady State Operating Temperature-Inverter Source [Estimated]	Steady State Operating Temperature-Sine Source [Estimated]
Motor Temp[˚C]	16.5 ˚C	104.9 ˚C	97.4 ˚C
Stator Ph-Ph Resistance[mΩ]	44.6 mΩ	60.275 mΩ	58.95 mΩ

4.6.3. 70 Hz – Inverter Drive

4.6.3.1. 70 Hz No-Load tests

It is assumed that the friction and windage losses are directly related with the mechanical shaft speed of the motor and as such the below equation can be derived:

$$\frac{P_{f\&w\,2}}{P_{f\&w\,1}} = (\frac{shaft\ speed_2}{shaft\ speed_1})^2 \qquad (4\text{-}2)$$

As determined in the previous sections by applying sinusoidal source the friction and windage loss is determined at 50 Hz, shaft speed, and due to the fact that the measurements at 70 Hz is done while the motor is connected to an inverter results in an increased core loss and it will be difficult to determine the convergence point of the no load test curve without sufficient data at low voltage. And for that reason the friction and windage loss is calculated analytically based on Equation (4-2) and core loss is determined using the same procedure used in Section 4.6.1.1 (50 Hz no-load test). The results are included at Table 4.14.

Table 4.14 *70 Hz No-Load Test Data Calibration w.r.t Current Transformers*

	Voltage [L-L rms]	P mech [W]	P fe [W]
No CT Calibration	504	300	3561
With CT calibration	504	300	3314

4.6.3.2. Steady State Temperature, Resistance Measurement

The motor is tested under the condition stated in the Table 4.15 and the operating temperature is determined based on the resistance measurement method explained earlier. The results are included at Table 4.16.

Table 4.15 *Testing Condition*

Parameter	*Value*
Measuring Equipment	HIOKI-3194
CT Connected	YES
Test Type	Under-Load
Main Source/ Connection	Grid -Inverter
Rated Voltage	504 V-LL-rms
Rated Frequency	70
Rated Torque	574 N.m
Fan Connected	YES

Table 4.16. *Manufactured Motor's Estimated Operating Temperature at 70 Hz, 574 N.m, with Inverter Source*

Temperature Measurement based on Resistance Method	Cold Steady State Temperature	Steady State Operating Temperature-Inverter Source [Estimated]
Motor Temp[˚C]	16.5 ˚C	105.6 ˚C
Stator Ph-Ph Resistance[mΩ]	44.6 mΩ	60.4 mΩ

4.6.3.3. Performance Evaluation Under Load [T rated = 574 N.m]

4.6.3.3.1. Resistance comparison

Table 4.17. *Resistance Comparison 70 Hz under Inverter Driven at Thermal Steady-State with 574 Nm Rated Torque*

2nd Prototype	Test	FE
Ambient Temp	19.20 ˚C	-
Avg. Resistance @ 16.5 ˚C [Thermal S.S.]	22.30 mΩ	22.48 mΩ
Estimated Op. Temp @ rated Torque 574 N.m	60.4 mΩ ≙ 105.9 ˚C	100 ˚C
PT100 Sensors [#1] – [#4] @ Thermal Steady State	97 ˚C – 60 ˚C	-

4.6.3.3.2. Results: [T rated = 574 N.m]

Table 4.18. *Manufactured Motor Performance Comparison FE, Measurement, 70 Hz, 574 Nm*

	2nd Prototype		Description
	Test Inverter	FE 2D Sine	
Test Condition	S.S	-	
St. Wdg. Avg. Temp.	105.9 ˚C	100 ˚C	
PT100 [#1]/[#4] ˚C	97/60	-	
Voltage [V,rms]	504	504	Line-Line
Connection	Y	Y	
Current (A rms)	179.62	170.8	
Shaft Speed (r.p.m)	2068	2068.6	
Torque (N.m)	575.4	575.4	
Actual Power input kW	136.28	132.9	Pin=Pout+Total loss
Reactive Input Power	78.32	74.6	kVar
Power Factor	0.8670	0.8720	$cos(\varphi) = Pin \div (3 \times Vph \times Iph)$
Output Power(kW)	124.61	124.65	torque × Shaft speed
Total Power Loss (Indirect)	9.433	8.25	P cu, s+Pcu, r+Pcore+Pf&w+Pstray
Total Power Loss (Direct)	11.67	-	P in – Pout
Efficiency Indirect	93.0	93.7	(P out)/ (P out + P total loss)
Efficiency Direct	91.4	-	Pout/Pin

4.6.3.3.3. Loss components: [T rated = 574 N.m]

Table 4.19. *Manufactured Motor Loss Segregation Comparison FE, Measurement, 70 Hz, 574 Nm*

	2^{nd} Prototype		Description/ Definition
	Test Inverter	FE 2D Sine	
Airgap [mm]	1.2	1.2	Radial Gap
Time step	-	50	
Non-linear residual	-	1e-08	
s	0.0152	0.152	Slip
Pcu, s (kW)	2.923	2.761	Stator copper losses
Pfe (kW)	3.561	2.20	Iron losses [Original loss coefficients]
Pfe (kW) +Core Effect	-	3.35	
P stray (kw)	0.681	0.656	P stray=0.005* P in
Pcu, r (kW)	1.967	2.233	Rotor copper losses= “Solid loss” +P (end rings)
Pmech (kW)	0.3	0.3	Mechanical Losses(f&w)
Solid Loss (FEM)[kW]*	-	1.75	FEA Loss “Solid Loss”
$P_{er,\ rotor}$ [kW]	-	0.484	Rotor end rind ohmic loss (analytical)
P out [kW]	124.61	124.65	
Total Power Loss (Indirect)	9.432	8.25	Ptot=Pcu, s+Pcu, r+Pfe+Pmech+Pstray
Total Power Loss (Direct)	11.673	-	P in – Pout

In calculating the core loss in 2D FE environment, ANSYS Maxwell provides an option to calculate the core loss not as a post processing calculation but rather take into account the changes to the B field due core loss phenomena. And here in Table 4.19 by considering the core effect, core loss value has increased from 2.2 kW to 3.35 kW.

4.6.4. Variable Speed Performance Comparison

The motor is tested at 5 different frequencies including the 50 Hz , and 70 Hz frequencies discussed earlier.

4.6.4.1. Performance Characteristics at 125 kW – 574 Nm rating

Table 4.20. *Manufactured Motor Performance Characteristics at Rated Values of 125 kW Constant Power Region, and 574 Nm at Constant Torque Region*

f Hz	32	50	70	100	125
Current total rms [A]	182.7	178.7	179.6	173	179.7
Input Power - [kW]	64910	98650	136280	138000	140650
Fundamental Voltage L-L, [V]	228.5	360.6	504.2	501	500.15
Torque [Nm]	572.5	573.9	575.4	404	328.5
Power factor	0.8911	0.871	0.867	0.9173	0.901
Speed [rpm]	926	1468	2068	2947	3623
PT100 [1]	112	106	97	139	112
PT100[4]	76	71	60	114	67
St. Wdg. Temp	103.9	104.9	105.6	130	117
Output Power [kW]	55518	88233	124606	124667	124640
Indirect Total Loss [W]	8124	8267	9433	9671	12597
Direct Total Loss [W]	9392	10417	11674	13333	16010
eff. Indirect	87.2%	91.4%	93.0%	92.8%	90.8%
eff. Direct	85.5%	89.4%	91.4%	90.3%	88.6%

The insulation class of the motor is rated at 180 °C and considering the temperature values obtained from the tests the motor temperature values stay well below the limit. So the motor can be operated at higher power ratings as well. Although the motor is warm while taking the temperature/ resistance measurement, the motor at 50 Hz, and 70 Hz reaches thermal steady state, at those temperature values represent a more accurate readings, whereas in other frequencies readings are taken as the motor is warm. However since the thermal constant is large enough, we assume that the motor at 3 other frequencies is close to reaching steady state, which is a fair assumption considering the measurement have taken place consecutively.

4.7. Target Performance Verification

In this section the performance of the motor is summarized with respect to the rated operating point at 5 different frequencies. Three operating frequencies are selected at constant torque region and two frequencies are selected and the constant power region. The curves are included in Figure 4.7, Figure 4.8, Figure 4.9, Figure 4.10, and Figure 4.11.

The main goal of this chapter is to validate the motor by comparing its characteristics with the target performance to see if it can satisfy the requirements set at the very beginning of this study.

It is expected that our manufactured motor can provide the required performance, however in order to further investigate the motor and its behavior it is better to look at the loss component individually.

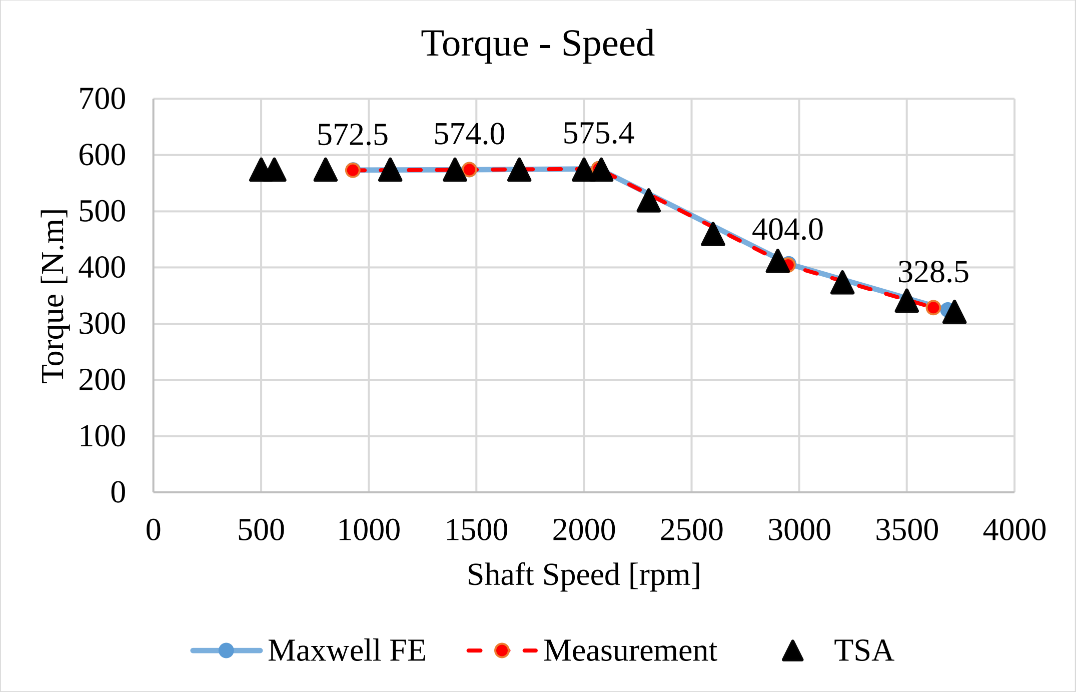

Figure 4.7. Torque – Speed Characteristics .. FE 2D vs. Measurements

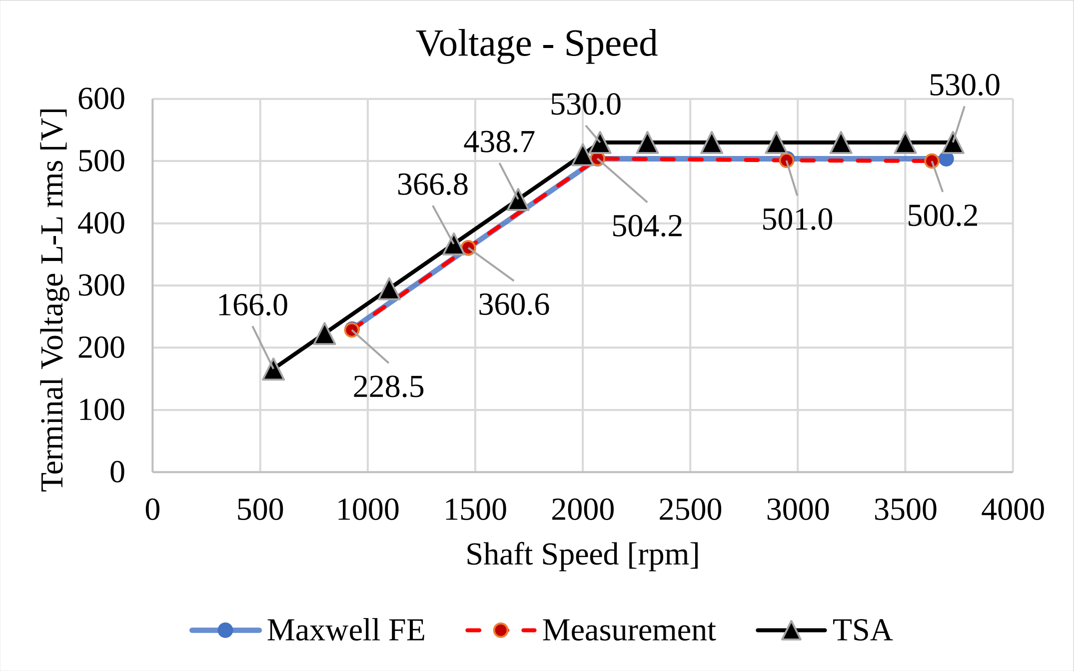

Figure 4.8. Voltage– Speed Characteristics. FE 2D vs. Measurements

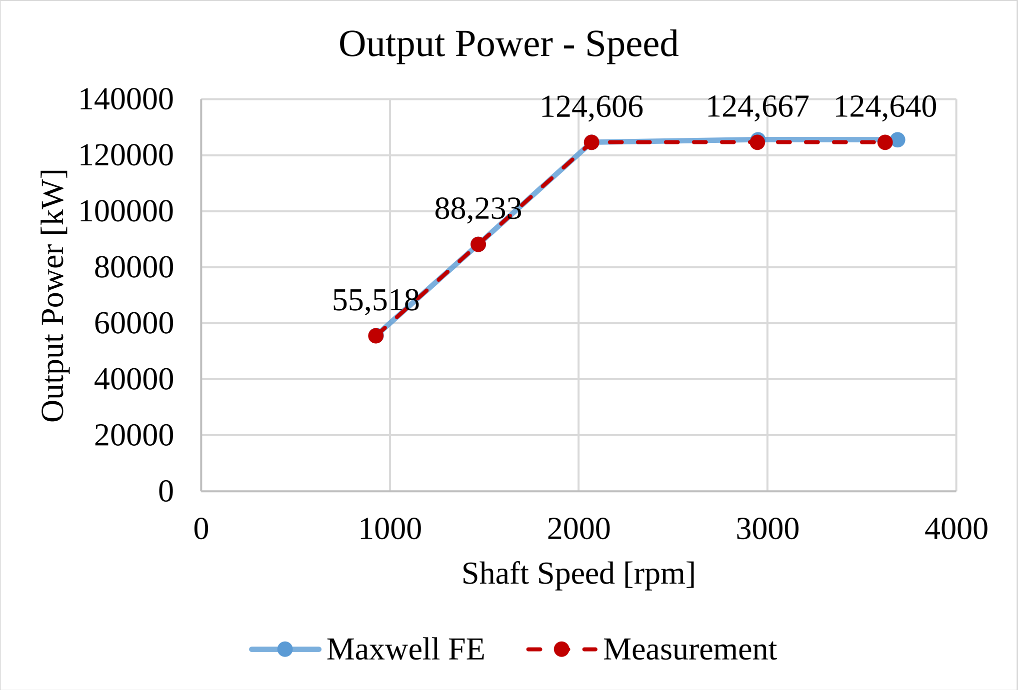

Figure 4.9. Voltage– Speed Characteristics. FE 2D vs. Measurements

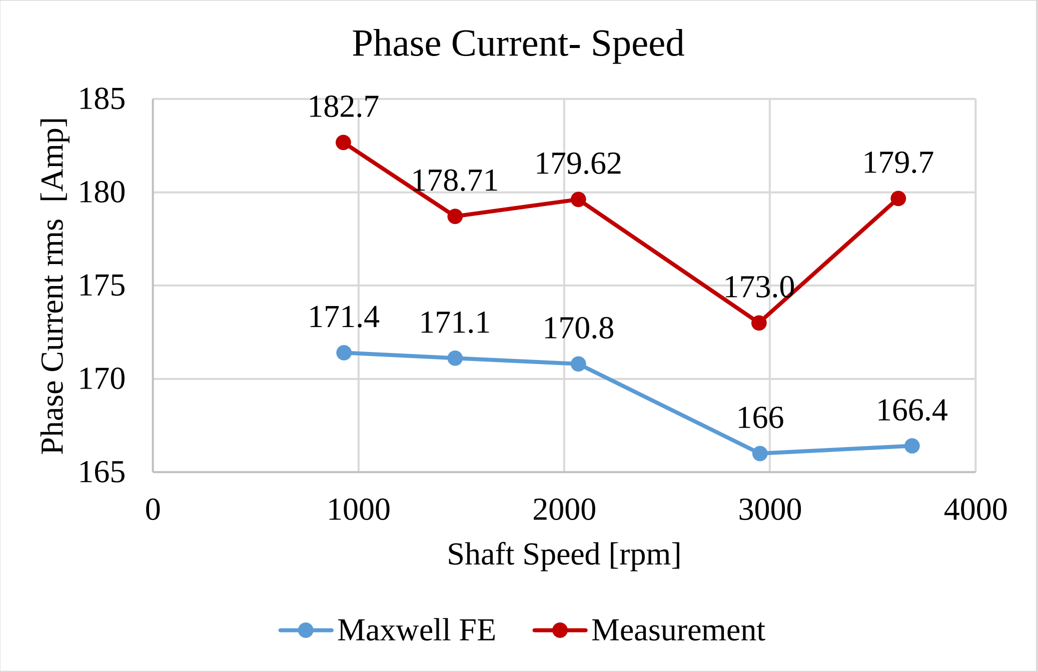

Figure 4.10. Current– Speed Characteristics. FE 2D vs. Measurements

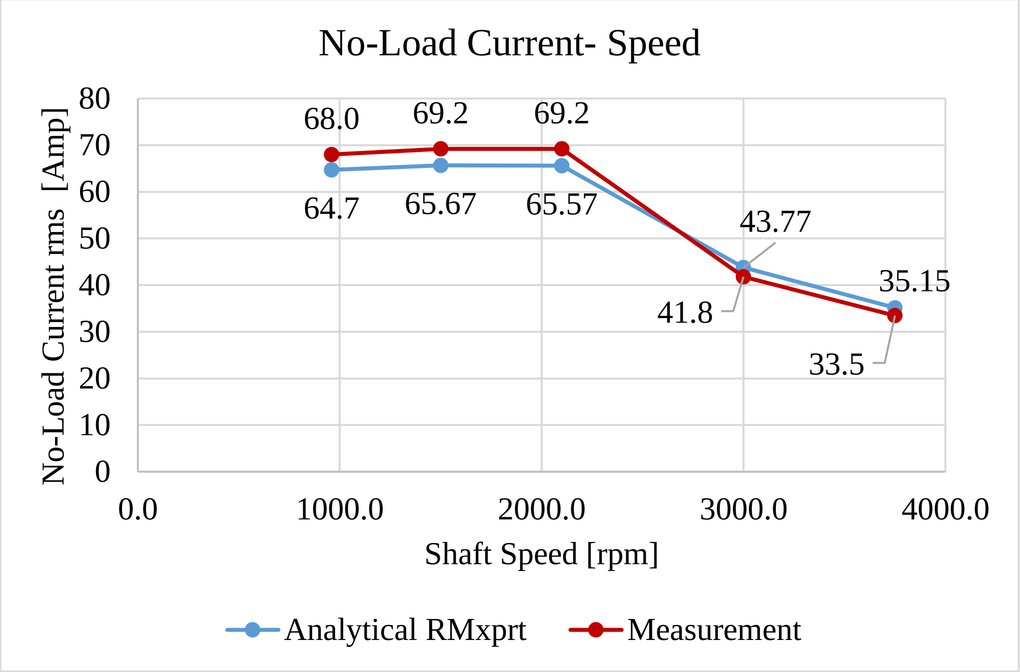

Figure 4.11. No-Load Current– Speed Characteristics. RMxprt vs. Measurements

4.8. Variable Speed Loss Analysis

In this section each loss component will be individually represented, and the measurement data and FE analysis results will be compared. The motor rated performance used for these analyses is included in

Table 4.21. *Motor's S1 Rated Parameters at 70Hz*

	Value
Connection	504 V
Frequency	70 Hz
Shaft Speed	2068 rpm
Pole Number	4
Rated Current	181.1
Power Factor	0.87
Output Power	125 kW
Cooling System	Outer Fan cooled

The motor is operating with constant torque of 574 Nm , from 32 Hz up to 70 Hz and then moves to a constant power region and operates with constant output power of 125 kW from 70 Hz up to 125 Hz.

4.8.1. Stator Copper Loss

Stator copper loss calculation is trivial with respect to the other loss components, however in determining the loss value estimating the temperature is of importance.

Table 4.22. *Stator Winding Temperature, at Rated 574 Nm Torque , w.r.t Frequency*

	f Hz	32	50	70	100	125
Measurement	St. Wdg. Temp [°C]	103.9	104.9	105.6	130	117
FE	St. Wdg. Temp [°C]	104	100	100	130	117

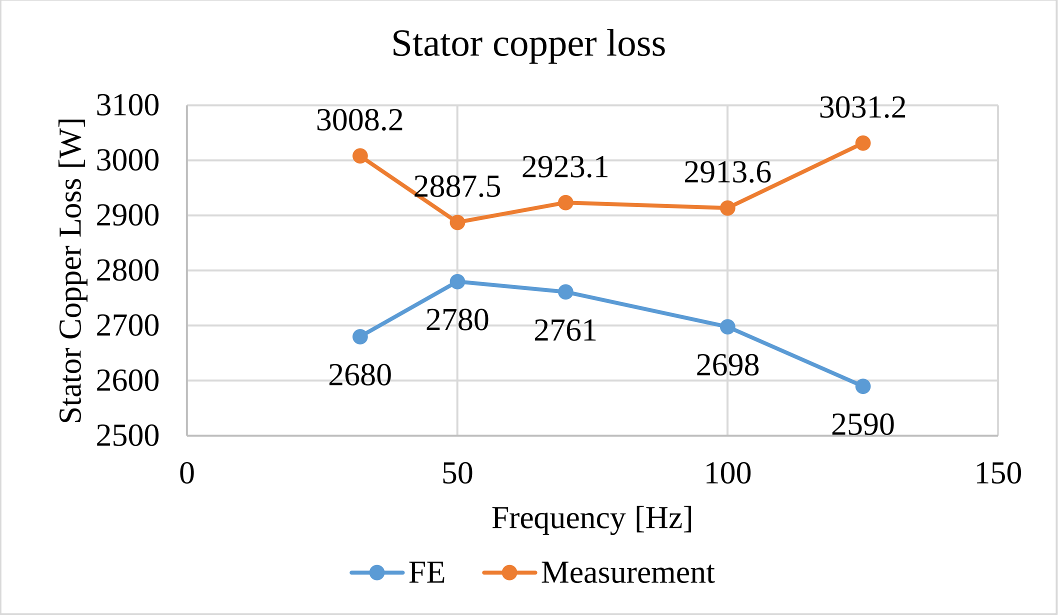

Figure 4.12. Stator Copper Loss ,FE Measurement Comparison Manufactured Motor 125 kW, 574 Nm rated

4.8.2. Rotor Copper Loss

In order to determine the rotor copper loss from measured data, $P_{air\ gap}$ needs to be calculated. Which is determined by subtracting the stator copper loss, core loss , and stray loss from the input power. Rotor copper loss w.r.t IEC standards is (slip × $P_{air\ gap}$).

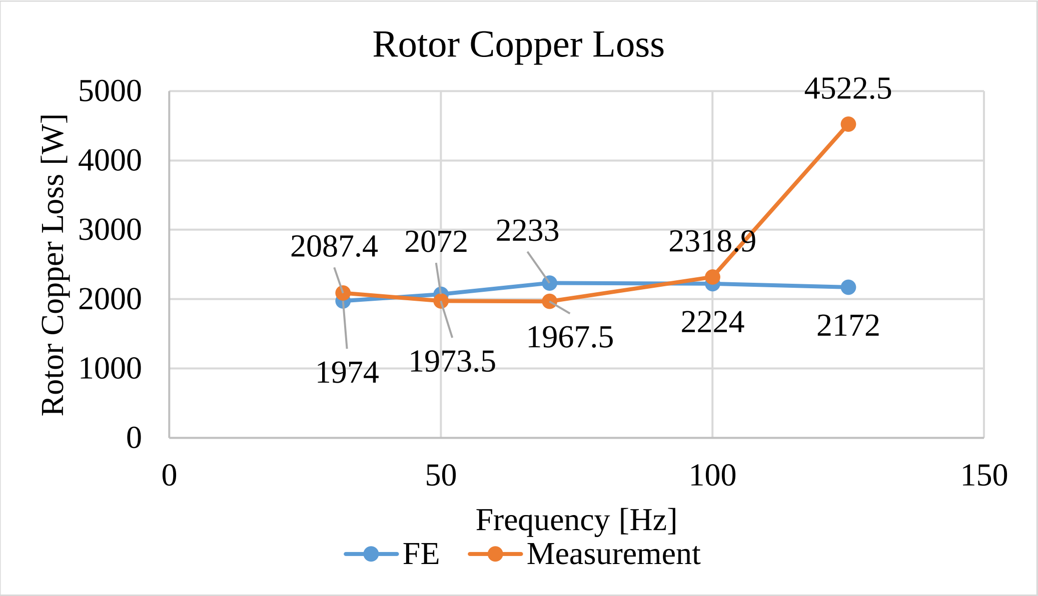

Figure 4.13. Rotor Copper Loss ,FE Measurement Comparison Manufactured Motor 125 kW, 574 Nm rated

4.8.3. Core Loss

As it has been mentioned in Chapter 2 and Chapter 4 (50 Hz, and 70 Hz mode of operation), in both IEEE and IEC standards in using the indirect method to calculate the efficiency. Both standards offer the same solution on calculating the mechanical loss and core loss, which is done by performing the no-load test. In using the Finite Element method although the calculation might seem trivial, but it is important to select the right material with desired B-H curve and core loss coefficient. Also, in determining core loss through Maxwell 2D it is important to use the proper meshing and to use the proper time step for the operation.

Table 4.23. *Time steps at steady state*

Supply Frequency Hz	*Time Step µSec*
32	50
50	50
70	50
100	25
125	25

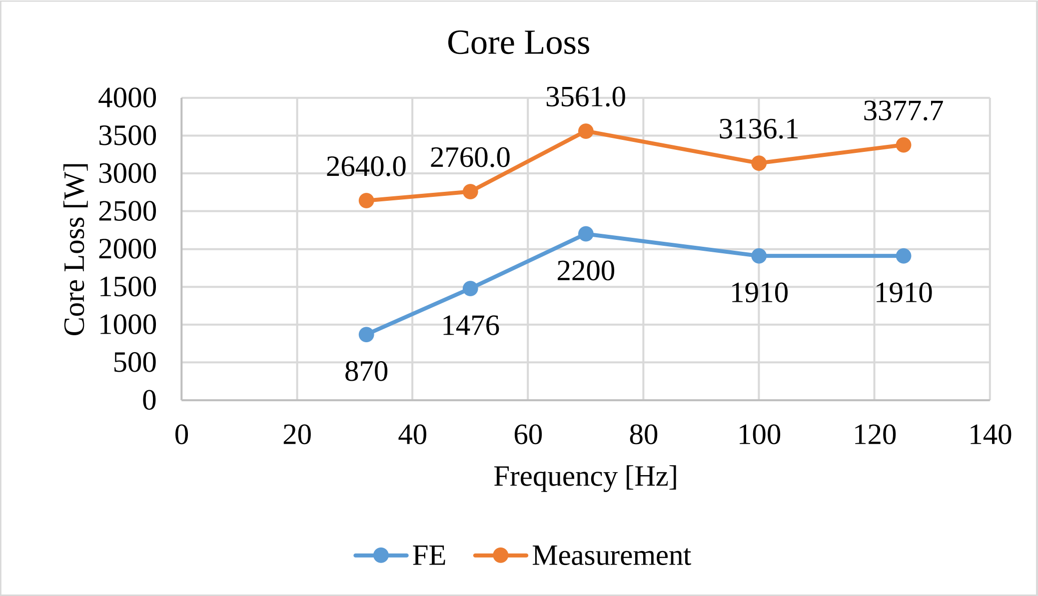

Figure 4.14. Core Loss ,FE Measurement Comparison Manufactured Motor 125 kW, 574 Nm rated

It should be noted that in these core loss calculations core effect option in ANSYS Maxwell is not selected and the calculation is in post processing mode. However for two frequencies of 50 Hz and 70 Hz the simulations have been repeated w.r.t the core effect being on which the results are included in4.6.1.3.2 and 4.6.3.3.3 which yield much closer values. However, in using this option you can only utilize one CPU core and thus it significantly increases the solution time.

In Finite Element simulations from which these plots are derived, the excitation is sinusoidal, whereas the measurement data uses an inverter to drive the motor. The gap between the data is assumed to be related to this fact.

4.8.4. Friction and Windage Losses (Mechanical Loss)

As explained in Section 4.6.3.1, mechanical loss is determined at a specific case that we know it represent the correct value at that condition (50 Hz , sinusoidal supply), and at the rest of the frequencies friction & windage loss is calculated analytically.

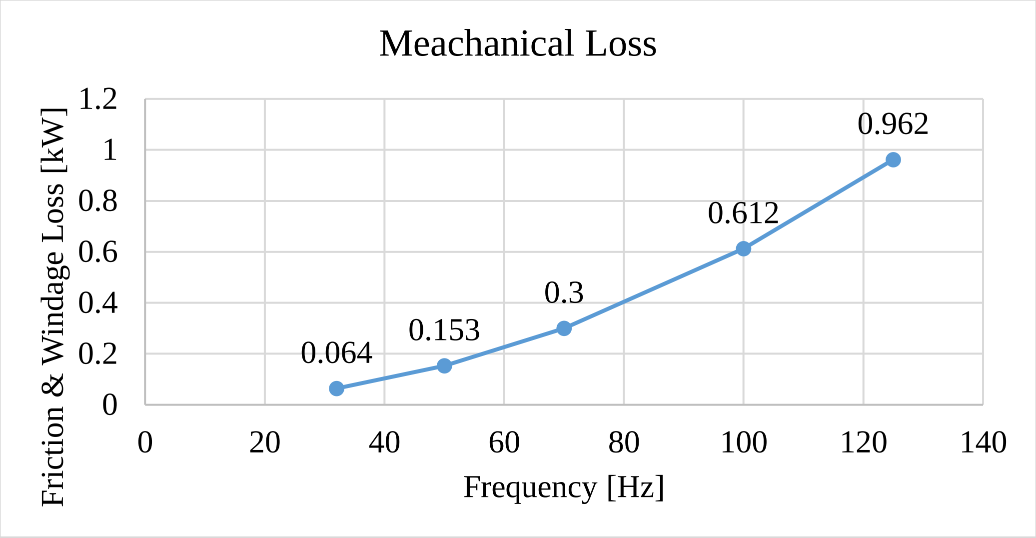

Figure 4.15. Mechanical Loss at No-Load

4.8.5. Efficiency -Direct , Indirect

In calculating the efficiency using direct method $\eta = {}^{P_{out}}/_{P_{in}}$ and in Indirect method , by using loss segregation $\eta = {}^{P_{out}}/_{P_{out} + total\ loss}$.

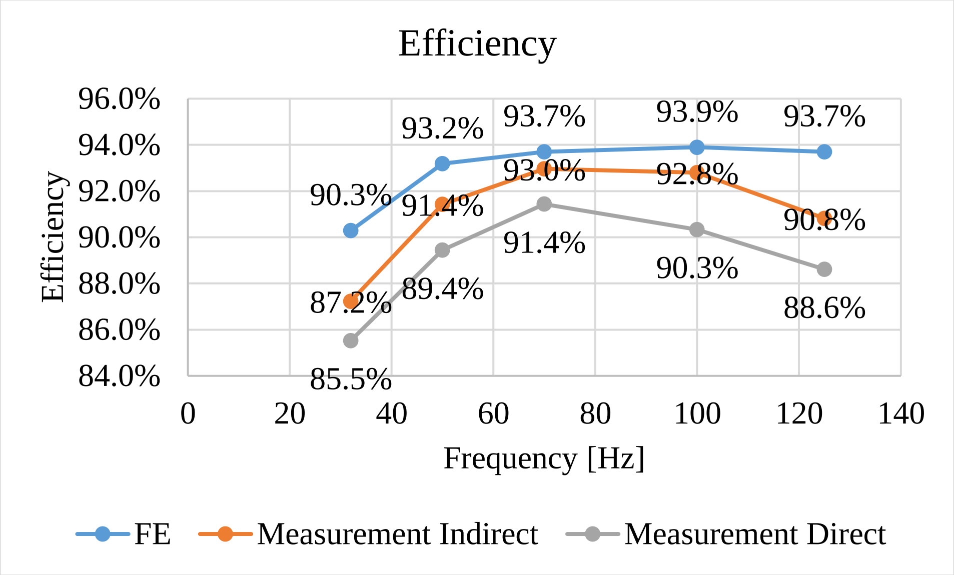

Figure 4.16. Efficiency Comparison, Manufactured Motor 125 kW, 574 Nm rated

4.8.6. Total Loss – Direct and Indirect (Stray Load loss)

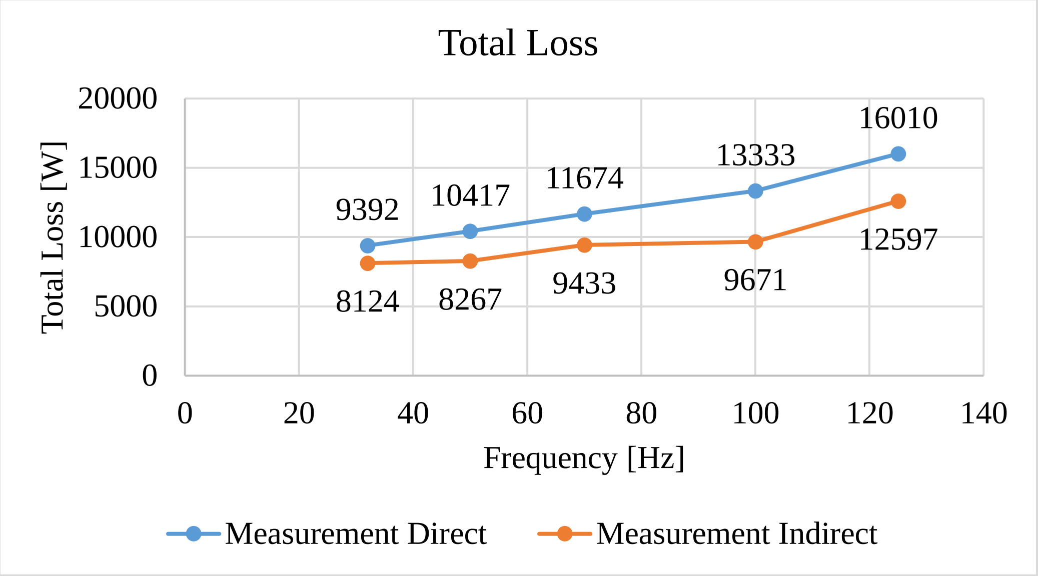

Figure 4.17. Total Loss Comparison, Manufactured Motor 125 kW, 574 Nm rated

It can be seen from the figure above that there is a gap between two methods, this is expected in measurements and considering two measurements are reliable this difference is referred to as stray load loss. The Standards followed in this thesis for this purpose is the IEC standard, in which stray load loss is determined as the 0.5 % of the input power. However, if you use the IEEE standard the stray load losses will be different.

Table 4.24. *IEEE Std 112 1996 on stray load loss estimation*

Machine rating	*Stray-Load loss percent of rated output*
1-90 kW	1.8 %
91-375 kW	1.5 %
376-1850 kW	1.2 %
1851 kW and greater	0.9 %

As a result:

Table 4.25. *Stray Load Loss Estimation based on IEC, IEEE and Measurement*

Frequency Hz	Direct Method – Indirect Method [Watt]	Stray Load Loss (IEC) [Watt]	Stray Load Loss (IEEE) [kW]
32	1268	325	1
50	2149	493	1.58
70	2241	681	1.875
100	3662	690	1.87
125	3412	703	1.87

These are all approximations and there should be a method to calculate the stray load loss more accurately rather that estimation. One method that can be used to calculate the high frequency loss component which comprise the stray load loss can be found in [6], [7]. A further study is planned to closely analyze the core loss distribution in the rotor and stator to better understand the various components of the core loss and how they are affected by higher order harmonics.

CHAPTER 5

CONCLUSION

In this study a traction induction motor, is developed, and manufactured. To achieve this Finite Element calculations and simulation models are verified, a process is implemented to design and improve a simulation model and finally the developed model is verified through Finite Element analysis to make sure it is capable of meeting the requirement.

As first step, a reference test motor has been selected, which its test results obtained through measurements. Upon close inspections of the motor. its 3D solid model has been derived and modeled in a computer environment and as such its electromagnetic model has been constructed in ANSYS Maxwell. After modelling the reference test motor in ANSYS Maxwell. The model is studied to determine loss components , their distribution and efficiency evaluation of the motor. Next by analyzing the reference test motor we created some guidelines to help the designing process.

Based on the design criteria that formed previously, an initial design has been selected. The initial design’s parameters are determined based on the constraint of the application (for example the limited space), and by utilizing design criteria that was created from the reference motor (the initial design is selected in manner to have the same output coefficient as the reference motor). In order to progress the design we used thermal and fluid flow analysis to understand how the motor is behaving thermally and whether we need to change the design to address the excess loss or not. At each electromagnetic design iteration we tried to reduce the stator and rotor copper loss while maintaining a balance between electric loading and magnetic loading. Also we selected an optimum cooling system by including 0.5 cm stator ducts at the rim of the stator.

Finally as the electromagnetic design has been finalized, and the materials has been selected, the model has gone under some changes regarding the mechanical and manufacturing difficulties. A first prototype has been manufactured and based on the tests that has been performed on the motor, a new flat type winding arrangement has been selected which was used in the final manufactured prototype.

Each design and computer simulation need to be verified to add to its credibility and at the final stage the FE model was compared to the actual motor. Several tests including no-load test, load tests have been performed at various frequency points of 32, 50, 70, 100, and 125 Hz. And Based on the standards available, the motor's performance have been determined and its loss components have been individually determined. And compared with the FE model. There exist a good agreement between the FE model and the test results regarding the loss components and performance characteristics. And as it was presented in Chapter 4, the manufactured motor is fully capable of delivering the target performance. However the core loss calculations need to be more accurately determined when it comes to the FE analysis as in the comparisons the only parts that does not agree is the core loss calculations specifically when it comes to higher frequencies.

REFERENCES

[1] J. F. Gieras and N. Bianchi, “Electric Motors for Light Traction,” *EPE J.*, vol. 14, no. 1, pp. 12–23, Feb. 2004.

[2] A. Boglietti *et al.*, “Electrical Machine Topologies: Hottest Topics in the Electrical Machine Research Community,” *IEEE Ind. Electron. Mag.*, vol. 8, no. 2, pp. 18–30, Jun. 2014.

[3] E. B. Agamloh and A. Cavagnino, “High efficiency design of induction machines for industrial applications,” *Proc. - 2013 IEEE Work. Electr. Mach. Des. Control Diagnosis, WEMDCD 2013*, pp. 33–46, 2013.

[4] H. B. Ertan, K. Leblebicioğlu, B. Avenoğlu, and M. Pirgaip, “High-frequency loss calculation in a smooth rotor induction motor using FEM,” *IEEE Trans. Energy Convers.*, vol. 22, no. 3, pp. 566–575, 2007.

[5] M. Kondo, R. Ebizuka, and A. Yasunaga, “Rotor design for high efficiency induction motors for railway vehicle traction,” *Proc. - 12th Int. Conf. Electr. Mach. Syst. ICEMS 2009*, 2009.

[6] S. Nandi, “Modeling of induction machines including stator and rotor slot effects,” *IEEE Trans. Ind. Appl.*, vol. 40, no. 4, pp. 1058–1065, 2004.

[7] T. A. Lipo, “Introduction to AC Machine design,” pp. 536–540, 2011.

[8] S. Nandi, S. Ahmed, and H. A. Toliyat, “Detection of rotor slot and other eccentricity related harmonics in a three phase induction motor with different rotor cages,” *IEEE Trans. Energy Convers.*, 2001.

[9] I. E. T. Energy and E. Series, *Fault Diagnosis of Induction Motors*. 2017.

[10] M. Kondo, M. Miyabe, R. Ebizuka, and K. Hanaoka, “Design and efficiency evaluation of a high-efficiency induction motor for railway traction,” *Electr. Eng. Japan (English Transl. Denki Gakkai Ronbunshi)*, vol. 194, no. 2, pp. 15–23, 2016.

[11] P. Lindh, L. Aarniovuori, H. Karkkainen, M. Niemela, and J. Pyrhonen, “IM Loss Evaluation Using FEA and Measurements,” in *2018 XIII International Conference on Electrical Machines (ICEM)*, 2018, pp. 1220–1226.

[12] S. Williamson and M. C. Begg, “Calculation of the resistance of induction motor end rings,” *IEE Proc. B Electr. Power Appl.*, vol. 133, no. 2, p. 54, 1986.

[13] L. Aarniovuori, P. Rasilo, M. Niemela, and J. J. Pyrhonen, “Analysis of 37-kW Converter-Fed Induction Motor Losses,” *IEEE Trans. Ind. Electron.*, vol. 63, no. 9, pp. 5357–5365, 2016.

[14] J. Pippuri and A. Arkkio, “Challenges in the segregation of losses in cage induction machines,” in *2008 18th International Conference on Electrical Machines*, 2008, pp. 1–5.

[15] S. Nategl, D. Lindberg, O. Aglen, R. Brammer, and A. Boglietti, “Review and Trends in Traction Motor Design: Electromagnetic and Cooling System Layouts,” *Proc. - 2018 23rd Int. Conf. Electr. Mach. ICEM 2018*, pp. 2600–2606, 2018.

[16] S. O. Kwon, J. J. Lee, B. H. Lee, J. H. Kim, K. H. Ha, and J. P. Hong, “Loss distribution of three-phase induction motor and BLDC motor according to core materials and operating,” *IEEE Trans. Magn.*, vol. 45, no. 10, pp. 4740–4743, 2009.

[17] K. Komeza and M. Dems, “Finite-Element and Analytical Calculations of No-Load Core Losses in Energy-Saving Induction Motors,” *IEEE Trans. Ind. Electron.*, vol. 59, no. 7, pp. 2934–2946, Jul. 2012.

[18] G. Bertotti, “General properties of power losses in soft ferromagnetic materials,” *IEEE Trans. Magn.*, vol. 24, no. 1, pp. 621–630, Jan. 1988.

[19] S. Mizuno, S. Noda, M. Matsushita, T. Koyama, and S. Shiraishi, “Development of a totally enclosed fan-cooled traction motor,” *IEEE Trans. Ind. Appl.*, vol. 49, no. 4, pp. 1508–1514, 2013.

[20] D. T. Peters, E. F. Brush, and J. L. Kirtley, “Die-cast copper rotors as strategy for improving induction motor efficiency,” in *2007 Electrical Insulation Conference and Electrical Manufacturing Expo*, 2007, pp. 322–327.

[21] E. Kurvinen, C. Di, I. Petrov, R. P. Jastrzebski, D. Kepsu, and J. Pyrhonen, “Comparison of the Performance of Different Asynchronous Solid-Rotor Constructions in a Megawatt-Range High-Speed Induction Motor,” pp. 820–825, 2019.

[22] R. N. Lal and Ganesh, “Development of reliable designs of squirrel cage rotors for traction motors used in locomotives working in arduous operating conditions,” *IET Electr. Power Appl.*, vol. 4, no. 7, p. 487, 2010.

[23] V. Callcut, “High Copper Alloys - High Strength Coppers for Demanding Electrical Applications,” *Copper Development Association*, no. September. 2006.

[24] J. B. Bartolo, H. Zhang, D. Gerada, L. De Lillo, and C. Gerada, “High speed electrical generators, application, materials and design,” *Proc. - 2013 IEEE Work. Electr. Mach. Des. Control Diagnosis, WEMDCD 2013*, pp. 47–59, 2013.

APPENDICES

A. Electrical Steel Characteristics

The COGENT steel with model number of SURA M530-50A which is a non-grain oriented electrical steel is used as the core material in the stator as well as the rotor. The B-H curve is given in Figure A.1.

Table A.1. *SURA M530-50A Characteristics*

Material Name	Relative Permeability	Bulk conductivity	Core loss model			Mass density
SURA M530-50A	Nonlinear B-H	3125000siemens/m	Electrical steel w/m^3			7750kg/m^3
			K_h	K_c	K_e	
			513.8	0.47	4.13	

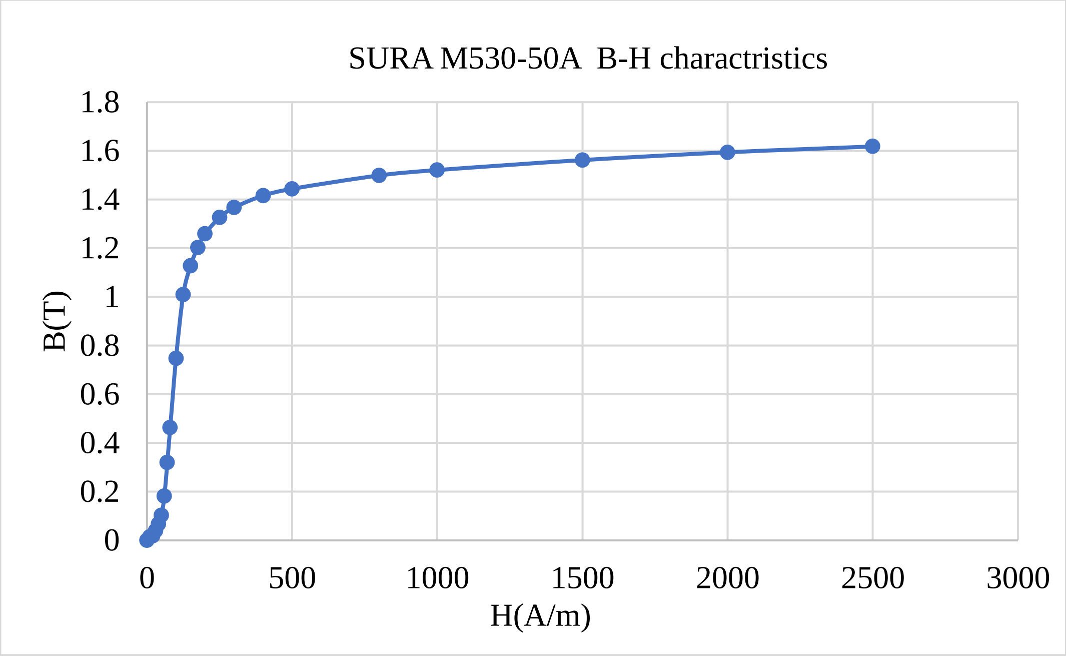

Figure A.1. SURA M530-50A B-H curve

And the data table is included in Table A.2

Table A.2. *SURA M530-50A B-H data*

B [Tesla]	H [A/m]	B [Tesla]	H [A/m]	B [Tesla]	H [A/m]
0.1	56.1	0.7	123	1.3	243
0.2	74.1	0.8	133	1.4	333
0.3	85.8	0.9	145	1.5	573
0.4	95.6	1.0	158	1.6	1345
0.5	105	1.1	174	1.7	3367
0.6	114	1.2	200	1.8	6964

B. Rotor Conductor’s Material

The conductor used in the rotor bars as well as the rotor cage short circuit end rings are a copper alloy specifically chromium-zirconium-copper. The alloy used in this study has the characteristics mentioned below.

Table B.1. *Rotor Conductors Electrical and Mechanical Properties*

Rotor bars - physical and mechanical properties			
Alloys	Electrical conductivity γ MS / m	Electrical Resistivity ρ $\mu\Omega \cdot$ cm	Density ρ kg / dm^3
CuCrZr	47	2.13	8.9